



Microstructure-property relationships in Cr(C)N coatings

Author:

Sun, Wei-Lien

Publication Date:

2014

DOI:

<https://doi.org/10.26190/unsworks/2571>

License:

<https://creativecommons.org/licenses/by-nc-nd/3.0/au/>

Link to license to see what you are allowed to do with this resource.

Downloaded from <http://hdl.handle.net/1959.4/53552> in <https://unsworks.unsw.edu.au> on 2024-05-03

Microstructure-property relationships in Cr(C)N coatings

Wei-Lien SUN

A thesis in fulfilment of the requirements for the degree of
Master of Philosophy

THE UNIVERSITY OF
NEW SOUTH WALES



School of Materials Science and Engineering
Faculty of Science

March 2014

PLEASE TYPE

THE UNIVERSITY OF NEW SOUTH WALES
Thesis/Dissertation Sheet

Surname or Family name: Sun

First name: Wei-Lien

Other name/s:

Abbreviation for degree as given in the University calendar: MPhil

School: Material Science and Engineering

Faculty: Faculty of Science

Title: Microstructure-properties relationships in Cr(C)N coatings

Abstract 350 words maximum: (PLEASE TYPE)

In this study, the effect of carbon on microstructure, mechanical properties, tribological properties and the deformation and fracture behavior in CrN and CrCN coatings with various graphite target currents in the deposition process were investigated.

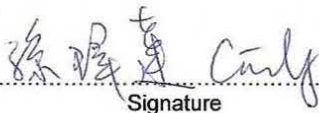
The elemental composition of Cr(C)N was characterized by X-ray photoelectron spectroscopy (XPS). With the increase in graphite target current, the carbon content in the Cr(C)N increased. The microstructure of Cr(C)N was investigated using atomic force microscopy (AFM), focused ion beam (FIB) microscopy, x-ray diffraction (XRD) and transmission electron microscopy (TEM). AFM and cross-sectional FIB images and TEM images show the grain size was decreasing with carbon content. XRD and the selected area electron diffraction patterns (SAED) of TEM show the phase was changing from Cr₂N-dominant to CrN-dominant with increasing carbon content in the Cr(C)N coatings. Energy dispersive spectroscopy (EDS) of TEM analyzes the distribution of elements across the sample cross-section.

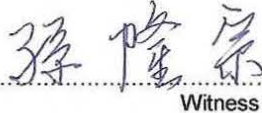
Hardness and Young's modulus were obtained using a Hysitron Triboindenter. The coefficient of friction was obtained using pin-on-disk tribometer. Deformation and fracture behaviour of the Cr(C)N coatings was determined using UMIS nanoindentation and pin-on-disk tribometer, followed by cross-sectional FIB and TEM analysis. Crack can only be observed in the Cr(C)N coatings with low carbon content even at a load of 500mN for UMIS nanoindentation and a load of 5N for pin-on-disk tribometer. Generally, hardness, modulus and coefficient of friction are generally decreased with carbon content. However, some results show a slightly difference which might attribute to various factors such as bonding types, phases and grain size etc.

Declaration relating to disposition of project thesis/dissertation

I hereby grant to the University of New South Wales or its agents the right to archive and to make available my thesis or dissertation in whole or in part in the University libraries in all forms of media, now or here after known, subject to the provisions of the Copyright Act 1968. I retain all property rights, such as patent rights. I also retain the right to use in future works (such as articles or books) all or part of this thesis or dissertation.

I also authorise University Microfilms to use the 350 word abstract of my thesis in Dissertation Abstracts International (this is applicable to doctoral theses only).


Signature


Witness

24. 6. 2014
Date

The University recognises that there may be exceptional circumstances requiring restrictions on copying or conditions on use. Requests for restriction for a period of up to 2 years must be made in writing. Requests for a longer period of restriction may be considered in exceptional circumstances and require the approval of the Dean of Graduate Research.

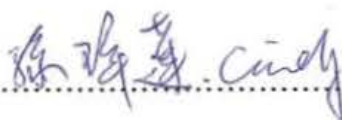
FOR OFFICE USE ONLY

Date of completion of requirements for Award:

ORIGINALITY STATEMENT

'I hereby declare that this submission is my own work and to the best of my knowledge it contains no materials previously published or written by another person, or substantial proportions of material which have been accepted for the award of any other degree or diploma at UNSW or any other educational institution, except where due acknowledgement is made in the thesis. Any contribution made to the research by others, with whom I have worked at UNSW or elsewhere, is explicitly acknowledged in the thesis. I also declare that the intellectual content of this thesis is the product of my own work, except to the extent that assistance from others in the project's design and conception or in style, presentation and linguistic expression is acknowledged.'

Signed

.....

Date

24.6.2014.....

Acknowledgements

First of all, I wish to express my deepest gratitude to my supervisor, Professor Paul Munroe for his patience in guiding me throughout the entire project. His incessant support has motivated me to ensure that this entire project is successful. I am also indebted to him for his critical review of this thesis. I also wish to acknowledge Associate Professor Sammy Lap Ip Chan, my co-supervisor, for his warm encouragement and advice throughout my studies.

I wish to extend my appreciation to several academic and technical staff in UNSW who provided help and assistance in this study. I would like to particular express my appreciation to Ms. Lana Strizhevsky, Ms. Jane Gao, Mr Danny Kim, Mr. George Yang and Mr. Joseph Arsecularatne from the School of Material Science and Engineering; Ms. Leah Koloadin from the Electron Microscopy Unit; Dr. Yu Wang, Dr. Bill Gong from the Solid State and Elemental Analysis Unit.

Especially, I would like to express my sincere appreciation to Mr. Bill Joe for his willing help with the UMIS nanoindentation, Hysitron triboindentation and Pin-on-disk Tribometer. I would also like to thank him for his invaluable encouragement and suggestion.

I wish to acknowledge Mr. Sean Lim for his patience during my training in transmission electron microscopy, Nova FIB and atomic force microscope. I also want to thank him for his kind help and skilled assistance. I would also like to thank Dr. Charlie Kong for his patience on training me in dual beam FIB microscopy.

I would also like to thank the Department of Mechanical and Biomedical Engineering of the City University of Hong Kong for providing the Cr(C)N coating specimens for this study.

Last but not the least, I wish to express my deepest gratitude to my family and friends for supporting me throughout my study time in UNSW and stimulating me to increase my efforts.

Abstract

In this study, the effect of carbon additions on the microstructure, mechanical properties, tribological properties and the deformation and fracture behaviour of CrN coatings were investigated. Four CrN-based coatings were deposited on M2 steel substrates using a closed field unbalanced magnetron sputtering ion plating deposition system. The carbon content in the coatings was varied by changing the current on the graphite target.

The elemental composition of Cr(C)N was characterized by X-ray photoelectron spectroscopy (XPS). With increases in the graphite target current, the carbon content in the Cr(C)N coatings increased. The microstructure of the Cr(C)N coatings was investigated using atomic force microscopy (AFM), focused ion beam (FIB) microscopy, x-ray diffraction (XRD) and transmission electron microscopy (TEM). AFM, cross-sectional FIB images and TEM images show that the grain size decreased with increasing carbon content. XRD and the selected area electron diffraction patterns (SAED) acquired via TEM showed that the dominant phase in the coatings transformed from Cr₂N to CrN with increasing carbon content in the coatings.

Hardness and Young's modulus measurement were obtained using a Hysitron nanoindenter. The coefficient of friction was obtained using pin-on-disk tribometer. The deformation and fracture behaviour of the Cr(C)N coatings was determined using UMIS nanoindentation, followed by cross-sectional FIB and TEM analysis. Cracking in the coating was only be observed in the Cr(C)N coatings with low carbon contents even at high loads Generally, hardness, modulus and coefficient of friction decreased with carbon content. However, the relationship between these properties and carbon content was complex and appeared to depend on several inter-related parameters.

Table of Contents

Acknowledgements	i
Abstract	ii
Table of Contents	iii
List of Figures	v
List of Tables	ix
Chapter 1 Introduction	1
Chapter 2 Literature review	3
2.1 Overview	3
2.2 CrN thin films	3
2.2.1 Cr-N Equilibrium phase diagram	3
2.2.2 Film deposition methods	5
2.2.3 Structure of CrN-based phases	16
2.2.4 Properties of CrN	18
2.3 CrCN thin films	19
2.4. Characterization techniques	23
2.4.1 Scanning Electron Microstructure (SEM)	23
2.4.2 Focused Ion Beam Microscopy (FIB)	24
2.4.3 Dual-Beam Focused Ion Beam	25
2.4.4 Transmission Electron Microscopy (TEM)	26
2.4.5 X-Ray Diffraction (XRD)	28
2.4.6 X-ray Photoelectron Spectroscopy (XPS)	30
2.4.7 Atomic Force Microscopy (AFM)	31
2.4.8 Tribometry	32
2.5. Deformation and Fracture behaviour	33
2.5.1 Nanoindentation	33
2.5.2 Thin film cracking	39
2.6. Summary	41
Chapter 3 Experimental Procedure	42
3.1 Introduction	42
3.2 Material Deposition Conditions	42
3.3 Composition and Microstructure Characterization	43

3.3.1 X-ray Photoelectron Spectroscopy (XPS).....	43
3.3.2 X-ray Diffraction (XRD).....	44
3.3.3 Atomic Force Microscopy (AFM)	44
3.3.4 Focused Ion beam (FIB) Microscopy	46
3.3.5 Transmission Electron Microscopy (TEM).....	47
3.3.6 Scanning Electron Microscopy (SEM)	47
3.4 Mechanical and tribological properties Characterizations.....	48
3.4.1 Hysitron Triboindenter	48
3.4.2 Pin-on-disk wear testing.....	49
3.5 Deformation behaviour characterization.....	49
3.5.1 Ultra Micro-Indentation System (UMIS).....	49
Chapter 4 Result and discussion	50
4.1 Introduction	50
4.2 Composition and microstructural characterization	51
4.2.1 Focused Ion Beam Microscopy.....	51
4.2.2 X-ray Photoelectron Spectroscopy (XPS).....	53
4.2.3 X-ray Diffraction (XRD).....	60
4.2.4 Transmission Electron Microscopy (TEM).....	63
4.2.5 Atomic Force Microscopy (AFM)	73
4.3 Mechanical and tribological properties characterization	75
4.3.1 Mechanical properties	75
4.3.2 Tribological properties	80
4.4 Deformation and fracture behaviour[115].....	82
4.4.1 Ultra Micro-Indentation System (UMIS).....	82
4.4.2 Deformation behaviour characterization.....	89
4.4.3 Wear track characterization.....	93
4.5 Summary	98
Chapter 5 General discussion.....	99
5.1 Introduction	99
5.2 Microstructure and composition versus mechanical properties	99
5.3 Deformation mechanism v.s. Indentation curves	101
Chapter 6 Conclusions and summary.....	102
References	104

List of Figures

<u>Figure</u>	<u>Description</u>	<u>Page</u>
2.1	Equilibrium phase diagram for the Cr-N system [1, 2]	4
2.2	N concentration in CrN _x (0 ≤ x ≤ 1) vs. the ratio of nitrogen partial pressure to the total gas pressure in the sputtering chamber [2]	5
2.3	A schematic diagram of a cathodic arc evaporation system	6
2.4	A schematic diagram of (a) Magnetron sputtering (b) Unbalanced magnetron sputtering [3]	7
2.5	X-Ray diffraction patterns of as-deposited CrN _x films with different pN ₂ ratio to total pressure (%): (a) 0% (b) 0.5% (c) 1.0% (d) 2.0% (e) 5.0% (f) 8.0% (g) 10% (h). 12.0% (i) 15.0% (j) 20.0% (k) 30.0% (l) 40.0% [2]	10
2.6	X-ray diffraction patterns for CrN films deposited at different bias voltages [4]	11
2.7	The effect of substrate temperature on the texture coefficient of CrN [5]	12
2.8	Hardness and reduced modulus of CrN _x as a function of nitrogen partial pressure ratio to the total pressure [2]	14
2.9	The effect of substrate temperature on hardness of CrN at the deposition conditions: pN ₂ =1.6 Pa, V _S =-100 V and I _{arc} =80 A [5]	15
2.10	A schematic diagram of (a) HCP structure (b) NaCl structure (c) (111) plane of FCC structure	17
2.11	Bright field TEM images of (a) Cr/CrN multilayer coating on a titanium substrate (b) the interface between Cr and CrN layers with electron diffraction patterns for Cr, CrN and Cr ₂ N [6]	18
2.12	X-ray diffraction patterns of CrCN coatings with various carbon contents [7]	20
2.13	Two-dimensional AFM plan view images of Cr(C)N coatings (a) I _C =0 A (b) I _C =0.3 A (c) I _C =0.9 A (d) I _C =1.5 A [8]	20
2.14	Bright field TEM images and diffraction pattern of CrCN coatings (a) I _C =0 A (b) I _C =0.3 A (c) I _C =1.5 A [8]	21
2.15	The interaction of an incident electron beam with the specimen [9]	24

2.16	Preparation of a cross-section (a) ion beam used for milling (b) tilting and imaging [10]	24
2.17	A schematic diagram for TEM specimen preparation by the H-bar technique [11]	25
2.18	A schematic diagram of the dual-beam FIB [12]	26
2.19	A schematic ray diagram for the TEM showing (a) image formation (b) diffraction pattern formation. The back focal plane and the image plane of each lens are shown [13]	28
2.20	A schematic diagram showing Bragg's Law	29
2.21	XPS spectrum of a CrCN coating [8]	30
2.22	Interaction forces between a tip and sample surface [14]	31
2.23	Comparison of (a) contact mode (b) non-contact mode (c) tapping mode [15]	32
2.24	Load-indentation depth curve for a Cr coating measured with a (a) Berkovich indenter (b) spherical indenter [16]	35
2.25	Figure 2.25: A schematic diagram of a load-displacement curve of (a) pop-in (b) pop-out [17]	35
2.26	A schematic diagram of a load-displacement curve for nano-indentation [18]	36
2.27	A schematic diagram of spherical indentation with piling up and sinking in [19]	38
2.28	Principle of deformation behaviour for spherical indentation [20]	39
2.29	A schematic diagram of the cracking during loading and unloading with a spherical indenter [21].	40
3.1	Definition of the arithmetic average height [22]	45
3.2	Section function analysis using an AFM	45
3.3	Dual beam FIB images taken during TEM specimen preparation	47
4.1	FIB images of cross-sections of the undeformed coatings (a) A (b) B (c) C (d) D	51
4.2	XPS survey etch spectra of the four Cr(C)N coatings with a 120s surface clean	53
4.3	The elemental concentration in the Cr(C)N coatings as determined from a survey etch following a 120s surface clean	54

4.4	XPS depth-profile of Cr(C)N for the coatings (a) A (b) B (c) C (d) D	55
4.5	C1s fine spectra for specimens (a) A (b) B (c) C (d) D	57
4.6	Cr2p fine spectra for specimens (a) A (b) B (c) C (d) D	58
4.7	X-ray diffraction spectra of the four Cr(C)N coatings	60
4.8	Bright-field TEM images of the Cr wetting layer (a)-(d) and Cr(C)N layer (e)-(f) for specimens A, B, C and D respectively	64
4.9	Selected area electron diffraction patterns from the Cr(C)N layers of (a) A (b) B (c) C (d) D	65
4.10	EDS elemental maps for Specimen A (a) Cr (b) N (c) Fe (d) C (e) bright field STEM image	69
4.11	EDS elemental maps for Specimen B (a) Cr (b) N (c) Fe (d) C (e) bright field STEM image	70
4.12	EDS elemental maps for Specimen C (a) Cr (b) N (c) Fe (d) C (e) bright field STEM image	71
4.13	EDS elemental maps for Specimen D (a) Cr (b) N (c) Fe (d) C (e) bright field STEM image	72
4.14	AFM images with scanasyst mode in 5 μ m x 5 μ m area for the Cr(C)N coatings (a) A (b) B (c) C (d) D	73
4.15	TEM bright field image of specimen B	74
4.16	Histograms showing the values of H, E, H/E and H ³ /E ² for different C target currents	76
4.17	Depth vs. Load under 8mN using Hysitron indentation	79
4.18	Friction behaviour of Cr(C)N coatings sliding against ruby balls	80
4.19	Coefficient of friction as a function of carbon target current	81
4.20	Deformation behaviour at loads 100-500mN of specimens (a) A (b) B (c) C (d) D	84
4.21	Load-displacement curve to loads of (a) 100mN (b) 200mN (c) 300mN (d) 400mN (e) 500mN	87
4.22	FIB images showing deformation behaviour after spherical nanoindentation with 500mN of (a) A (b) B (c) C (d) D showing plan view; (e) A (f) B (g) C (h) D showing cross-sectional view	90
4.23	A bright field TEM image of (a) centre (b) left (c) right (d) top of indented area using spherical indenter under a 500mN of specimen B	92

4.24	SEM images showing wear tracks after pin-on-disk wear testing for specimens (a) A (b) B (c) C (d) D	93
4.25	FIB images showing wear track after pin-on-disk wear testing of (a)(b) plan view; (c) cross-sectional view for specimen A	95
4.26	FIB images showing wear track after pin-on-disk wear testing for specimens (a) B (c) C (e) D in plan view; (b) B (d) C (e) D in cross-sectional views	97

List of Tables

<u>Table</u>	<u>Description</u>	<u>Page</u>
2.1	Processing parameters and coating properties [23]	9
2.2	The effect of pulse frequency on average grain size [24]	13
2.3	Hardness of CrN with different substrate bias voltage measured with a 10mN load Berkovich indenter [25]	14
2.4	The effect of pulse frequency on mechanical properties [26]	16
2.5	Structural parameters for common phases in the Cr-N system [2, 27-29]	16
2.6	Mechanical properties of CrCN with different C ₂ H ₂ flow rates [30]	22
2.7	Hardness and coefficient of friction of different Cr-C compounds [48]	22
3.1	Deposition conditions of the Cr and Cr(C)N layers	43
4.1	The actual thickness and deposition rate of four Cr(C)N coatings	52
4.2	The peak positions and elemental concentrations in four Cr(C)N coatings by survey etch with a 120s surface clean	54
4.3	The elemental concentration in Cr(C)N coatings by survey etch with a 300s surface clean	57
4.4	Inter-planar spacing (d-spacing) calculated using XRD results	62
4.5	Inter-planar spacing (d-spacing) calculated using SAED for specimen A	66
4.6	Inter-planar spacing (d-spacing) calculated using SAED for specimen B	67
4.7	Inter-planar spacing (d-spacing) calculated using SAED for specimen C	67
4.8	Inter-planar spacing (d-spacing) calculated using SAED for specimen D	68
4.9	Roughness (Ra)* and feature size* for the four Cr(C)N coatings	74
4.10	Summary of values of H, E, H/E and H ³ /E ² for the four Cr(C)N coatings	76
4.11	Ratio of indentation depth to total thickness of Cr(C)N coatings using a 8mN of load	77
4.12	UMIS data for Specimen A	83

4.13	UMIS data for Specimen B	83
4.14	UMIS data for Specimen C	83
4.15	UMIS data for Specimen D	83
4.16	Total depth of each load for each sample	85
4.17	Ratio of indentation depth to thickness at loads of 100mN to 300mN	85
4.18	The thickness of four Cr(C)N coatings after wear testing	98

Chapter 1 Introduction

Chromium coatings have a wide range of applications in industry, such as internal combustion engine components, hydraulic cylinders, rolls and machine tools [31]. However, hexavalent chromium used in electrochemical processes has been found to be carcinogenic [23]. Therefore, an alternative coating, chromium nitride, is being investigated. Chromium nitride (CrN) has been widely used for industrial applications due to its outstanding properties including oxidation, corrosion and wear resistance [1, 32-34]. These properties can be strongly influenced by the microstructure of the coating that, in turn, depends on the deposition conditions used. Relevant microstructural features include composition, crystallographic orientation, lattice defect density and grain size [33].

Recently, ternary Cr-X-N coatings have been explored in order to further improve the properties of these coatings relative to binary CrN. This is because CrN has a relatively high coefficient of friction. Compared with other chromium nitride-based coatings, chromium carbon-nitride (CrCN) coatings have been less widely studied. In previous studies, it has been reported that the addition of carbon into CrN coatings causes both an increase in hardness and a decrease in the coefficient of friction [35, 36]. To study the influence of carbon in CrN coatings, the role of carbon on the coating microstructure needs to be understood. There are three well known stable chromium carbides: cubic Cr_{23}C_6 and orthorhombic Cr_3C_2 and Cr_7C_3 [37]. However, in practice, only CrN and Cr_2N has been clearly identified in these CrCN coatings, but Cr_{23}C_6 or Cr_7C_3 has been theoretically predicated to be present [38]. Further, detailed microstructural studies of CrCN coatings are required to understand the influence of C on CrN.

The aim of this project is to investigate the microstructure and mechanical properties of CrN coatings, with respect to additions of carbon, deposited on a M2 steel substrate using unbalanced magnetron sputtering. In previous research, Cr(C)N coatings have been studied for their microstructure and tribological properties. However, the exact role of carbon in these coatings and the deformation mechanisms operating are not clear. To improve coating reliability and service life in industry, deformation mechanism in these Cr(C)N coatings need to be understood.

This thesis is organized in the following structure: In chapter 2, an introduction to CrN-based coatings, CrCN and the principles of the characterization methods used are presented in the literature review. In chapter 3, a detailed experimental procedure in this thesis is described. This chapter starts with the deposition method used followed by compositional and microstructural characterization, mechanical and tribological characterization and deformation mechanism characterization. The effect of carbon on the microstructure and mechanical properties, as well as tribological properties, was measured by X-ray photoelectron spectroscopy (XPS), X-ray diffraction (XRD), atomic force microscopy (AFM), focused ion beam (FIB) microscopy, transmission electron microscopy (TEM), scanning electron microscopy (SEM), pin-on-disk tribometer, Hysitron triboindentation and UMIS nanoindentation. Chapter 4 contains the results of these experiments together with discussion compared to other workers. Chapter 5 provides a general discussion for the effect of carbon doping in the Cr(C)N coatings. A brief summary and future research directions are presented in chapter 6.

Chapter 2 Literature review

2.1 Overview

CrN-based coatings have been widely used as protective coatings for industry applications such as engine components. Depending on the deposition parameters used, Cr-N based coatings can exhibit a wide range of microstructures and properties. It has been reported that the microstructure and properties of CrN-based coatings can be tailored by adding specific elements. Since the microstructure of these coatings has a significant effect on their performance, many researchers have studied the effect of processing variables and composition on the structure and properties of CrN-based coatings [6, 25, 33, 36, 39-41]. In Cr-N coatings, three phases are observed: body centered cubic (BCC) Cr, hexagonal (HCP) Cr₂N and face centered cubic (FCC) CrN.

The microstructure and mechanical properties of CrN and CrCN can be controlled by the deposition conditions used. To improve the reliability of these coatings, understanding the relationship between structure and deformation behaviour is necessary. From indentation studies, the deformation behaviour of these coatings are investigated. In this chapter, an overview of CrN-based coatings and CrCN coatings with respect to their microstructure, properties, deposition methods and characterization are provided.

2.2 CrN thin films

2.2.1 Cr-N Equilibrium phase diagram

Cr-N-based coating systems usually comprise one, or both, of two phases: CrN and Cr₂N. Depending on a range of deposition parameters, such as deposition rate, applied bias voltage, substrate temperature, and gas pressure, CrN-based coatings can exhibit a wide range of different microstructures and phases (i.e. α -Cr, δ -CrN and β -Cr₂N) [25, 32, 34].

An important coating property that can be strongly affected by changes in microstructure is hardness. For example, Hurkmans noted that hardness may vary from 10 to 22 to 16 GPa corresponding to a change in phase composition from a Cr to a Cr₂N to a CrN-dominated microstructure with increasing nitrogen partial pressure during processing [33, 42]. That is, Cr₂N is the hardest phase.

As can be seen in Figure 2.1, a eutectic reaction ($L \rightarrow \alpha\text{-Cr} + \beta\text{-Cr}_2\text{N}$) occurs in the Cr-N equilibrium phase diagram at a temperature of 1640°C and a composition of 13.4 at. %N. The $\alpha\text{-Cr}$ single phase is stable up to 1800°C with a maximum solid solubility of nitrogen at 4.36% at a temperature of 1640°C. A mixed phase comprising Cr and Cr₂N exists under the eutectic point. The Cr₂N phase is stable as a single phase from 30-32% and has a very slight temperature dependence. Two phases (Cr₂N and CrN) are stable below 1049°C for nitrogen concentrations over 32 at. %. The CrN single phase exists as a line compound at around 50 at. %N.

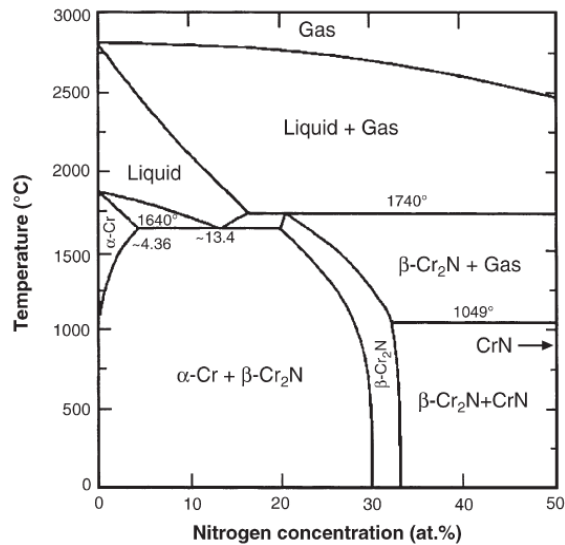


Figure 2.1: Equilibrium phase diagram for the Cr-N system [1, 2]

In Figure 2.2, it is shown that the N concentration in deposited CrN_x coatings increases with the nitrogen partial pressure in the deposition chamber. Three solid phases are clearly shown: body centered cubic (BCC) Cr, hexagonal close packed (HCP) Cr₂N and face centered cubic (FCC) CrN [28]. Cr₂N is stable over a range of nitrogen partial pressures from 7.5 to 9.5 %. This shows that single phase Cr₂N is stable across only a very narrow region of N₂ concentrations. As the N₂ partial pressure increases to 20 %, the phase composition shifts towards CrN.

the N concentration in CrN_x reaches and remains at 50 at.%, a value that leads to the formation of stoichiometric CrN [2]. Thus, to obtain single phase CrN coating, a high nitrogen partial pressure is needed.

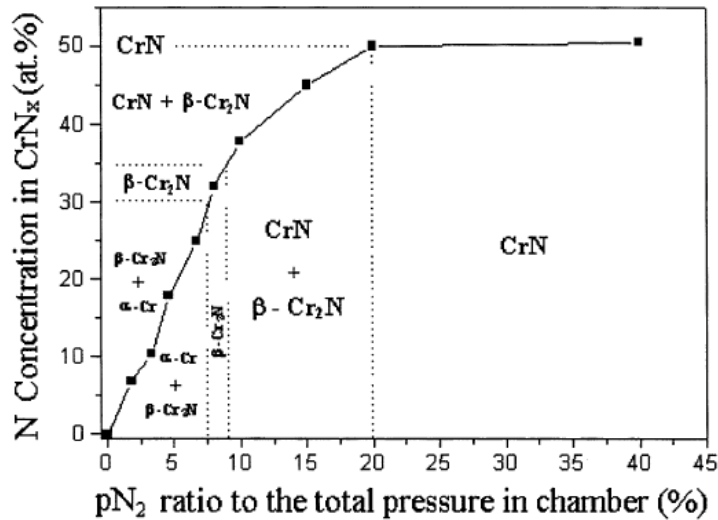


Figure 2.2: N concentration in CrN_x ($0 \leq x \leq 1$) vs. the ratio of nitrogen partial pressure to the total gas pressure in the sputtering chamber [2]

2.2.2 Film deposition methods

CrN can be produced either by physical vapour deposition (PVD) or chemical vapour deposition (CVD). However, the precursors to CVD processes are solid, which are less efficient in controlling the flow of reaction gases during deposition [43]. In PVD processes, the structure and the properties of the coating are strongly dependent on ions bombarding the growing film [3, 44, 45]. The ion current energy and density can be controlled by applying a substrate bias voltage and pulsing frequency [3, 45-47]. Common PVD methods used for CrN deposition eg. cathodic arc evaporation and sputtering are discussed in more detail in section 2.2.1 and section 2.2.2. Furthermore, the effect of deposition parameters on the structure and properties of CrN-based films are discussed in detail in section 2.2.3 and section 2.2.4 below.

2.2.2.1 Cathodic arc evaporation (CAE)

In cathodic arc evaporation, the targets are mounted on the each side of the cathode (Figure 2.3). The substrate is placed in the center of chamber, which is under vacuum, and rotated. A high current, low voltage arc strikes the cathode that generates a highly energetic emitting area on the cathode surface, known as the cathode spot. This cathode spot is an intense source of electrons and metallic ions which are accelerated into the vacuum [48]. The inert gas and reactive gas introduced into the chamber form a compound with the plasma on the substrate surface [5, 41]. The high power density of the arc results in a high degree of ionization. Arc deposition is often used because high plasma ionization can be generated which can lead to higher density coatings [49].

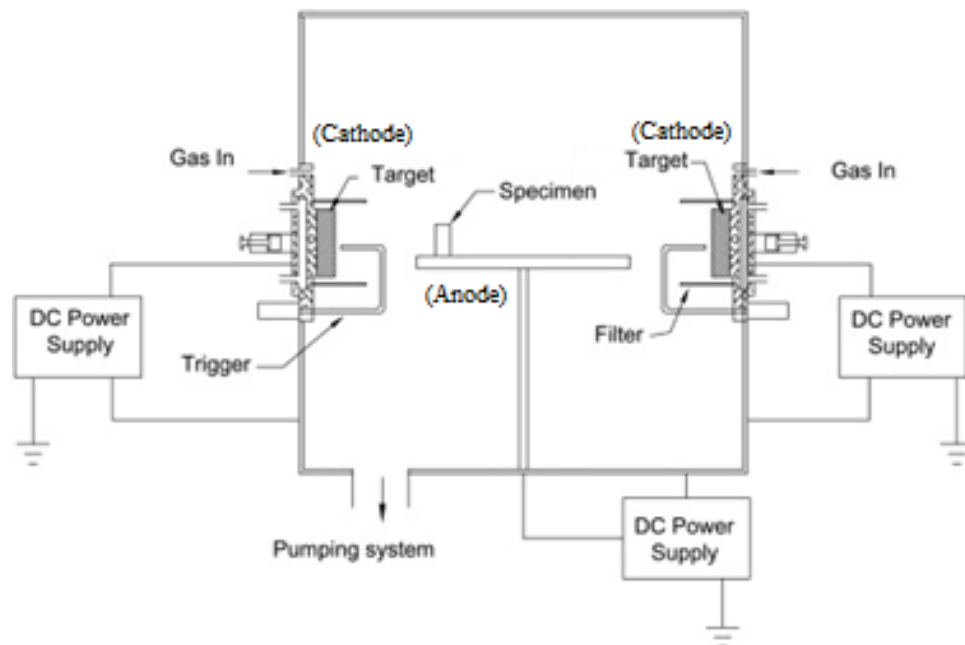


Figure 2.3: A schematic diagram of a cathodic arc evaporation system

2.2.2.2 Sputtering

Sputtering is one of the most common physical vapor deposition (PVD) method used in industrial applications due to its versatility. In the basic sputtering process, a target is bombarded by energetic ions generated in a glow discharge plasma. The bombardment process causes the removal of target atoms, which then condense onto the substrate as a thin film [3]. The secondary electrons emitted from the target maintain the plasma. However, drawbacks of the sputtering process include low deposition rates, low ionization efficiencies in the plasma and a high substrate heating effect. This has been overcome by the development of magnetron sputtering and unbalanced magnetron sputtering (Figure 2.4) which are discussed below [3]. Compared to evaporation, sputtering this method provides a simpler approach to control film properties, but more damage to the surface coating may occur [50, 51].

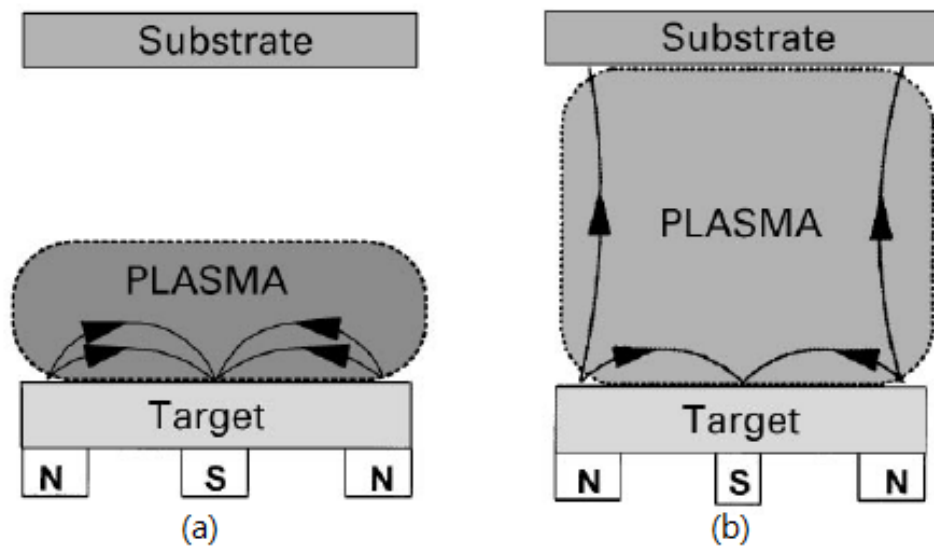


Figure 2.4: A schematic diagram of (a) Magnetron sputtering
(b) Unbalanced magnetron sputtering [3]

Magnetron sputtering

In the magnetron sputtering process (see Figure 2.4 (a)), a magnet is placed behind the target to increase the path length of the sputtered ions [52]. The plasma cloud in magnetron sputtering is, thus, confined to the target region. Consequently, the substrate outside of this region is located in an area with a very low plasma density. Although the energy of the bombarding ions can be increased by increasing the negative bias applied to the substrate, this can lead to defects in the films, such as microvoids and microparticles and high residual stresses in the coating [3].

Unbalanced magnetron sputtering

The unbalanced magnetron sputtering process is a further improvement on the conventional magnetron sputtering process and is used to obtain higher density films. In the unbalanced magnetron sputtering process (see Figure 2.4 (b)), the magnetic field of the outer ring poles is relatively stronger than the central pole. In this case, some of the magnetic field lines from the outer poles are oriented directly toward the substrate, rather than toward the central pole. Therefore, the plasma is no longer confined to the target region and some of the ions are biased towards the substrate directly without external bias [3].

2.2.2.3 Effect of deposition on structure

It has been shown by many studies that the microstructure of Cr-N based coatings can be controlled by the deposition conditions. The influence of deposition parameters such as substrate temperature, substrate bias voltage, partial pressure of reactive gases and total pressure on coating microstructure has been investigated by many researchers [4, 24, 26, 27, 29, 40, 53-57]. These changes in microstructure then affect the resultant properties of the coating.

As shown in Table 2.1, over a range of substrate temperatures and flow rates, different phases are formed with different preferred orientations [23]. For example, at both 200°C and 400°C, an increase in nitrogen flow leads to a drop in the deposition rate. At 400°C, the deposition rate decreases from 0.85 $\mu\text{m h}^{-1}$ to 0.75 $\mu\text{m h}^{-1}$ as the nitrogen flow increases from 0 vol.% to 5.7 vol.%. This then leads to the formation of Cr_2N . The deposition rate remains constant at around 0.7 $\mu\text{m h}^{-1}$ for nitrogen flow rates between 5.7 vol.% and 9.5 vol.%. The deposition rate is decreased when the nitrogen flow rate is over 9.5 vol.%, which correlates to the formation of CrN. The coating deposited with a nitrogen flow of 15.7 vol.% leads to a coating comprising CrN with a (200) preferred orientation; while the coating deposited with a nitrogen flow of 22.1 vol.% results in a CrN coating with a (111) preferred orientation.

Table 2.1: Processing parameters and coating properties [23]

Temperature (°C)	Nitrogen flow (vol. %)	Deposition rate ($\mu\text{m h}^{-1}$)	Phases	Preferred orientation
Room temperature	0	0.8	Cr	-
200	0	0.82	Cr	-
	7.1	0.7	Cr	-
	9.5	0.71	Cr_2N	(111)
	15.7	0.55	CrN	(200)
400	0	0.85	Cr	None
	5.7	0.75	Cr and Cr_2N	Cr_2N , (111)
	7.1	0.68	Cr_2N and CrN	Cr_2N , (111)
	9.5	0.70	Cr_2N and CrN	Cr_2N , (111)
	15.7	0.50	CrN	(200)
	22.1	0.40	CrN	(111)

Nitrogen partial pressure

Many researchers have noted that an increase in nitrogen partial pressure during deposition leads to a rise in the content of nitrogen in the coatings [5]. As shown in Figure 2.5, X-ray diffraction patterns show a very sharp peak for elemental Cr (with 0 % N_2) which is consistent with a Cr (110) preferred orientation. When a small concentration of N_2 is added, the strong Cr (110) peak disappears. This is because the incorporated N atoms reduce the grain size in the film and the preferred orientation

disappears [2]. When more N_2 is added, broad and weak peaks from Cr_2N (111) and Cr_2N (200) are observed. This indicates that the Cr starts to transform to Cr_2N . This occurs over a range of N_2 partial pressure ratios from 0.5 % to 8 %. This is due to a transformation in the coating microstructure through a mixture of Cr and Cr_2N . As the N_2 partial pressure ratio increases further to 8%, a peak for Cr_2N (002) is observed confirming the formation of this phase [2]. However, Wei et al. noted that other researchers observed a (111) peak for Cr_2N rather than a (002) peak over this pressure range [23, 29]. For N_2 concentrations of 10-15 %, a broad and weak CrN (200) peak is also observed in addition to the Cr_2N (002) peak. As the nitrogen partial pressure increases to 20%, the appearance of strong CrN (111) and CrN (222) peaks are observed which confirm the formation of stoichiometric CrN [27].

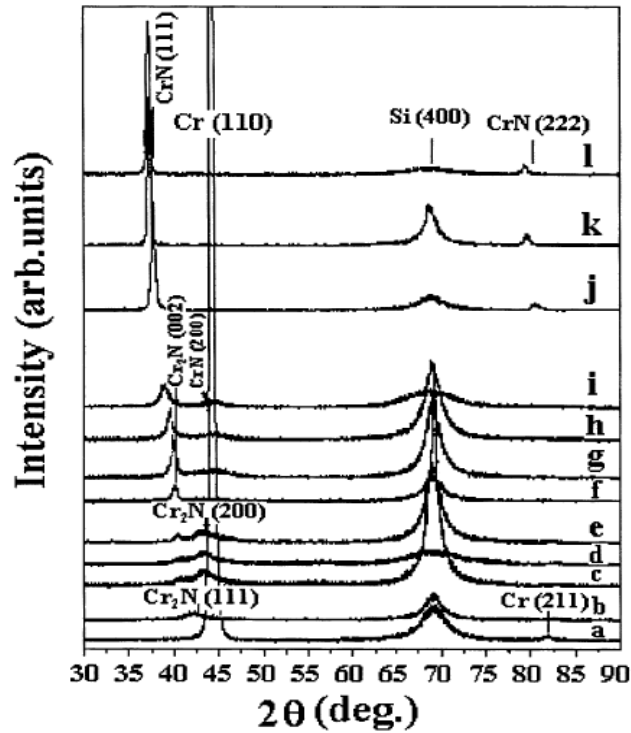


Figure 2.5: X-Ray diffraction patterns of as-deposited CrN_x films with different pN_2 ratio to total pressure (%): (a) 0 % (b) 0.5 % (c) 1.0 % (d) 2.0 % (e) 5.0 % (f) 8.0 % (g) 10 % (h) 12.0 % (i) 15.0 % (j) 20.0 % (k) 30.0 % (l) 40.0 % [2]

Wei et al. also noted that the peaks for both Cr_2N (002) and CrN (111) shifted to smaller diffraction angles with increasing N_2 partial pressure due to either increasing compressive stress in the film or the incorporation of N enlarging the lattice unit cell [2].

Substrate bias voltage

Figure 2.6 shows x-ray diffraction patterns for CrN deposited at different bias voltages. The figure shows the (111), (200), (220) and (311) peaks for CrN deposited at voltage bias of -50V. However, the (111) peak disappears at a voltage bias of -100V. Other researchers also found that the preferential crystal lattice orientation changes from (111) to (200) and (220) with increasing negative bias voltage [40, 53]. This has been associated with variations in grain size [4]. According to the Scherrer formula, the grain size can be estimated from the width of the examined diffraction peak. The average grain size of CrN deposited at $V_B=-50V$ was calculated to be 80nm, while the average grain size of CrN deposited at $V_B=-100V$ was 20nm. More information about the Scherrer formula is described in section 4.4.

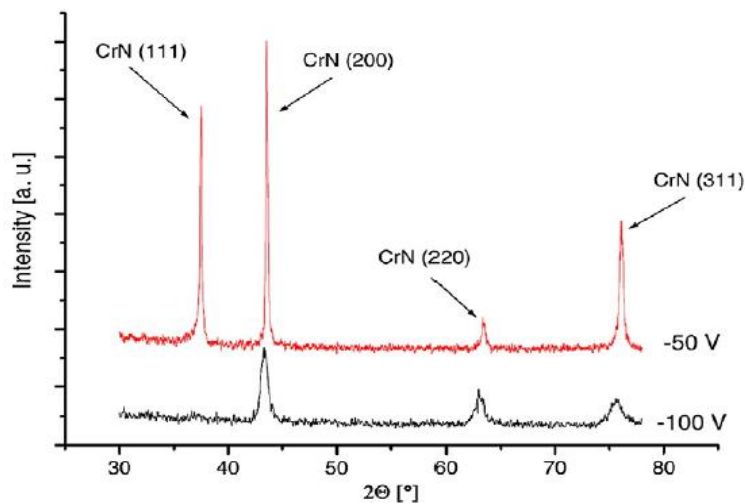


Figure 2.6: X-ray diffraction patterns for CrN films deposited at different bias voltages [4]

Other researchers found that the grain size of CrN decreases and the morphology changes from a granular structure to a columnar structure with increasing negative substrate bias voltage [24]. It is also well known that increasing substrate bias voltage results in a higher energy of the incident ions. As a result, both nucleation rate and the mobility of adatoms increase leading to a finer-grained structure. However, the atoms growing from the film are also re-sputtered. Therefore, the re-sputtering effect on the growing film decreases the deposition rate [53, 54].

Substrate temperature

The growth conditions of a coating are controlled by thermodynamics and kinetic restrictions, which depend on the substrate temperature and the energy of incident atoms at the substrate surface. If thermodynamic mechanisms dominate, the (100) orientation of CrN occurs preferentially due to it exhibiting the lowest surface energy ($\gamma_{(111)} > \gamma_{(110)} > \gamma_{(100)}$). If kinetic mechanisms dominate, the (111) orientation occurs preferentially [55].

As described above, CrN grains can exhibit two preferred orientations: the (111) orientation and the (220) orientation. The ratio of (111) to (220) can be expressed by the parameter of texture coefficient. In Figure 2.7, texture coefficient as a function of the substrate temperature for chromium nitride is shown. At temperatures below 350°C, the (220) preferred orientation is dominant. At 350°C, the (111) preferred orientation appears and becomes dominant at 470°C. This is because the mobility of adatoms increases with substrate temperature.

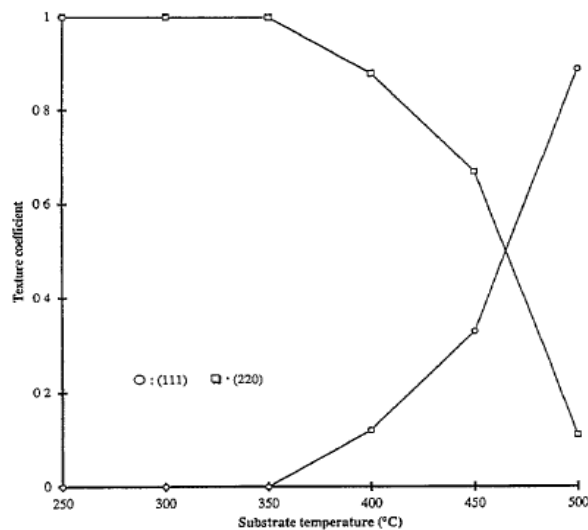


Figure 2.7: The effect of substrate temperature on texture coefficient of CrN [5]

Pulse frequency

As shown in Table 2.2, the CrN grain size decreases with increasing pulse frequency. The data shown in Table 2.2 are for a coating deposited by DC reactive magnetron sputtering at 300°C and a substrate bias voltage of -290V. It is believed that a reduction in grain size is caused by ion bombardment biasing the substrate [24]. More surface defects are produced with increasing pulse frequency due to the increasing ion flux resulting in a higher energy of incident ions. Further, the dominant orientation of CrN transforms from (200) to (220) with a higher pulse frequency [26].

Table 2.2: The effect of pulse frequency on average grain size [24]

Pulse frequency (kHz)	Average grain size (nm)
2	11.59±0.08
20	6.77±0.11

2.2.2.4 Effect of deposition conditions on the properties of CrN

Nitrogen partial pressure

As shown in Figure 2.8, the hardness clearly increases at very low partial pressures of nitrogen in the reaction chamber. With increasing nitrogen pressure, hardness and modulus increase until a plateau is reached at a pN₂ value of around 15 %, which is considered to be the hardest phase for CrN_x coatings. As shown earlier in Figure 2.2, this coating consists of a mixed phase with CrN and Cr₂N both present. Due to this two phase structure, the CrN exhibits very fine grains (≤ 7 nm) resulting in higher hardness [5]. The structure of Cr₂N transforms from a coarse structure to a fine structure with increasing nitrogen content resulting in higher hardness [56]. With further increases in nitrogen pressure, the hardness decreases due to the formation of the softer CrN relative to the formation of the harder Cr₂N. The reason for this is that the covalent bonding in Cr₂N is stronger than CrN, but the covalent bonding in CrN is stronger than the metallic bonding in Cr.

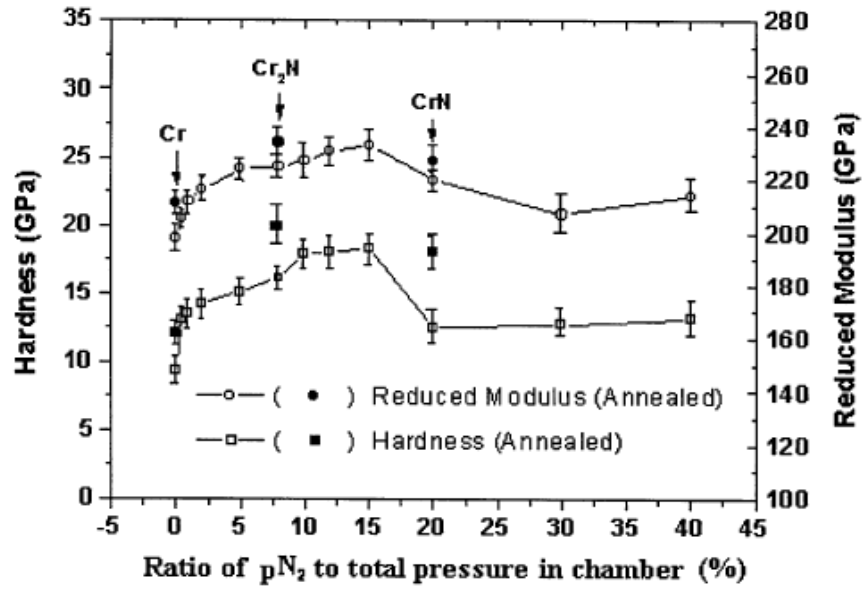


Figure 2.8: Hardness and reduced modulus of CrN_x as a function of nitrogen partial pressure ratio to the total pressure [2]

Substrate bias voltage

Table 2.3 shows the effect of substrate bias voltage on the hardness of CrN. With a lower substrate bias voltage, a lower hardness is obtained. As the bias voltage increases to $V_s=100$, the hardness increases to about 29GPa. However, the hardness decreases slightly with higher bias voltages (over 200V).

Table 2.3: Hardness of CrN with different substrate bias voltage measured with a10mN load Berkovich indenter [25]

V_s (V)	Hardness (GPa)
20	17.5 ± 1.4
50	24.7 ± 0.4
100	29.0 ± 0.7
200	27.3 ± 0.6
400	27.6 ± 1.9

Odén [25] noted that an increase in the substrate bias voltage resulted in the formation of lattice defects, such as dislocations and a smaller columnar grain width. This enhances the hardness of the coating. With further increases in substrate bias voltage over 100V, the microstructure of the coating contains a larger grain column width and lower lattice defect density resulting in lower hardness [25]. Similar trends were reported by Lee et al. [24]. It is believed that increasing bias voltage leads to higher surface mobility of adatoms and a denser surface layer. However, when the bias voltage increases to a very high level, the very high-energy bombardments create many large defects, such as voids and cracks, in the film resulting in lower hardness.

Substrate temperature

As shown in Figure 2.9, the hardness increases gradually with increasing substrate temperature [5]. This is because an increase in substrate temperature leads to higher mobility of adatoms. A change in texture from (220) to (111) at higher substrate temperatures results in higher hardness. This is because the (111) orientation has the highest atomic packing density in the FCC structure [57].

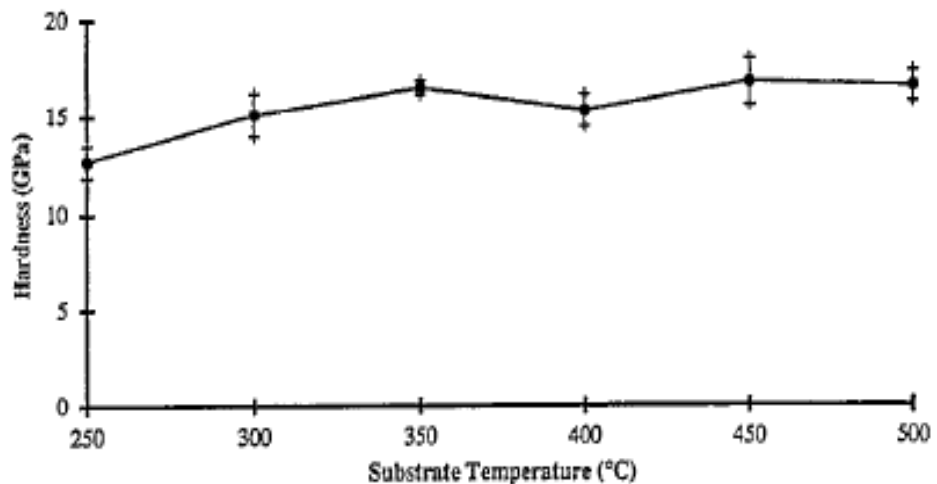


Figure 2.9: The effect of substrate temperature on hardness of CrN at the deposition conditions: $pN_2=1.6$ Pa, $V_s=-100$ V and $I_{arc}=80$ A [5]

Pulse frequency

As shown in Table 2.4, hardness increases from 20.9 GPa to 22.2 GPa with increasing pulsed frequency from 2kHz to 20kHz due to the decreasing grain size (described in section 2.2.3). Nevertheless, the hardness decreases from 22.2 GPa to 19.9 GPa when the pulsed frequency increases from 20 kHz to 50 kHz. It is believed that the hardness decrease at a pulsed frequency of 50kHz is due to the formation of cracks that weaken the coating [26].

Table 2.4: The effect of pulse frequency on mechanical properties [26]

Pulsed frequency (kHz)	Hardness (GPa)	Elastic modulus (GPa)
2	20.9	225
20	22.2	239
50	19.9	223

2.2.3 Structure of CrN-based phases

The microstructure and properties of the three phases (Cr, Cr₂N and CrN) in CrN-based coatings are summarized in Table 2.5 [2, 27-29]. The lattice constant for Cr₂N depends on nitrogen content, and therefore a range of lattice parameters is found [28, 56]. In the Cr-N system, β -Cr₂N is found to be the hardest phase and α -Cr the softest [2, 27-29].

Table 2.5: Structural parameters for common phases in the Cr-N system [2, 27-29]

Parameters	α -Cr	β -Cr ₂ N	CrN
Crystal system	BCC	HCP	FCC
Lattice parameter a,c (nm)	a=0.288	a=0.2742-0.2770, c=0.4349-0.4474	a=0.417
C _N (at. %)	0	33±2	50
Hardness (GPa)	1.35-10	15-27	11-15
Young's modulus (GPa)	132-180	220-270	210-244

In the bulk form, elemental Cr exhibits a body centered cubic (BCC) with a lattice parameter of 0.288nm. Cr₂N has a hexagonal closed-packed (HCP) structure with lattice parameters of around a=0.277nm and c=0.447nm depending on the nitrogen content (See Figure 2.10(a)). CrN exhibits a NaCl type structure with a lattice parameter of 0.417nm with nitrogen atoms occupying the octahedral holes in the chromium lattice (See Figure 2.10 (b)). As CrN has a faced centered cubic (FCC) structure (See Figure 2.10 (c)), the (111) planes in CrN consist of alternating nitrogen and chromium layers, whereas the (200) and (220) planes in CrN consist of both nitrogen and chromium atoms [4, 40].

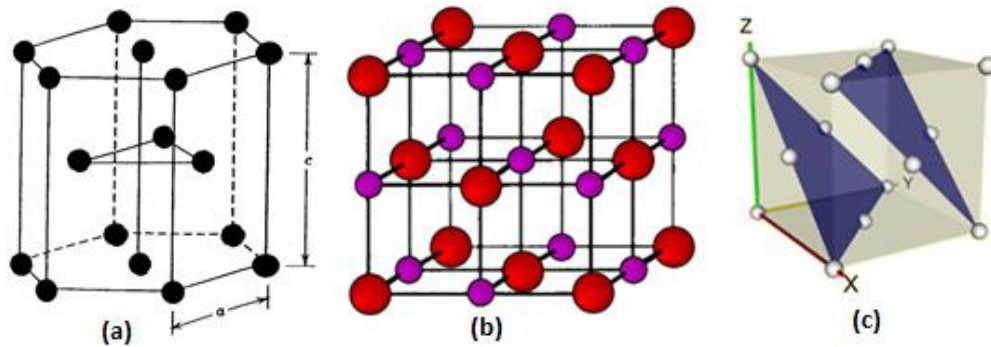


Figure 2.10: A schematic diagram of (a) HCP structure (b) NaCl structure (c) (111) plane of FCC

An example of the three different crystal structures in the Cr-N system can be seen in the transmission electron microscope study shown in Figure 2.11. In this study a Cr/CrN multilayered structure was deposited on a titanium substrate using a plasma-assisted physical vapour deposition (PAPVD) vacuum arc method. Bright field (BF) TEM images show the cross-section of the coating including the substrate and the entire coating thickness (Figure. 2.11 (a)). Selected area diffraction patterns (SADP) taken by TEM from specific areas of the CrN coating show reflections corresponding to different crystal structures (BCC for Cr; FCC for CrN; HCP for Cr₂N) (Figure. 2.11 (b)).

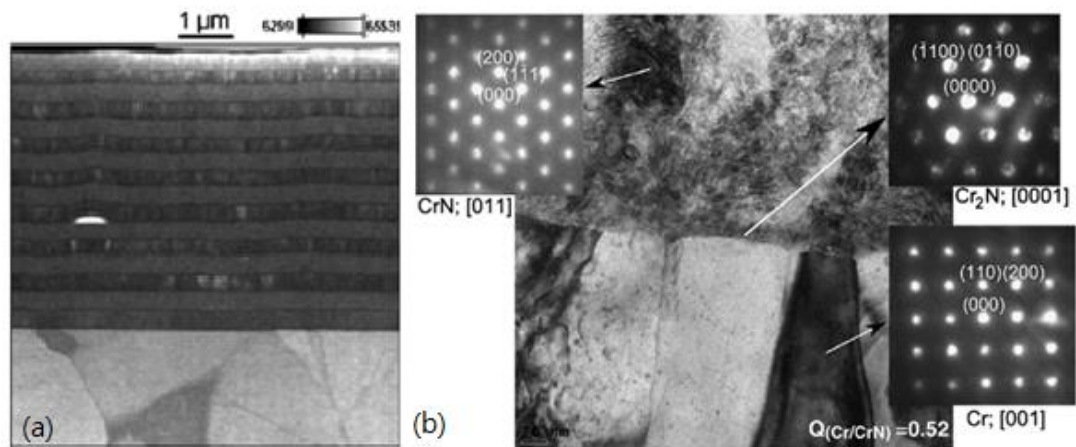


Figure 2.11: Bright field TEM images of (a) Cr/CrN multilayer coating on a titanium substrate (b) the interface between Cr and CrN layers with electron diffraction patterns for Cr, CrN and Cr₂N [6]

In the bright field TEM images, the phase with the higher atomic weight displays darker contrast images than the phase with a lower atomic weight. In Figure 2.11 (a), the darker layer is the chromium layer and the lighter layer is the chromium nitride layer as confirmed by energy-dispersive X-ray spectroscopy (EDS) mapping. In Figure 2.11 (b), the hexagonal Cr₂N phase is observed at the interface between the Cr and CrN layer. Both Cr and CrN phases exhibit a columnar structure. Era et al. found similar data and noted that the Cr₂N coating reveals a dendritic structure [56]. The grains of the CrN phase are less clearly visible compared to the grains of the Cr phases. This is because the grains of CrN are finer than Cr [6].

2.2.4 Properties of CrN

CrN films have been widely used as wear-resistant coatings. Therefore, most of the research performed on CrN coatings has focused on its mechanical properties, such as hardness and elastic modulus. Hardness is a characteristic of a material expressing its resistance to permanent deformation, such as the capacity to resist scratching, abrasion, penetration or indentation. Elastic modulus is a characteristic of material implying the ability to resist plastic deformation under an external stress. The hardness and the elastic modulus of CrN coatings range from 10 to 31 GPa and 220 to 400 GPa, respectively, depending on the deposition conditions, as described earlier [25, 33, 40, 58].

2.3 CrCN thin films

Sometimes CrN coatings cannot satisfy wear resistant applications under specific conditions, due to its high coefficient of friction (typically about 0.7) [8]. To reduce the coefficient of friction of CrN coatings, doping with carbon is being investigated. Chromium carbon nitride (CrCN) coatings are becoming more and more important for wear resistance applications due to their increased hardness and improved wear performance relative to CrN.

Graphite is commonly used as lubricant because of its low coefficient of friction. Many authors have noted that the influence of carbon in chromium nitride includes a change in hardness, adhesion, stress, oxidation resistance and coefficient of friction [59]. However, compared to other chromium nitride-based coatings, CrCN has been less well studied [8, 30].

2.3.1 Microstructure of CrCN thin films

As can be seen in Figure 2.12, diffraction peaks shift to lower 2 theta angles with increasing carbon content for a range of compositions where carbon is added to replace nitrogen. This correlates with additional carbon atoms being dissolved into the CrN lattice to replace nitrogen atom sites and thus reducing the lattice constant [7, 41]. However, Pengfei noted that the additional carbon that is dissolved into the CrN coating cannot replace the nitrogen, but rather change the original structure of CrN. The carbon thus makes the coating transform from a crystalline phase to an amorphous phase [8]. Consistent with this, Pengfei and Tong [8, 41] noted that when carbon is doped into these coatings, the intensity of the diffraction peaks become lower and broader. The coatings transform from crystalline to amorphous and the grain size gradually decreases. Polcar et al. [38] noted that Cr, CrN, Cr₂N and some Cr carbide phases would be expected to form in CrCN thin films. In this study, Polcar used reactive arc deposition from a Cr target in an Ar and N₂ atmosphere with a C₂H₂ reactive gas in a working pressure of 0.1 Pa and a substrate temperature of 220°C. However, in practice, Polcar noted that only Cr₂N can be clearly recognized because that the XRD peaks were too

weak for a detailed analysis. There are three well known chromium carbides which have three stable phases: cubic Cr_{23}C_6 and orthorhombic Cr_3C_2 and Cr_7C_3 [37]. However, these have not been observed experimentally.

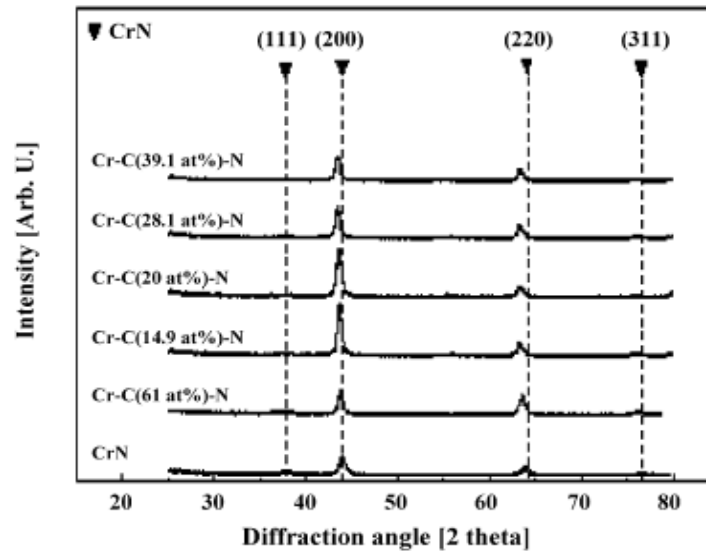


Figure 2.12: X-ray diffraction patterns of CrCN coatings with various carbon contents [7]

Figure 2.13 shows atomic force microscope (AFM) images of Cr(C)N coatings deposited with different carbon target currents by reactive unbalanced magnetron sputtering deposition. In binary CrN (Figure 2.13 (a)), the grains are cobblestone-like stacked with a feature size around $0.2 \mu\text{m}$. With increasing the carbon target current to 0.3A , the feature size is decreased to $0.1 \mu\text{m}$. When the carbon target current is further increased to 0.9A , these features are not visible and the surface appears to be very smooth. This is because the carbon elements doped in the coating inhibit the crystal growth of CrN. Associated mechanical tests performed by these workers showed that C additions reduced the coefficient of friction and increased hardness [8].

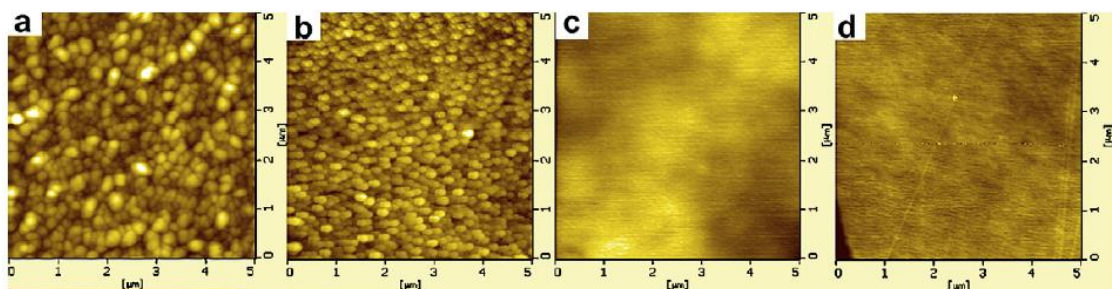


Figure 2.13: Two-dimensional AFM plan view images of Cr(C)N coatings (a) $I_C=0 \text{ A}$ (b) $I_C=0.3 \text{ A}$ (c) $I_C=0.9 \text{ A}$ (d) $I_C=1.5 \text{ A}$ [8]

In Figure 2.14 (a), the TEM image shows that the binary CrN phase, prepared using reactive unbalanced magnetron sputtering deposition, exhibits a dense columnar structure and the SAED pattern reveals a clear crystalline structure. When a relatively small amount (4.72 at. %) of carbon is added (Figure 2.14 (b)), the width of the columnar grain structure decreases and the SAED pattern shows a series of concentric rings indicating a very fine grained structure. With more carbon doping (46.43 at. %) (Figure 2.14(c)), the coating exhibits a multilayered structure (identified as CrN/a-CN_x [60]) and the SAED diffraction rings broaden indicating the coating mainly exists in the amorphous state [8]. A multilayered structure of CrCN with high carbon doping (4.9 at. %, measured by field emission electron probe microanalysis) was also found by Tong [41] prepared using cathodic arc evaporation. Tong suggested that the multilayer was produced due to the decomposition of the reaction gas, C₂H₂ into carbon that was deposited onto the surface of the CrCN layer when the specimen was rotated to the opposite of the chromium target plasma region.

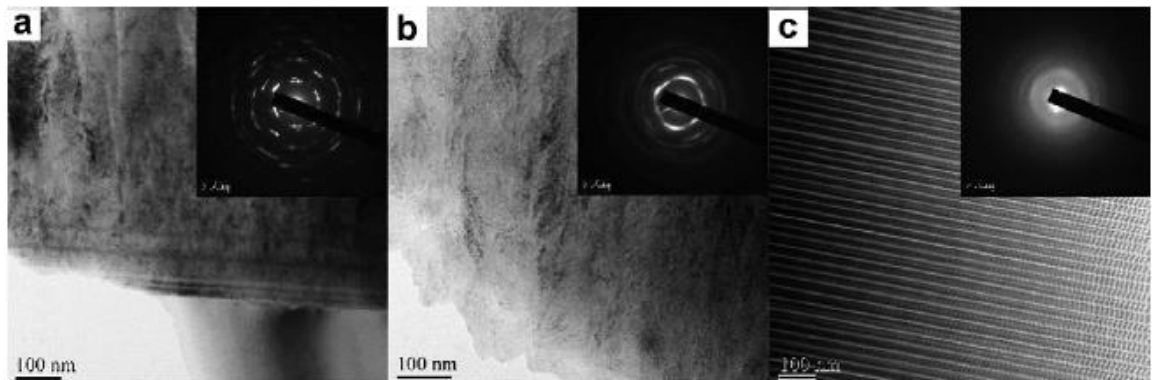


Figure 2.14: Bright field TEM images and diffraction pattern of CrCN coatings
(a) $I_C=0$ A (b) $I_C=0.3$ A (c) $I_C=1.5$ A [8]

2.3.2 Properties of CrCN thin films

The data in Table 2.6 was obtained on coatings produced by cathodic arc evaporation. Increasing the C₂H₂ flow rate leads to an increase in the carbon content which was measured by X-ray photoelectron spectroscopy (XPS). The coating thickness is generally increased with increasing C₂H₂ flow rate, which was measured by scanning electron microscopy (SEM).

Table 2.6: Mechanical properties of CrCN with different C₂H₂ flow rates [30]

C ₂ H ₂ flow (sccm)	Chemical composition (at. %)			Thickness (um)	Hardness (GPa)	Young's modulus (GPa)
	Cr	C	N			
0	64	0	36	3.40	23.9±1.2	292±9
6	53	6	41	3.52	25.8±2.3	297±15
24	46	22	30	3.57	25.4±1.8	305±10
48	47	28	23	4.05	28.1±1.3	30±9

As shown in Table 2.6, hardness broadly increases with increasing carbon content. However, the hardness drops slightly when the carbon content reaches around 22 at.% and increases with further increases in carbon content. A similar trend was also observed by Tong [41] and Choi [7]. They suggested that the hardness increases with increasing carbon content was due to the solid solution hardening effect of carbon atoms. The defects in the coating act as a barrier to dislocation propagation. Furthermore, Hu [8] suggested that the hardness increased because of the increasing content of sp² and sp³ bonds and C-Cr compound bonds in Cr(C)N coatings resulting in higher hardness. However, some researchers have found that the hardness decreases with increasing carbon content. The hardness decreases with increasing carbon content due to the carbon-containing coating exhibiting amorphous nanolayers [41]. Table 2.7 shows the hardness and coefficient of friction of a range of chromium carbide phases. A phase based on a mixture of amorphous carbon (or amorphous chromium carbide) has a low coefficient of friction that would be expected to improve tribological properties. Cr₇C₃ also has a relatively low coefficient of friction. However, Cr₃C₂ exhibits a high coefficient of friction, which, if present in CrN thin films would be unlikely to assist in improving wear behaviour.

Table 2.7: Hardness and coefficient of friction of different Cr-C compounds [61]

Structure	Hardness (GPa)	Coefficient of friction
C+a:CrC	10	0.06
Cr ₇ C ₃	16	0.12
Cr ₃ C ₂	20-22	0.46-0.52

The influence of carbon doping to CrN coatings on the coefficient of friction has been studied by many researchers. It has been reported that the coefficient of friction in CrN is relatively high and in a range from 0.54 to 0.7 [7, 8, 35] depending on different deposition parameters and characterization parameters. With increasing carbon content in the coatings, the coefficient of friction is decreased to a relatively lower range from 0.35 to 0.5 [7, 8, 35, 62]. All these studies observed that the coefficients of friction of these chromium nitride-based coatings decreased with carbon content. It has been suggested that this is because that the carbon exists as a sp^2 -bonded graphite phase which acts to reduce the coefficient of friction [8, 63]. However, Warcholinski [35] noted that the coefficient of friction decreased with a small addition of carbon (15 at. %); while coefficient of friction increased with further increase in carbon content from 20 to 30 at. % and then decreased again when carbon content reached 50 at. %. The coatings in this study were deposited using cathodic arc-evaporation method. It was suggested that an increase in the coefficient of friction in these CrN-based coatings was due to the present of Cr_3C_2 . Wang. [62] also found the similar tendency, that is the coefficient of friction is decreased with a small addition of carbon and then decreased with further carbon content. Wang suggested that an increase in the coefficient of friction was due to the formation of Cr_2O_3 in the coatings.

2.4. Characterization techniques

2.4.1 Scanning Electron Microstructure (SEM)

Scanning electron microscopy (SEM) is usually used to investigate the topographic features of a sample. A SEM produces images of a sample by scanning it with a focused beam of electrons. As, shown in Figure 2.15, the interaction of the incident electrons with the sample produces various interaction productions, e.g. emission of secondary electrons, back-scattered electrons, light emission, characteristic X-rays and other signals [9]. In the most common imaging mode, secondary electrons are detected by a secondary electron detector to produce very high-resolution images, with spatial resolutions of only a few nm. Backscattered electrons are generated more efficiently from high atomic number phases and so can provide compositional contrast.

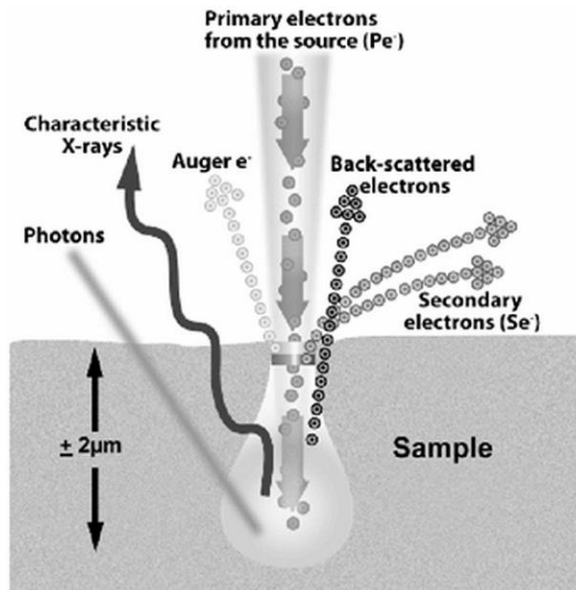


Figure 2.15: The interaction of incident electron beam with the specimen [9]

2.4.2 Focused Ion Beam Microscopy (FIB)

Focused ion beam (FIB) microscopy can be used to either obtain images using a low current beam or milling using a higher current beam (See Figure 2.16). The operation of a FIB instrument to obtain an image is broadly similar to a scanning electron microscope (SEM), but the FIB instrument uses a focused gallium ion beam with a beam energy of between 5 and 50 keV (typically 30 keV) instead of an electron beam [64-66]. The focused ion beam is accelerated to strike the sample and sputter the material resulting in milled trenches. The secondary electrons, generated by the interaction of the ion beam and the specimen, can be detected to form an image [67]. The sample is then tilted by $\sim 45^\circ$ to view the milled cross-section (See Figure 2.16).

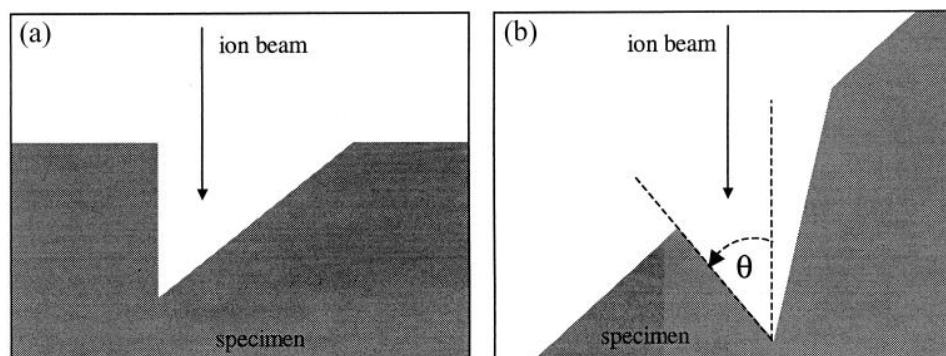


Figure 2.16: Preparing a cross-sectioning (a) ion beam for milling (b) tilting and imaging [10]

TEM sample preparation using FIB

The FIB instrument can be used as a precision sectioning tool, applied to cut sub-micron electron transparent slices of material for transmission electron microscopy (TEM) [67]. The specimen can be prepared by two methods: the “H-bar” technique or the “lift-out” technique [11, 68]. In the H-bar technique (Figure 2.17), the specimen is first cut from the bulk material about $2.5 \times 1.0 \times 0.5$ mm in dimension and then mechanically polished down to less than $100 \mu\text{m}$ in thickness to reduce FIB milling time [11]. In the lift-out technique pre-preparation is not required [69]. The FIB creates a membrane with a typical thickness less than 100 nm . The TEM specimen can be made directly from a bulk sample. However, the potential risks of the lift-out process are quite high. Therefore, recent studies have combined both the H-bar and lift-out techniques to make TEM specimens [11].

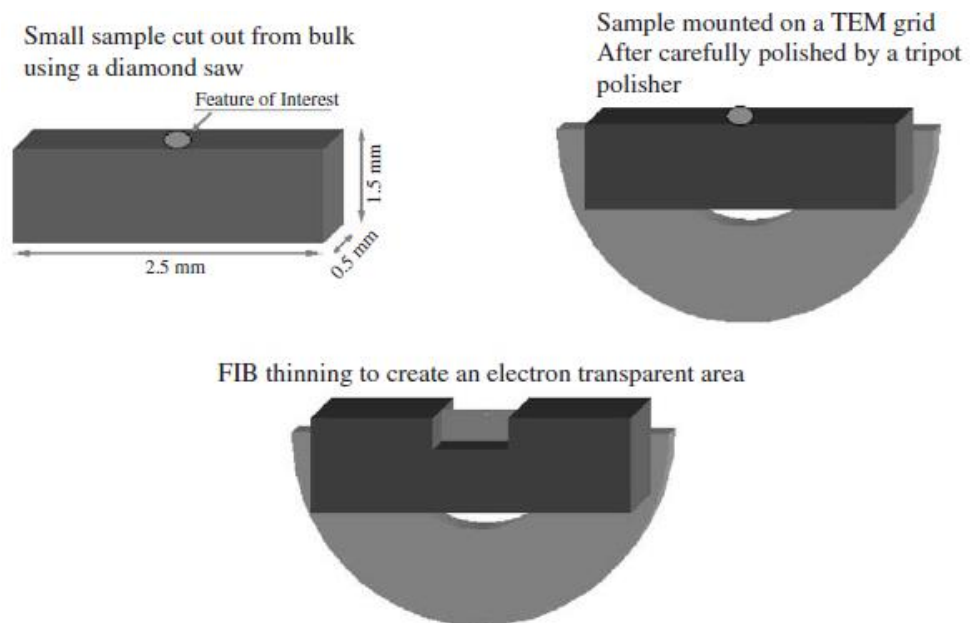


Figure 2.17: A schematic diagram of TEM specimen preparing by H-bar technique [11]

2.4.3 Dual-Beam Focused Ion Beam

In a conventional FIB, both imaging and milling are generated using a focused ion beam. Therefore, Ga^+ ions are potentially implanted into the specimen [65]. To overcome this type of damage using a conventional FIB, a technique called “Dual-Beam” FIB has been developed. A dual-beam FIB has both an ion gun and electron gun

that combine the milling abilities of a conventional FIB and high resolution imaging performance of a scanning electron microscope (SEM). As shown in Figure 2.18, the electron column is positioned vertically and the ion column lies at an angle of 52° to the electron column [12]. In a dual-beam FIB, both electron beam and ion beam are coincident on the same region of the specimen in the eucentric plane.

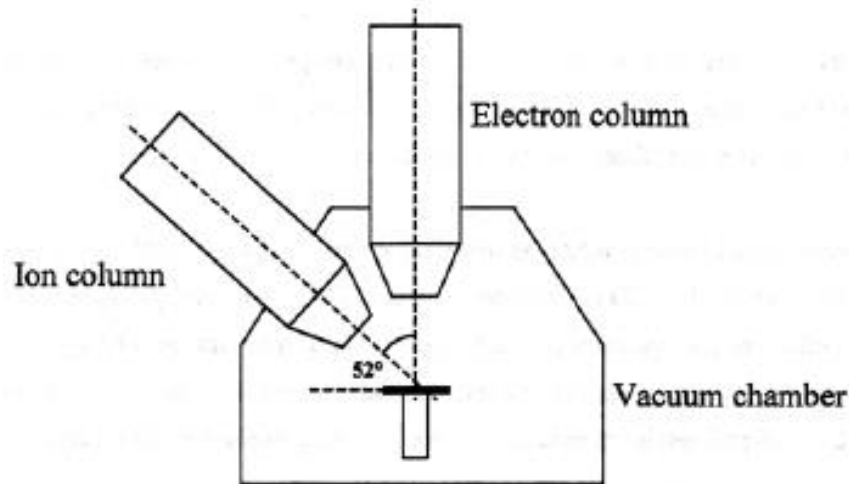


Figure 2.18: A schematic diagram of the dual-beam FIB [12]

2.4.4 Transmission Electron Microscopy (TEM)

Transmission electron microscopy (TEM) is used to characterize the microstructure of the specimen from localized regions of electron transparent specimens. In the TEM a high energy electron beam interacts with, and passes through, the specimen and results in a range of interaction products. These products can be detected and used to provide the information on the material [70]. Some of the important products are listed below:

- Transmitted unscattered electrons: these electrons pass through the sample without any significant interaction.
- Transmitted inelastically scattered electrons: these electrons pass through the sample and lose some energy through interactions such as x-ray production.
- Transmitted elastically scattered electrons: these electrons are diffracted by the crystalline sample, but have not lost any energy.
- Characteristic X-rays: these x-rays have energy and wavelength characteristic of the elements in the specimen.

The transmitted elastically and inelastically scattered electrons and unscattered electrons are used to produce TEM images. The TEM images of cross-section samples indicate the structure, thickness and morphology of the film. The high energy electrons that pass through a crystalline sample may be diffracted by Bragg scattering. The diffracted electrons may provide crystallographic information, such as crystal structure and orientation through the generated electron diffraction pattern. If the material is amorphous, the diffraction pattern consists of a series of diffuse concentric rings rather than discrete reflections.

The interaction of electrons with a specimen also generates characteristic x-rays which can be analyzed to provide chemical analysis. The characteristic x-rays can be used to determine qualitative and quantitative chemical analysis using an energy dispersive spectrometer (EDS). The element can be identified from peak energies in the spectrum and the composition can be determined from the integrated intensity of the various elemental peaks [52].

Imaging mode of a TEM

The imaging system of a TEM consists of four lenses: the objective lens, the diffraction lens, the intermediate lens and the projector lens. As shown in Figure 4.4, two modes of TEM operation are illustrated. The objective lens focuses the scattered electron beams at the back focal plane of objective lens to form the diffraction pattern and these beams reform the image at the image plane of the objective lens. The intermediate lens, diffraction lens and projector lens magnify this primary image to form a highly magnified image on the final screen. In imaging mode (Figure 2.19 (a)), the objective aperture is placed in the back focal plane of the objective lens and is used to select the beams to be used to form the image. In diffraction mode (Figure 2.19 (b)), a selected area aperture is inserted in the primary image plane of the objective lens to select the area from which the diffraction pattern is formed. This diffraction pattern allows the crystal structure of the specimen to be determined [13, 71].

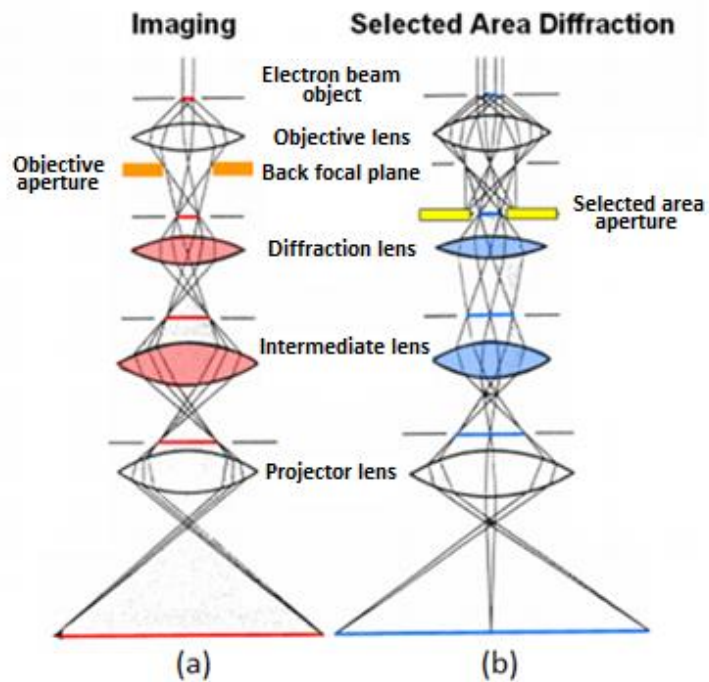


Figure 2.19: A schematic ray diagram for TEM showing (a) image formation (b) diffraction pattern formation. The back focal plane and the image plane of each lens are shown [13]

2.4.5 X-Ray Diffraction (XRD)

X-ray diffraction (XRD) is a non-destructive analysis method used to determine the structure and the composition of a sample [23]. X-ray diffraction is based on the elastic scattering of monochromatic x-ray photons by atoms in a periodic lattice. To determine an unknown structure requires three steps. First, the shape and size of the unit cell, such as interplanar d-spacings and the lattice structure, can be measured using Bragg's law. The number of atoms per unit cell can then be computed from the shape and the size of the unit cell. Finally, the positions of the atoms within the unit cell are deduced from the relative intensities of the diffraction lines [72]. When the crystal lattice is illuminated by X-rays, intense peaks of scattered radiation are observed as predicted from Bragg's law, as shown in Figure 2.20 [73, 74].

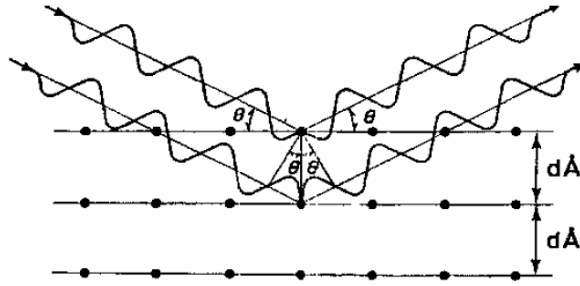


Figure 2.20: A schematic diagram showing Bragg's Law

$$\text{Bragg's law: } n\lambda = 2d\sin\theta$$

where n is the order of reflection, λ is the wavelength of the X-ray source (normally 0.154 nm for CuK α source), d is the interplanar spacing of the diffracting crystal and θ is the angle between the incident beam and the normal to the reflecting lattice plane (the Bragg angle).

The average size of individual grains in a thin film can be determined using the Scherrer formula from peak broadening in the X-ray diffraction pattern [23, 75].

$$\text{Scherrer formula: } L_c = \frac{K\lambda}{\beta \cos\theta}$$

where L_c is the calculated grain size, K = the shape factor = 0.9 - 1.3, λ is the X-ray wavelength, β is full width at half-maximum (FWHM)= 2θ and θ is Bragg angle.

In order to understand the preferred orientation of a crystal plane, a texture coefficient can be calculated to compare the observe peak relative intensities. Texture coefficients represent the texture of a particular plane ($h k l$). The texture coefficients of CrN can be calculated from the normalized XRD peaks with the following formula [53, 55]:

$$T(h k l) = \frac{I(h k l)}{I(1 1 1) + I(2 0 0) + I(2 2 0)}$$

where hkl represents the (111), (200) and (220)-reflections. The value of the texture coefficient indicates the intensity of a texture generated by grains oriented in a given (hkl) direction.

2.4.6 X-ray Photoelectron Spectroscopy (XPS)

Chemical bonding and elemental composition can be determined by XPS using a monochromatic Al K α X-ray source. The incident X-rays interact with the sample and this leads to the excitation of core state electrons (1s, 2s, 2p, etc.) with a kinetic energy (KE) that is measured experimentally. The kinetic energy of ejected photoelectrons gives qualitative and quantitative information and allows the determination of binding energy (BE) and numbers of emitted electrons respectively [76, 77].

$$BE = hv - KE$$

where $h\nu$ is the excitation energy of the incoming X-ray.

As shown in Figure 2.21, the XPS spectrum shows the chemical structure and the bonding state in a CrCN coating. The spectrum shows major peaks for Cr, C, N together with smaller peaks for O and Ar. The elemental content of the coating can be estimated by the ratio of the integrated area under the main peak and total integrated area under the spectrum modulated through a number of correction factors [8]. Detailed analysis of the elemental peaks allows the bonding state for a given element to be determined. For example, whether Cr exists in an elemental metallic state or is bonded to oxygen or carbon.

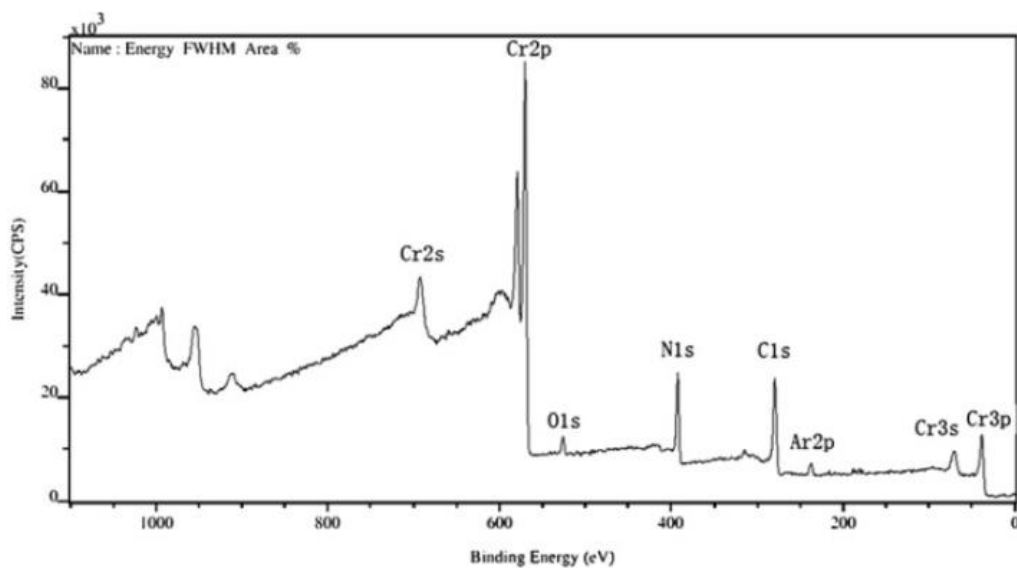


Figure 2.21: XPS spectrum of CrCN coating [8]

2.4.7 Atomic Force Microscopy (AFM)

Atomic force microscopy (AFM) is a very high-resolution form of scanning probe microscopy (SPM). AFM was developed to improve a limitation of its precursor, scanning tunneling microscopy (STM) that is, STM can only be used on conductive and semi-conductive surfaces. Unlike STM, AFM can also be used to study insulators [78]. An AFM scans the sample surface using a probe with a sharp tip, which is usually located at the end of cantilever; typically the tip has a diameter of 10nm. The cantilever bends and is deflected by forces generated between the tip and the sample surface, depending on local perturbations on the specimen surface. A detector measures the deflections of the cantilever to allow a computer to generate a three dimensional map of surface topography [79].

There are various interactive forces between the tip and the sample surface and the van der Waals force is the one most commonly associated with AFM [14]. As represented in Figure 2.22, in the contact region, the probe presents repulsive van der Waals force over a distance of a few angstroms (\AA) between the sample surfaces. In the non-contact region, the probe presents attractive van der Waals force at a distance of 10-100 angstroms (\AA) away from the sample surface. Tapping mode fluctuates between these two regions.

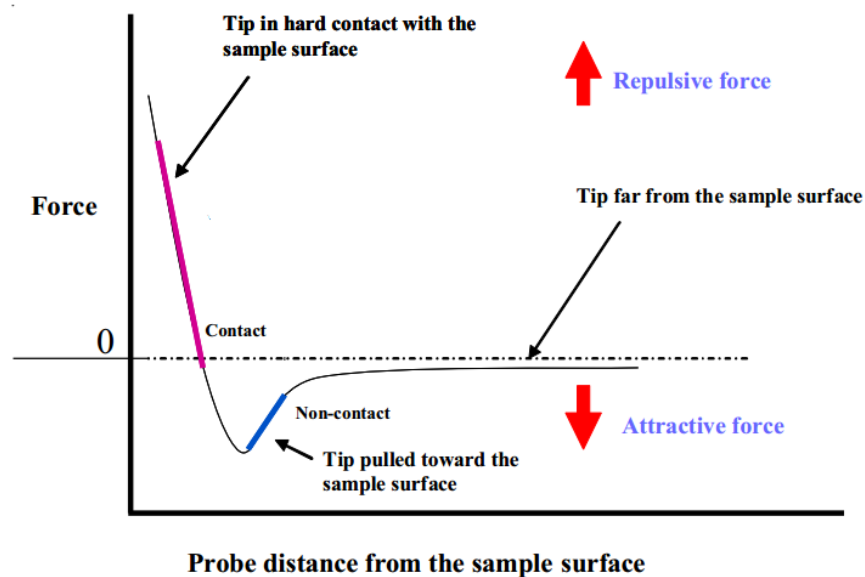


Figure 2.22: Interaction forces between tip and sample surface [14]

As shown in Figure 2.23, three primary AFM imaging modes are illustrated: contact mode, tapping mode and non-contact mode. Contact mode was the mode first developed for the AFM. In contact mode, the tip contacts the sample surface all the time. As the tip moves across the sample surface, the cantilever records changes in surface topography directly without oscillation [79]. However, imaging in contact mode is influenced by frictional and adhesive forces and this can damage the sample surface. In non-contact mode, the tip does not contact the sample surface. The tip is oscillated at its resonance frequency and the amplitude of the oscillation is typically constant. Therefore, non-contact imaging can be affected by surface contaminant layers and provides lower resolution information. Tapping mode is the most common mode because it takes advantages of both contact mode and non-contact mode. The tip oscillates and contacts the surface and then lifts off alternately. The amplitude of oscillation changes with sample surface topography [14]. It can reduce the extent of damage of the sample surface and provide high resolution imaging.

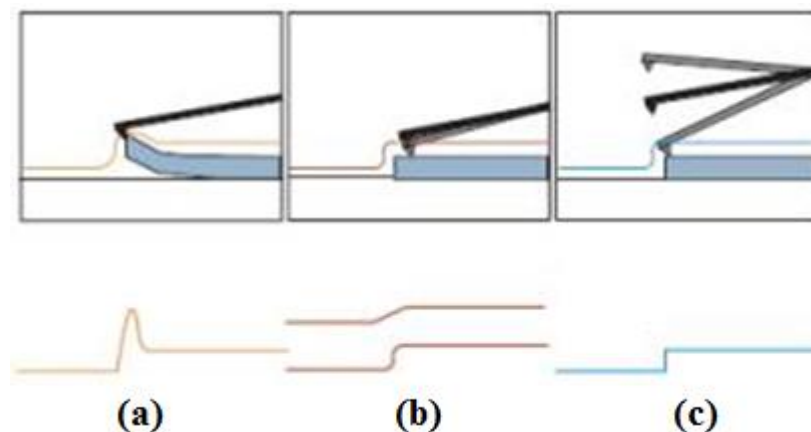


Figure 2.23: Comparison of (a) contact mode (b) non-contact mode (c) tapping mode [15]

2.4.8 Tribometry

Friction and wear are important problems in industry. A tribometer is used to characterize wear behaviour under controlled experimental conditions to investigate mechanisms of wear and determine parameters such as the coefficient of friction. There are many parameters which can affect wear behaviour, such as sample microstructure, temperature and humidity [80]. Pin-on-disk testing is the most widely used technique in wear testing which allows calculation of the coefficient of friction. It is based on the

principle of a pin that is pressed against a rotating disk. The coefficient of friction, μ , is determined by the ratio of the frictional force to the loading force on the pin. However, at the start of the test, the surface is usually smooth and flat, but later wear debris may accumulate on the surface and wear roughening may take place which can influence frictional behaviour [81].

2.5. Deformation and Fracture behaviour

To improve coating reliability, an understanding of the relationship between microstructure and deformation behaviour is important. The fracture behaviour of a coating can be investigated by nanoindentation with different loads and can then be characterized by methods such as focused ion beam microscopy. This section is divided into two parts. In the first part, a background to nanoindentation techniques is provided, including discussion of indenter types and the analysis of indentation data. The deformation behaviour of coatings under nanoindentation loading are discussed in the second part.

2.5.1 Nanoindentation

Nanoindentation testing is used to determine the mechanical properties of materials, including hardness and elastic modulus. The choice of indenter geometry has an influence on the indentation behaviour.

2.5.1.1 Indenters

Nanoindentation hardness tests are generally performed with either spherical or pyramidal (Vickers, Knoop and Berkovich) indenters. In practice, indenters are usually made from diamond due to its high hardness [82]. The most two popular indenter geometries for nanoindentation testing are discussed below: the Berkovich indenter and the spherical indenter.

Berkovich indenter

The three-sided Berkovich indenter with face angles of 65.3° is preferred over four-sided Vickers or Knoop indenters because it is easier to obtain a sharp tip [82, 83]. A sharp indenter causes yielding of the indented material at a lower load and, thus, permits measurements of the mechanical properties of very thin films [84]. It is thus easier to obtain more accurate data. Therefore, the Berkovich indenter is more frequently used to measure hardness than the spherical indenter. However, it is not as sensitive to detecting the transition from elastic to plastic behaviour. This can be confirmed in Figure 2.24. The unloading of the load-displacement curve shows that the recovery of the elastic deformation and residual plastic deformation in Berkovich indenter is smaller than in the spherical indenter [16].

Spherical indenters

The advantage of spherical indentation is the penetration of soft material can be controlled by the choice of indenter radius [83]. Also, the indentation created by the spherical indenter has a lower stress variation and smooth transition from elastic to plastic deformation. As shown in Figure 2.24, the elastic recovery measured by the spherical indenter is larger than that typically measured by a Berkovich indenter [16]. The formation of cracks and the delamination of a coating under loading are more readily observed by a spherical indenter [19]. As can be seen in Figure 2.25, pop-ins and pop-outs may occur during loading and unloading, respectively. Pop-ins may be caused by events such as crack nucleation and propagation. Pop-outs may be caused by events such as the dislocation motion or phase transformations.

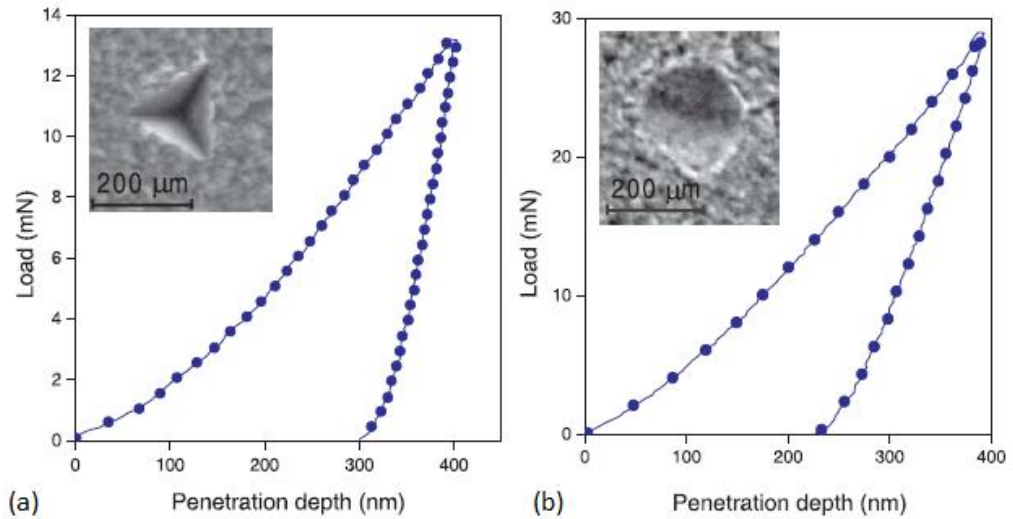


Figure 2.24: Load-indentation depth curve for a Cr coating measured with (a) Berkovich indenter (b) spherical indenter [16]

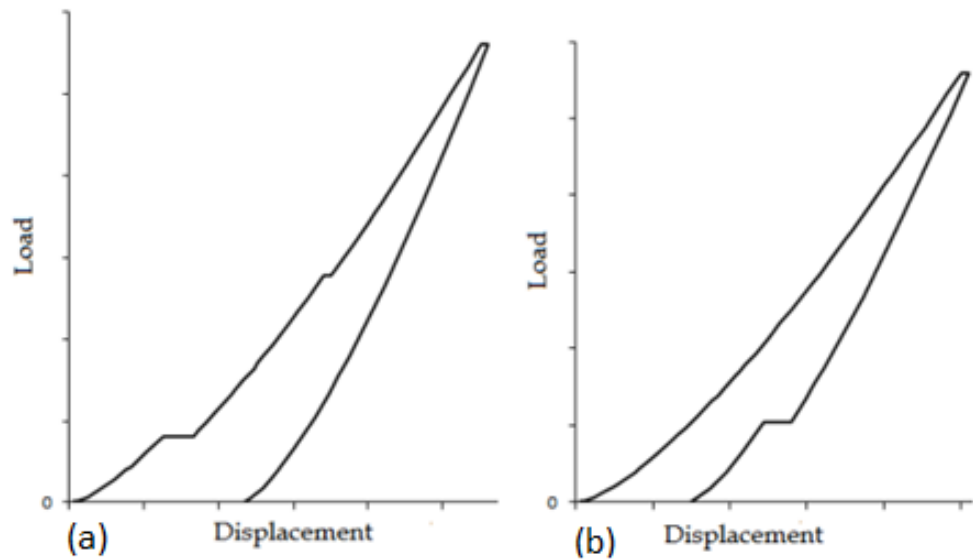


Figure 2.25: A schematic diagram of load-displacement curve of (a) pop-in (b) pop-out [17]

2.5.1.2 Analysis of indentation data

The experimental curve recorded during indentation shows the relationship between load (P) and displacement (h) (Figure 2.26). In the load-displacement curve, it can be seen that the maximum indentation depth is h_{\max} at a maximum load, P_{\max} . The loading curve exhibits elastic behaviour at the initial stage of loading and plastic behaviour at higher loads. The slope of the unloading curve during initial stages of unloading is defined as the unloading stiffness, S . Elastic recovery occurs during unloading and leaves a recovery depth, h_r . After the load is removed, there is a final indentation depth,

h_f , with residual plastic deformation. Typically, elastic modulus is determined by the contact area and the measured unloading stiffness. Hardness is measured from the contact area under maximum load [18, 85].

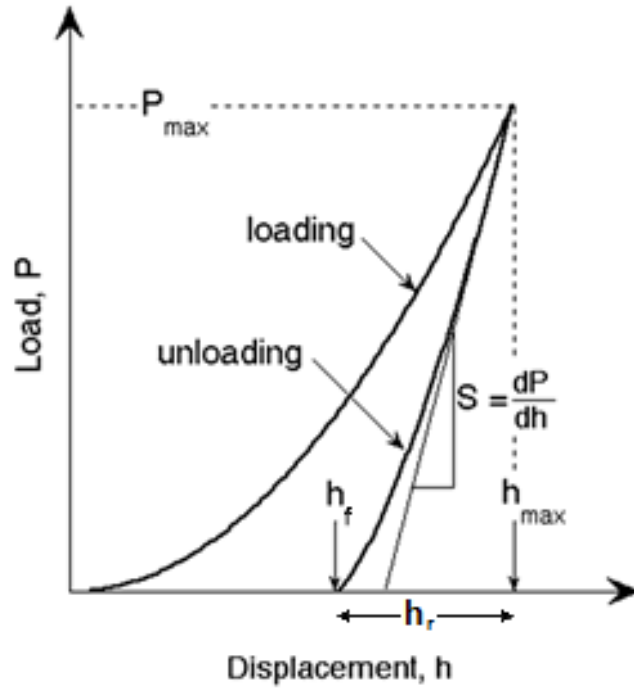


Figure 2.26: A schematic diagram of load-displacement curve for nano-indentation [18]

$$h_r = h_{max} - h_f$$

In conventional indentation testing, the contact area is determined as the size of the residual depth. To obtain more accurate values, the contact area is determined as the size of the contact area under full load. The shape of indenter tip and the depth of the penetration are also considered in a depth-sensing indentation test. The hardness, H , and elastic modulus, E , can be defined from the following expressions.

Indentation hardness, H , is defined as the indentation load, P , divided by the projected area of the contact, A .

$$H = \frac{P}{A}$$

The projected area of the contact, A is given by:

$$A = 24.5h_p^2 \quad \text{for a Berkovich indenter}$$

$$A = \frac{\pi d^2}{4} \quad \text{for a spherical indenter}$$

where h_p is the plastic depth of penetration and d is the diameter of the contact circle at full load [85-87].

The elastic properties of indented material, for example modulus, may be obtained from the unloading curve. The slope of the unloading curve is given by:

$$\frac{dP}{dh} = \alpha E^* \sqrt{A}$$

where α is the constant 1.167 and E^* is the effective modulus.

The effective modulus is related to the indenter and the indented material by means of the expression:

$$\frac{1}{E^*} = \frac{(1 - \nu_0^2)}{E_0} + \frac{(1 - \nu^2)}{E}$$

where E_0, E and ν_0, ν are the Young's modulus and Poisson's ratio of the indenter and the indented material.

2.5.1.3 Factors affecting nanoindentation test data

Piling up and sinking in

In indentation testing of an elastic material, the contact plane between the indenter and the indented material is not usually same as the original plane, but may change by either piling-up or sinking-in. The circle contact area above the original surface level is called “piling up” and below the original surface level is called “sinking in”, shown in Figure 2.27 [19]. The degree of the piling up and sinking in depends on the ratio of the initial yield strength, Y , and Young’s modulus, E [88].

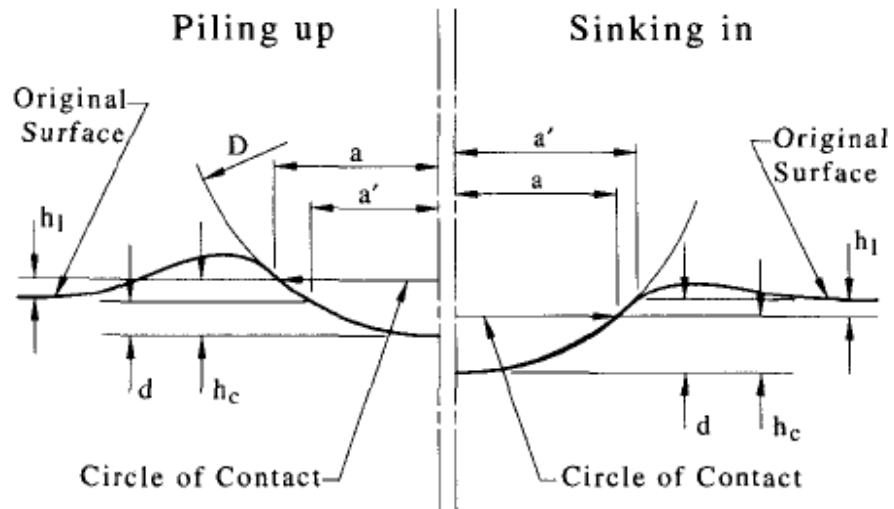


Figure 2.27: A schematic diagram of spherical indentation with piling up and sinking in [19]

2.5.2 Thin film cracking

Swain and other researchers described the deformation and fracture behaviour of films during spherical indentation [20]. They described three stages (See Figure 2.28). In the beginning of the loading process, the deformation is entirely elastic and reversible. Then, plastic deformation forms below the indented region which is irreversible. Eventually, plastic flow is established and fracture may occur [19, 20]. There are three common types of indentation cracks observed which are discussed below: ring cracks, radial cracks and lateral cracks.

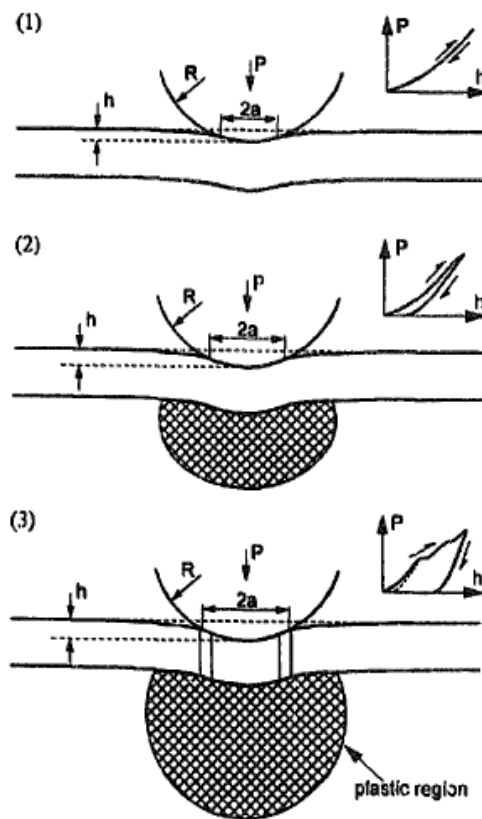


Figure 2.28: Principle of deformation behaviour for spherical indentation [20]

On the loading cycle (Figure 2.29 (a)-(c)), surface ring cracks are first to initiate at the periphery of the contact edge. With further loading, cone cracks are occasionally formed and median cracks develop beneath the indented area. On the unloading cycle (Figure 2.29 (d)-(f)), the median cracks close up due to compressive forces. The radial cracks occur at the interface between the coating and substrate and generate parallel to the load axis. When the ring cracks and radial cracks meet, lateral cracks can be generated parallel to the surface [21, 89].

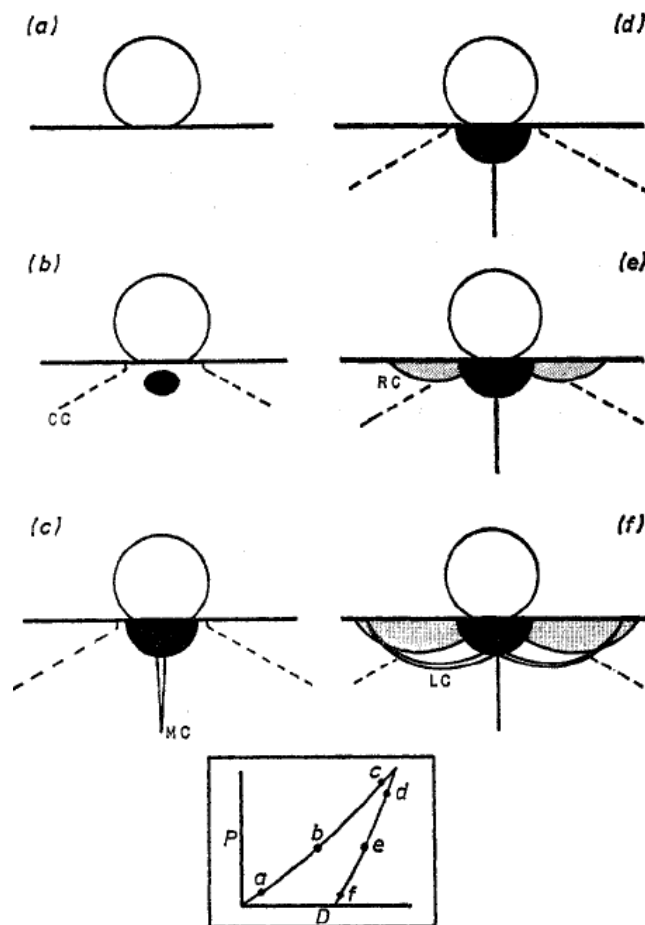


Figure 2.29: A schematic diagram of the cracking during loading and unloading with a spherical indenter [21]

2.6. Summary

Chromium nitride is widely used as a protective coating in industrial applications due to its high hardness and high resistance to corrosion and wear. CrN-based coatings exhibit a wide range of microstructures and properties depending on a range of deposition parameters, such as nitrogen partial pressure, substrate bias voltage, substrate temperature and pulse frequency. In the Cr-N system, the crystal structure transforms from BCC-Cr to HCP-Cr₂N to FCC-CrN with increasing nitrogen content. The hardness and elastic modulus of CrN-based films can be affected by parameters such as small variations in nitrogen concentration, a higher substrate bias voltage and a higher substrate temperature. However, increasing the nitrogen content to higher values leads to the lower hardness due to the transformation of Cr₂N to the slightly softer CrN phase.

Cr-X-N thin films have also been studied because CrN cannot satisfy certain specific requirements condition due to its high coefficient of friction. CrCN will be studied in this project because it is believed that C can lower the coefficient of friction of CrN. However, hardness and elastic modulus of these CrCN coatings are expected to increase with increasing carbon concentration. Moreover, the crystalline structure may potentially transform to an amorphous structure as a result of the presence of carbon atoms. So far, detailed microstructural studies of the effect of C on CrN-based coatings have not been performed.

To improve the reliability of a CrCN coating, understanding the relationship between the microstructure and fracture behaviour is necessary. By using nanoindentation, the deformation behaviour as a function of load will be understood from load-displacement curves and by FIB examination. To date, little is known about the deformation mechanisms operating in CrCN coatings under contact loading.

Chapter 3 Experimental Procedure

3.1 Introduction

This chapter describes the experimental procedures used in this study. The deposition procedure is explained in section 3.2. This is followed by the characterization procedures used including the compositional and microstructural analysis methods described in section 3.3 and the mechanical and tribological properties in section 3.4. The characterization methods used to analyse the deformation microstructure are detailed in section 3.5.

3.2 Material Deposition Conditions

The deposition process was performed at the Department of Mechanical and Biomedical Engineering of the City University of Hong Kong. Four Cr(C)N coatings were deposited using a closed field unbalanced magnetron sputtering ion plating system (UDP 650/6 system, Teer Coatings Ltd, UK) on AISI M2 high speed steel substrates (hardened to HRC62, Ra=0.01 μm after polishing).

Firstly, the vacuum chamber was pumped down to a background chamber pressure of 3×10^{-6} Torr (4.0×10^{-4} Pa). During deposition, an Ar working gas pressure was maintained at 1.3×10^{-3} Torr (0.17 Pa) with an Ar flow rate fixed at 30 sccm. The substrate was placed on the substrate holder with a rotation speed of 10 rpm, without external heating. The target-to-substrate distance was kept at 190 mm. There are 6 targets located symmetrically around the vacuum chamber ($\text{\O}650$ mm in diameter) with a Cr-C-C-Cr-C-C arrangement. The rectangular target size was 380 mm \times 175 mm \times 10 mm. The substrate holder was biased by an Advanced Energy Pinnacle Plus power supply, at a frequency of 250 kHz with a reverse time of 0.5 μs .

Prior to deposition, the substrate was sputtered cleaned by an Ar plasma at a bias voltage of -500 V for 30 minutes. A chromium interlayer of 0.3 μm was first deposited to enhance the adhesion of the coating to the substrate with a chromium target current of

5 A and a bias voltage of -80 V for 10 minutes. Next, the Cr(C)N layer was deposited by co-sputtering of graphite and chromium targets and introducing N₂ into chamber with a bias voltage of -80 V for 120 minutes. The nitrogen reaction gas was controlled by an optical emission monitor (OEM) with a setting at 70 % to regulate the reactivity of Cr²⁺ [90]. The different deposition settings for each deposition run are shown in Table 3.1.

Table 3.1 Deposition conditions of the Cr and Cr(C)N layers

Specimens (Batch number)	Cr interlayer	Cr(C)N top layer	
	Current applied to each Cr target (A)	Current applied to each Cr target (A)	Current applied to each C target (A)
A (398D)	5	5	0
B (387D)	5	5	1.5
C (393D)	5	5	3.5
D (396D)	5	5	4.5

3.3 Composition and Microstructure Characterization

Each sample was sectioned into three pieces for different characterization experiments using a Buehler IsoMet-1000 saw and then cleaned using acetone in an ultrasonic bath for 2 minutes.

3.3.1 X-ray Photoelectron Spectroscopy (XPS)

The composition and chemical state of the coating were analysed using a XPS survey scan and depth profiling (ESCALAB250Xi Thermo Scientific, UK) by using monochromatic Al K α radiation of energy 1486.68 eV at 150W (13kV x12 mA) with a 500 μ m spot size. All samples were analyzed at a photoelectron takeoff angle of 90°, which is defined as the angle between the surface normal and the axis of the analyzer lens [91]. The background vacuum of the XPS chamber was better than 2×10^{-9} mbar (2×10^{-7} Pa). The emitted photoelectrons were detected at a pass energy of 100 eV for the survey scan and 50 eV for the depth profiling region scan. Due to the high carbon content on the sample surface examined by the survey scan, depth profiling was used to

confirm the carbon content in the coating itself. Depth profiling was done using an Ar ion beam at 3 keV. An area of $2.5 \times 2.5 \text{ mm}^2$ was etched at a rate of 0.42 nm/s for 1610 seconds. The reference binding energy was taken as C 1s at 285.0 eV for adventitious hydrocarbons and the other elements were calibrated relative to this value [92]. The calibration of the XPS spectrometer was performed using the following standards: Au 4f₇ (83.96 eV), Ag 3d₅ (368.21 eV) and Cu 2p₃ (932.62 eV). Avantage software was used for instrument control and analysis, including quantification of data.

3.3.2 X-ray Diffraction (XRD)

The phase structures of Cr(C)N coatings were examined using X-ray diffraction (PANtical Empyrean, the Netherlands) at room temperature (25°C) using Cu K α radiation with a wavelength of 1.5418 Å. The diffractometer was operated at 40 mA and 45 kV. The XRD data were collected over the range of $2\theta = 30\text{-}90^\circ$ using a step size of 0.026°. HighScore Plus software was used for analyzing the data.

3.3.3 Atomic Force Microscopy (AFM)

The surface structure and roughness was analyzed using atomic force microscopy (AFM) (SPM Icon) operated in scanasyst mode. Scanasyst mode, is a proprietary name for tapping mode analysis. It operates with automatic optimization of imaging parameters including set-point, feedback gains and scan rate. The scan size was set to $5 \mu\text{m} \times 5 \mu\text{m}$ at a scan rate of 0.723 Hz. All images and the results were treated with a first order flattening protocol to remove any background slope in the surface topography. The surface roughness (arithmetic average roughness, Ra) (Figure 3.1) and the feature size of the Cr(C)N coatings were measured using the roughness function and section function of the AFM software, respectively.

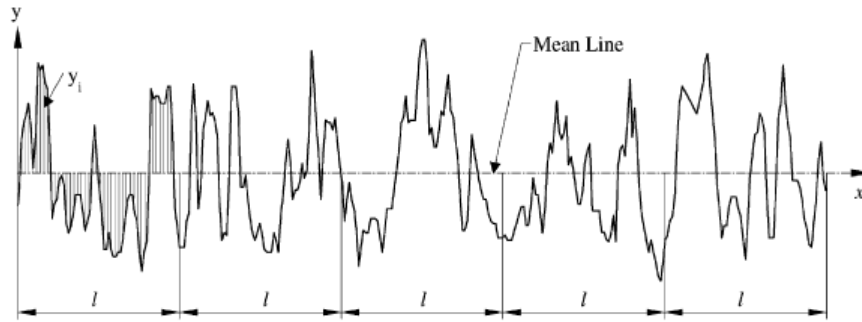


Figure 3.1 Definition of the arithmetic average height [22]

The surface roughness value, R_a , applied in this work is defined as the arithmetic average roughness. This is the one of the most widely used roughness parameters. It is defined as the average absolute deviation of the roughness irregularities from the mean line over one sampling length. The description of formula is described as follows [22]:

$$R_a = \frac{1}{n} \sum_{i=1}^n |y_i|$$

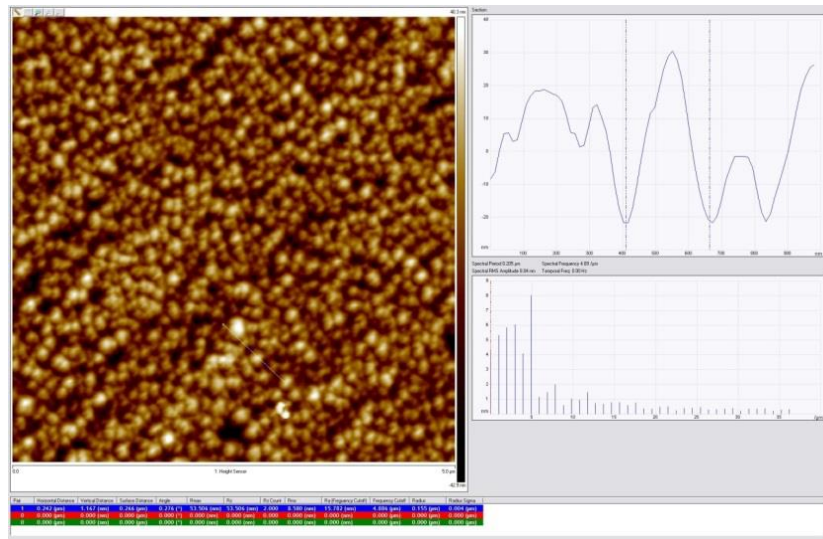


Figure 3.2: Section function analysis using an AFM

In the section function (Figure 3.2), a reference line was drawn in the area of interest. Then, the cross-section profile of the data along the reference line was provided. The feature size was measured by the gap between two lines at the edges of the feature.

3.3.4 Focused Ion beam (FIB) Microscopy

Analysis of the coating cross-section and the preparation of TEM specimens were obtained by focused ion beam (FIB) microscopy. This was performed using a FEI xP 200 FIB and xT Nova Nanolab 200 FIB as described in section 3.3.4.1 and section 3.3.4.2, respectively. Prior to examination samples were mounted on to an aluminum stub using silver-based glue and sputtered coated with gold to improve electrical conductivity of the sample surface for both instruments.

3.3.4.1 Cross-Sectional Imaging

Images of the coating cross-section, as well as the indents following indentation, were obtained using a FEI xP200 focused ion beam microscope. First, a rough mill of a trench $\sim 20\ \mu\text{m}$ by $8\ \mu\text{m}$ to a depth of $\sim 6\ \mu\text{m}$ was achieved using a high beam current of 2700 pA, followed by final clean-up mills using lower beam currents of 1000, 350 and then 150 pA. After milling, the stage was tilted to 45° for imaging using either a 70pA or 11 pA beam current.

3.3.4.2 TEM Sample Preparation

TEM specimens were prepared using xT Nova Nanolab 200 dual beam focused ion beam using the ex-situ lift out method [11]. A thin platinum layer was first deposited on the region of interest to protect the coating from damage during milling. Two trenches on both sides of the region of the interest were milled using a high beam current of 7 nA with stage tilt of 52° . The stage was then tilted to 7° to generate a L-shaped cut using beam current of 3nA. The stage was then tilted back to 52° with additional small angle modifications ($\pm 1.5^\circ$) and followed by clean-up mills for both sides using a lower beam current of 3 nA , 1 nA and 0.3 nA. Finally, a specimen membrane $\sim 100\text{nm}$ in thickness was prepared and then cut away from the trench using a rectangular pattern mill (Figure 3.3.4).

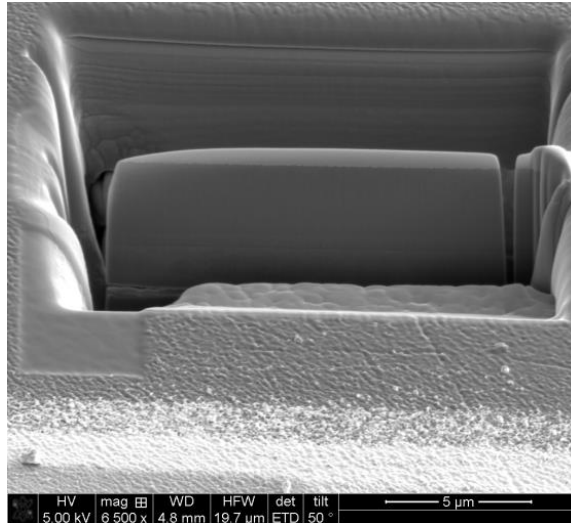


Figure 3.3: Dual beam FIB image taken during TEM specimen preparation

After FIB milling, the sample was moved to an ex-situ lift-out microscope. A thin electron transparent membrane was lifted-out using a glass needle attached to a micromanipulator with an optical microscope. The thin TEM foil was attracted by electrostatic force onto the tip of the glass needle and then placed on to a carbon-coated of 3mm diameter copper grid for subsequent TEM analysis [11].

3.3.5 Transmission Electron Microscopy (TEM)

The samples were characterized using a Philips CM200 field emission gun transmission electron microscope (FEG TEM). The microstructure was examined by bright field imaging. The crystal structure of the CrCN coatings was examined using selected area diffraction techniques. Elemental analysis was performed using energy dispersive spectroscopy (EDS) using point analysis, line scans and elemental mapping over the region of interest to investigate the distribution of elements in the sample.

3.3.6 Scanning Electron Microscopy (SEM)

In this study, the plan view images of the wear tracks were obtained using a SEM Hitachi S3400 scanning electron microscopy. Prior to examination, samples were mounted on to an aluminum stub using double side carbon tabs.

3.4 Mechanical and tribological properties Characterizations

In this project, the mechanical properties and tribological properties of the CrCN coatings were investigated by a Triboindenter (Hysitron, Inc) and pin-on-disk tribometer respectively.

The specimens for testing need to be flat and parallel to the workbench. Prior to testing, the bottom surface of the sample was first ground using 1200 grid sandpaper to reduce the influence of the roughness of the bottom surface of the substrate, and then cleaned using acetone in an ultrasonic bath for 2 minutes. The samples can then be placed directly on the workbench of the Hysitron directly using its magnetic substrate, i.e. M2 steel. For pin-on-disk tribometer testing, the samples were glued to the workbench by superglue because the samples were too small to fit in the sample holder.

3.4.1 Hysitron Triboindenter

Hardness and Young's modulus were determined using a Hysitron Triboindenter system, since it has the capability to perform indentation tests at very low loads. Therefore, it was possible to perform the indentation to less than 10% depth of the total coating thickness to avoid any influence from the substrate [82, 93]. Each sample was subjected to a load of 8mN using a three-sided pyramid diamond indenter tip (Berkovich type). Each sample was indented with a 3x3 pattern with a spacing of 20 μm between indents. The loading function was set into three segments: First, the load was increased from 0 to 8 mN over an interval of 10 seconds. Second, the load was held at 8 mN for 5 seconds to avoid creep behaviour. Third, the load was decreased from 8 to 0 mN over a period of 10 seconds. The hardness and elastic modulus were determined following the methods [82, 85] described in Section 2.5.1.2.

3.4.2 Pin-on-disk wear testing

The coefficient of friction was evaluated using a pin-on-disk wear testing with a loading 5 N at a sliding speed of 5 cm/s for 5000 cycles. The wear track was set up at a radius of 3 mm. As a counterpart, a ruby ball with a diameter of 6mm was used. The measurements were performed at ambient temperature in air at a humidity of 55-60 %. After pin-on-disk wear testing, the wear track was examined using both a FIB microscope and a SEM as detailed in section 3.3.4 and section 3.3.6.

3.5 Deformation behaviour characterization

Prior to testing, the undeformed samples were first ground using 1200 grit sandpaper to reduce influence of the roughness of the bottom surface of the substrate, and then cleaned using acetone in an ultrasonic bath for 2 minutes. The samples were then placed directly on the workbench of the UMIS directly using its magnetic substrate, i.e. M2 steel. After UMIS testing, the indented area was examined using a FIB microscope and TEM using the methods detailed in section 3.3.3 and section 3.3.5.

3.5.1 Ultra Micro-Indentation System (UMIS)

The deformation behaviour of the CrCN coating was investigated using a UMIS-2000 nanoindenter with a 5 μm radius spherical-tipped indenter. Indentation tests were performed with a layout file which was set to various loads of 100, 200, 300, 400 and 500 mN. Arrays of 8 indents with a spacing of 50 μm between them were performed at each load. The initial contact was set to 0.015 mN and the progression occurred using a square root progression of force. Each loading was performed with 100 increments for each loading and unloading cycle with a 0.1 second dwell time at each load increment. Once the maximum load was reached, it was held for 8 seconds to prevent thermal creep and then unloaded to 2 % of its maximum load.

Chapter 4 Result and discussion

4.1 Introduction

This chapter describes the characterization and testing of four Cr(C)N coatings in terms of their crystal structure, composition and microstructure, as well as their mechanical and tribological properties and microstructure following either indentation or wear testing.

The specimens were initially examined using FIB to generate cross-sectional images to observe their overall microstructure and measure the thickness of each of the coatings. The chemical composition and crystal structure of the coatings were characterized using XPS and XRD, respectively. Further, cross-sectional TEM specimens, prepared using FIB, were used to provide more detailed information of the coating microstructure, crystal structure and elemental distribution throughout the coating architecture. The surface roughness was measured by AFM. Mechanical properties, such as hardness and elastic modulus, were determined by a Hysitron Triboindenter using a Berkovich indenter. The coefficients of friction of the coatings were determined using a pin-on-ball tribometer. The deformation behaviour of the coating was investigated by UMIS nanoindentation using loads up to 500 mN and FIB analysis was used to examine the deformation microstructure.

4.2 Composition and microstructural characterization

4.2.1 Focused Ion Beam Microscopy

As can be seen in Figure 4.1, cross-sectional FIB images show the various layers in each sample. Each sample contains a chromium wetting layer exhibiting a columnar grain structure deposited directly on the M2 steel substrate. Adjacent to the chromium wetting layer, there is the Cr(C)N layer. The chromium wetting layer and the Cr(C)N layer both have grown perpendicular to the substrate surface.

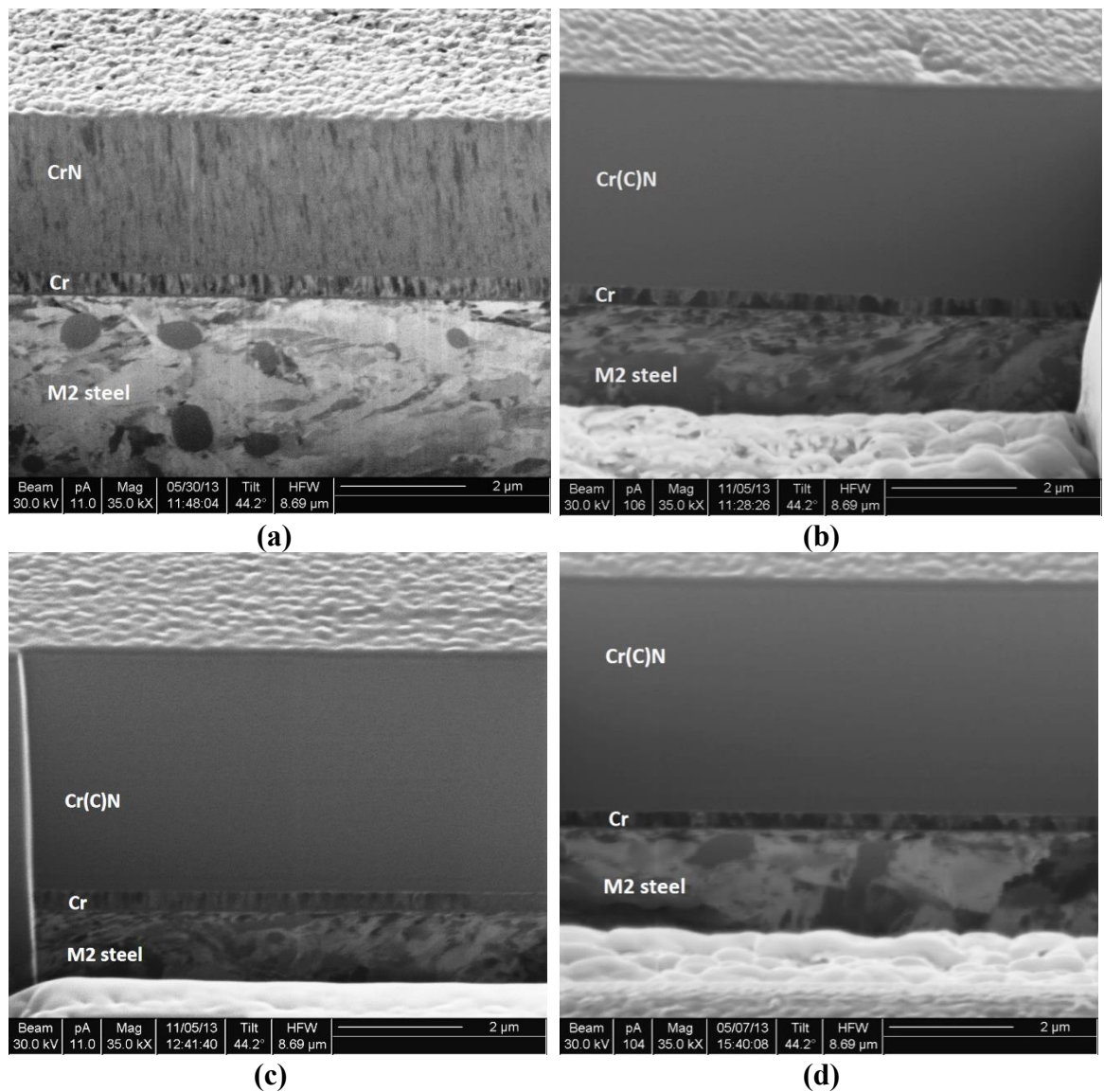


Figure 4.1: FIB images of cross-sections of the undeformed coatings (a) A (b) B (c) C (d) D

The CrN layer deposited on specimen A exhibited a fine-grained structure (grains are around 80 nm in width and typically 0.7 μm in length) compared to other Cr(C)N layers for specimens B, C and D, where no grain structure could be easily resolved using the FIB. This suggests that the carbon present in the Cr(C)N coatings for specimens B, C and D significantly refines the microstructure. As such, at this resolution, differences in microstructure for specimens B, C and D could not be readily distinguished. To investigate their microstructure in more detail, the samples were subsequently examined using TEM. The higher resolution images obtained by TEM are described later in section 4.2.4. where it is evident that all of the coatings contain fine columnar grains.

Coating thickness measurements were conducted on the FIB images. Since these were performed using a single beam FIB the sample stage was tilted by $\sim 45^\circ$. Hence, the measured thicknesses on the recorded images were corrected to provide an actual experimental thickness by dividing the values determined from the recorded image by $\cos 45^\circ$ [94]. The experimental coating thicknesses estimated from the cross-section FIB images are listed in Table 4.1. It can be seen that the thickness values increase with increasing graphite target current. This indicates a higher rate of deposition with increasing carbon content.

$$\text{Deposition rate} = \frac{\text{Coating thickness}}{\text{Deposition time}}$$

Table 4.1: The actual thickness and deposition rate of four Cr(C)N coatings

	A	B	C	D
Cr(C)N (μm)	3.61	5.25	5.62	6.48
Cr (μm)	0.49	0.50	0.46	0.46
Total (μm)	4.10	5.75	6.08	6.95
Deposition rate ($\mu\text{m}/\text{min}$)	0.030	0.044	0.047	0.054

4.2.2 X-ray Photoelectron Spectroscopy (XPS)

The chemical composition of the Cr(C)N coatings was measured using XPS. In initial studies analysis was performed following the application of a surface clean for 120 s. In the XPS survey scans (shown in Figure 4.2), peaks from Cr, C, N and O were observed from the specimens after this relatively short cleaning process. In addition, small Ar peaks were also detected from, all the coatings, in the survey scans shown in Figure 4.2. This is probably due to the Ar^+ ion in the cleaning process used, although the presence of an Ar working gas during the deposition process (glow discharge gas) cannot be discounted. It can be clearly seen that the intensity of the carbon peaks in the survey etch spectra increased from Specimen A to Specimen D; that is with increasing graphite target current used.

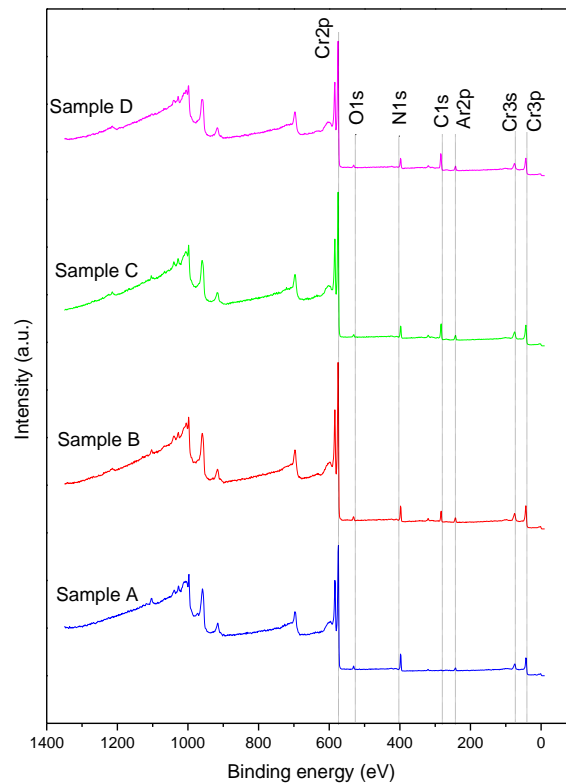


Figure 4.2: XPS survey etch spectra of the four Cr(C)N coatings with 120s surface clean

The peak positions, and their elemental concentrations, are summarized in Table 4.2 and Figure 4.3, respectively. To examine the elemental quantification in the coating, the Ar peaks observed in the survey scans were not included in this measurement. Table 4.2 includes data for both the C_{1s} A and C_{1s} B peaks.

Table 4.2: The peak positions and elemental concentrations in the four Cr(C)N coatings by survey scan with a 120s surface clean

	Binding Energy	A (0A)	B (1.5A)	C (3.5A)	D (4.5A)
	(eV)	(at. %)	(at. %)	(at. %)	(at. %)
C1s A	283.0	1.6	16.1	16.9	14.8
C1s B	284.5	6.3	9.6	18.0	24.2
Cr2p	575.0	57.5	50.9	46.8	45.2
N1s	398.4	24.5	17.1	14.2	12.2
O1s	531.8	10.1	6.4	4.2	3.6
Total C1s		7.9	25.7	34.9	39.0

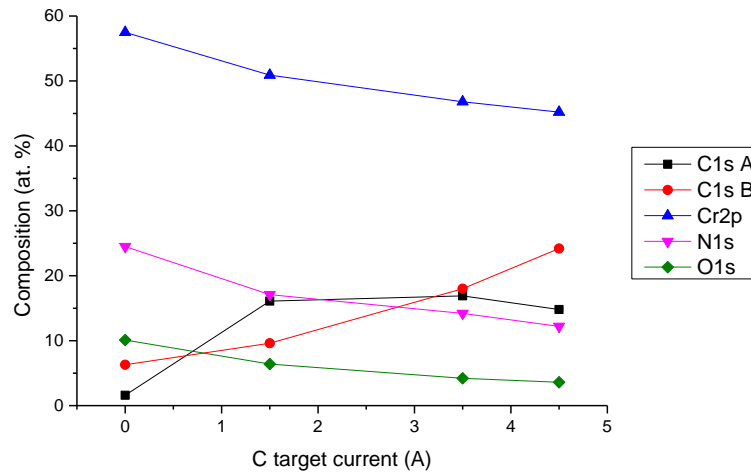


Figure 4.3: The elemental concentration of the Cr(C)N coatings as determined from a survey scan following a 120s surface clean

From Table 4.2 and Figure 4.3, a significant concentration of oxygen, in the range from 3.6 at. % (in specimen D) to 10.1 at. % (in specimen A), was detected, which was assumed to be associated with surface contamination. This was subsequently confirmed using an XPS depth profile analysis that is described later in this section.

In the XPS survey, the presence of Cr and N peak at binding energies of 575.0 eV and 398.4 eV, respectively, presumably derive from the Cr(C)N coating. The samples also show distinct carbon peaks consistent with the presence of both the C1s A and C1s B peaks at binding energies of 283.0 and 284.5 eV, respectively. This indicates the different carbon bonding types are present in each sample, which are discussed in detail

later. However, as shown in Table 4.2 and Figure 4.3, a small amount of carbon (1.6 at. %) was also detected in specimen A (with 0 A on the graphite target current). It was suspected that this carbon arises from the residual impurities on the specimen surface since the 120 seconds surface cleaning may have been insufficient to remove all contamination from the coating surface.

In order to confirm that the carbon content in specimen A was not present in the coating itself, but rather due to surface contamination a depth profile was performed. This allows examination of the relationship between the elemental concentration and depth to be explored and is shown in Figure 4.4. Generally speaking, the two distinct carbon peaks observed in the survey scans both increased in intensity with increasing graphite target current. However, the C1s A peak decreased in intensity for specimen D. Conversely, the chromium, nitrogen and oxygen concentrations all decreased relatively with increasing graphite target current. This implies the additional carbon in the coating occurred with increasing graphite target current occurred, as expected, in the Cr(C)N coatings.

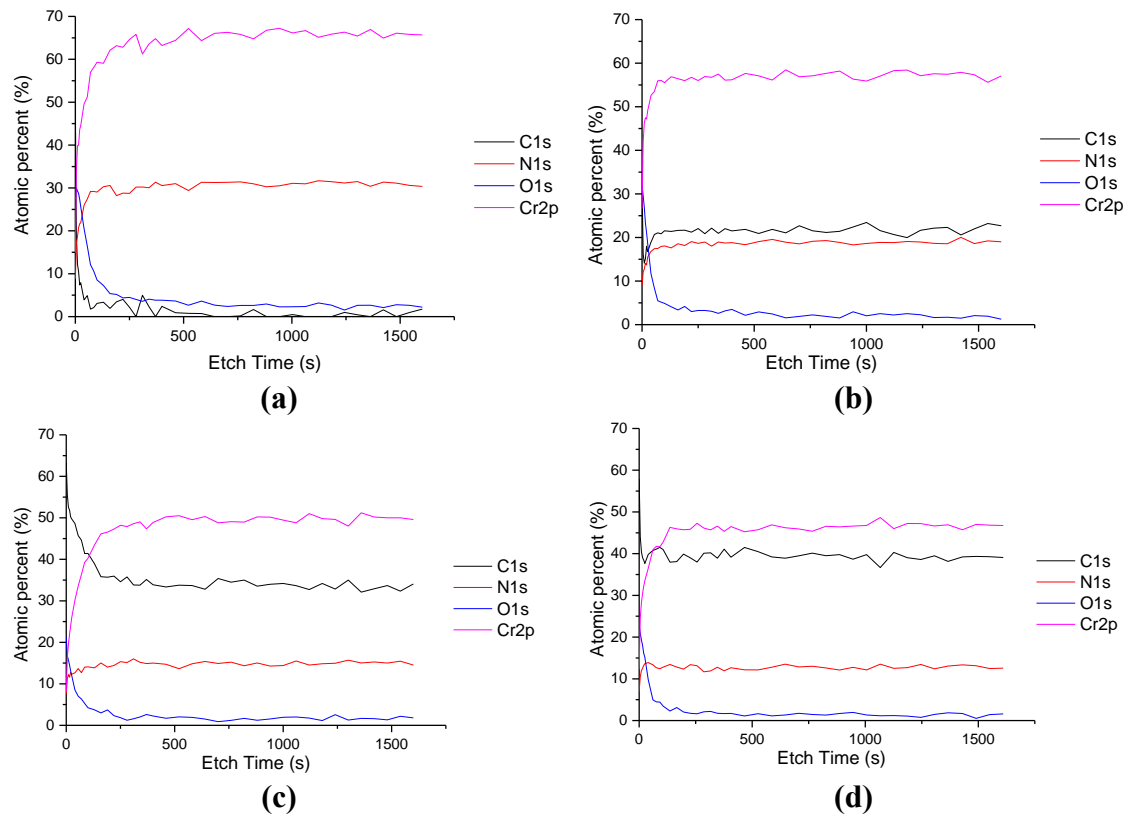


Figure 4.4: XPS depth-profile of Cr(C)N for the coatings (a) A (b) B (c) C (d) D

Figures 4.4 (a)-(d) show the atomic percentages of the constituent elements in the four coatings as a function of etching times for each sample. As etch time is increased, the effects of surface contamination were reduced and appeared to be negligible after about 240 s. As shown in Figure 4.4 (a), a considerable concentration of carbon was observed in specimen A (~15 at. %) at the beginning of the etching process, but this decreased to a constant value (less than 3 at. %) with increasing etch time. This confirms that the high carbon concentration obtained by the survey etch (for 120s) mostly derives from contamination on the specimen surface, rather than being present in the coating itself. These data also show that the amount of oxygen ranging from 20 at. % to 30 at. % present at the beginning of the etching process decreases to a small constant value in all four samples following etching. Therefore, the observed oxygen less than level of ~6 at. % (or lower) is believed to be intrinsically present in the film. It is clear that all elemental concentrations reach a constant value after an etch time of around 300 s. In order to determine a more accurate elemental concentration, the XPS survey scan after a 300 s surface clean were examined in further detail.

In Table 4.3, the peak position and elemental concentration of each peak examined after a 300 s surface clean is shown. A finite carbon concentration in specimen A of around 2.9 at % was determined which again implies that the larger amount of carbon (7.9 at. %) in specimen A, obtained by the survey etch following a 120s surface clean was mainly from residual impurities from surface contamination. More detailed analysis on the carbon present are provided in the discussion of the C1s fine spectra (Figure 4.5).

Table 4.3: The elemental concentration in Cr(C)N coatings by survey etch with a 300s surface clean

	BE	A (0A)	B (1.5A)	C (3.5A)	D (4.5A)
	(eV)	(at. %)	(at. %)	(at. %)	(at. %)
C1s A	283.0	0.9	18.0	18.1	16.1
C1s B	284.5	2.0	5.9	17.1	25.1
Cr2p	575.0	59.8	53.2	45.5	43.5
N1s	398.4	31.1	19.9	16.2	13.5
O1s	531.8	6.3	3.1	3.1	1.8
Total C		2.9	23.9	35.2	41.2
Cr/N		1.92	2.67	2.81	3.22
Cr/(C+N)		1.76	1.21	0.88	0.79

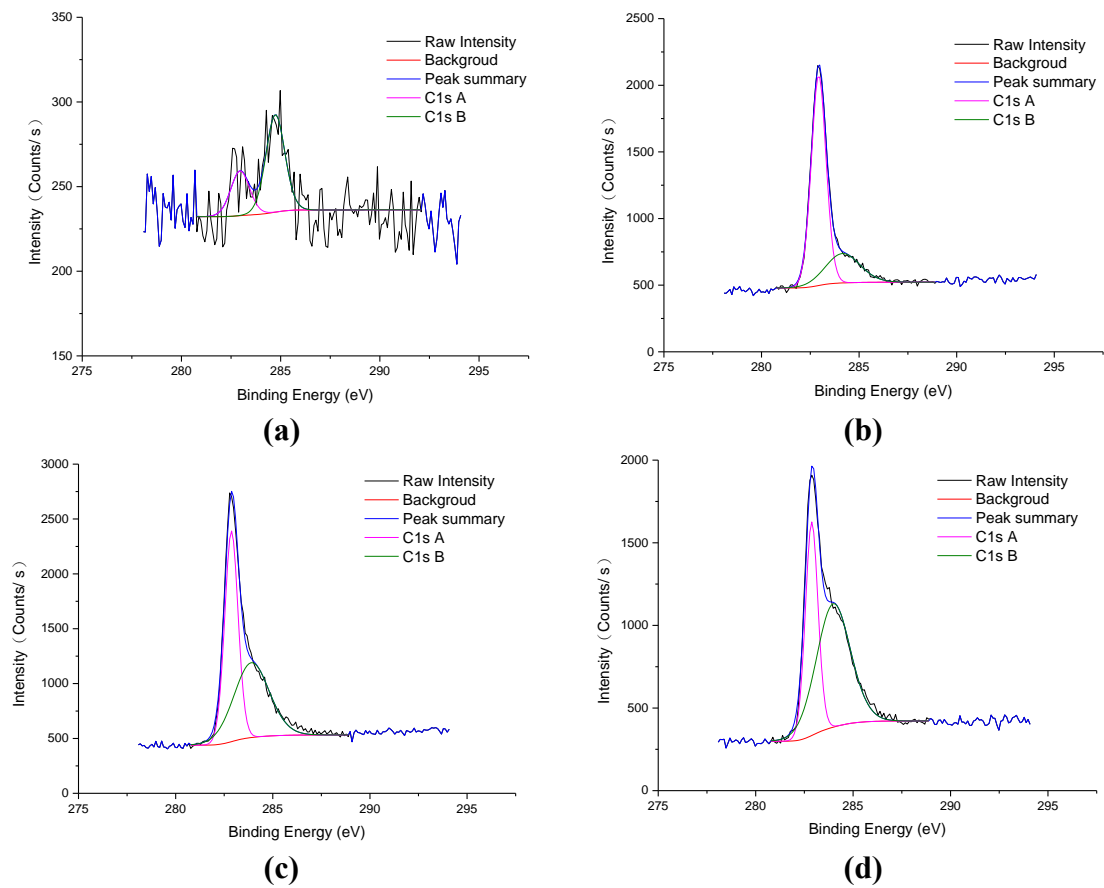


Figure 4.5: C1s fine spectra for specimens (a) A (b) B (c) C (d) D

The two carbon peaks at around 283 eV (C1s A) and 284.5 eV (C1s B) indicated the presence of both C-Cr and sp^2 C-C/C-N bonds [63], respectively. Both peaks increased in intensity with increasing graphite target current except that the C1s A peak that decreased in intensity for specimen D. Peaks at 286 eV and 288.1 eV, which are commonly related to the presence of sp^3 C-C/C-N and C=O, were not observed in this study [8, 63]. Wang et al. [63] pointed out that the presence of sp^3 C-C/C-N bonds in their coatings increased the hardness of their Cr(C)N coatings. In their study, carbon played an important role in the behaviour of these Cr(C)N coatings. Carbon present as sp^2 graphite-like bonding (C1s B) is more likely to act to reduce the coefficient of friction because it acts as a self-lubricant [8]. Carbon present as chromium carbide can lead to a reduction in hardness. This behaviour is described more detail in the section 4.3. The presence of chromium carbide might be confirmed by the Cr2p fine spectra shown in Figure 4.6. The chromium peak at around 575.0 eV could be associated with the presence of chromium nitride, chromium carbide or chromium oxide [63, 95, 96]. This observation might be supported by the broad FWHM of this peak in Figure 4.6.

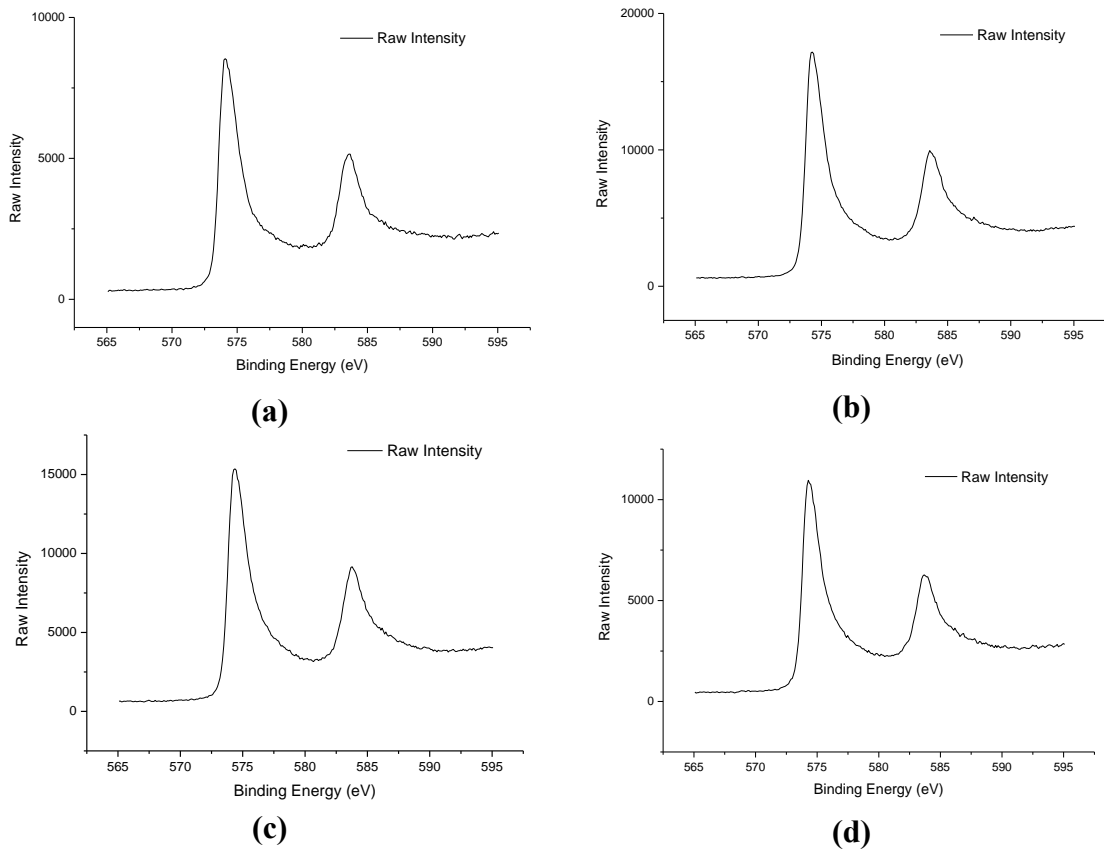


Figure 4.6: Cr2p fine spectra for specimens (a) A (b) B (c) C (d) D

Further, a finite amount of oxygen was detected in all coatings after a 300 s surface clean. This might be associated with Cr-O bonding. As shown in Table 4.3, the concentrations of Cr, N and O after a 300 s surface clean all decreased with increasing graphite target current.

In specimen A, the atomic ratio of Cr to N is ~ 1.92 . This is broadly consistent with the presence of Cr_2N . With increasing carbon concentration in the Cr(C)N coatings, the atomic ratio of Cr to N increased. This is presumably because the carbon atoms replace the nitrogen atoms in either the CrN or Cr_2N unit cells. As noted, the carbon content in specimens B, C and D is due to its presence in the coating, rather than as surface contamination that is the case for specimen A. Therefore, the atomic ratio of Cr to Cr+N was used to assess the phase stability (i.e. CrN or Cr_2N) for specimens B, C and D, rather than the atomic ratio of Cr to N. The atomic ratio of Cr to C+N for specimen B to specimen D then decreases from 1.21 to 0.79 and the carbon content increased from 2.9 at. % to 41.2 at. %, from specimen A to D indicating that Cr_2N is replaced by CrN with increasing carbon content. It is noted that the atomic ratio of Cr to N in CrN is theoretically unity, but the atomic ratio of Cr to C+N in specimens C and D is less than 1 (0.88 and 0.79, respectively). This might be due to the presence of amorphous carbon or chromium carbide in the Cr(C)N coatings. As discussed in the literature review (Figure 2.1), chromium nitride exists as a line phase which suggests that if excess carbon is present, then phases such as amorphous carbon or chromium carbide may be present between the CrN grains. Further work is required to investigate these possibilities in more detail.

4.2.3 X-ray Diffraction (XRD)

Figure 4.7 shows the XRD spectra show the all four Cr(C)N coatings with various graphite target currents for 2θ values ranging from 30 to 90°. The graphite target currents for specimens A, B, C and D were 0 A, 1.5 A, 3.5 A and 4.5 A, respectively. As shown in Figure 4.7, the Cr(C)N coatings exhibit the presence of both the fcc-structured CrN phase and the hcp-structured Cr₂N phase depending on the graphite target current. However, Cr₂N is dominant in specimen A, but, it is CrN that is the dominant phase in specimens B, C and D.

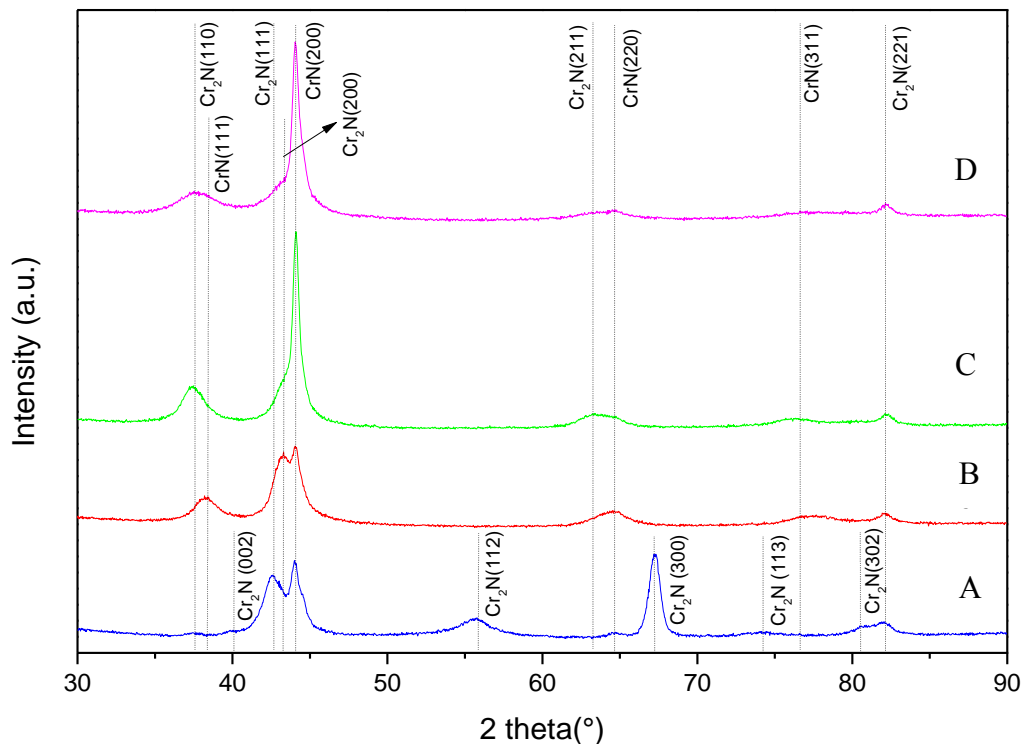


Fig. 4.7: X-ray diffraction spectra of the four Cr(C)N coatings

The diffraction peaks observed and shown in Figure 4.7 are consistent with those expected for either CrN or Cr₂N with reference to JCPDS pattern 01-076-2494 and JCPDS pattern 00-035-0803, respectively. No clear diffraction peaks relating to the presence of carbon e.g. graphite or chromium carbide were found in the diffraction patterns from these Cr(C)N coatings, even at the relatively higher concentration of carbon in the coatings prepared at high C target current (e.g. 39 at.% in specimen D). A similar effect was also observed by other authors [8, 59]. These workers suggested that

this effect, that is only CrN and Cr₂N were observed in the CrCN coatings, can be explained by two principal reasons. First, this may be associated with the relative low temperature during film growth. That is, a lower temperature favours the formation of a finer-grain structure, which may not be observed visibly in the X-ray measurements due to a low intensity of diffraction peak [35, 59]. Second, the carbon atoms might replace the nitrogen sites or form at interstitial positions in the CrN structure [17, 41]. Therefore, Cr(C_xN_{1-x}) or Cr₂(C_xN_{1-x}) solid solution might be formed due to the substitution of N by C in the Cr-N lattice.

As can be seen in the blue curve in Figure 4.7, specimen A shows several peaks that correlate well with the presence of Cr₂N, but fewer (and weaker) peaks (e.g. CrN (200) and CrN (220)) that are associated with the presence of CrN. This suggests that specimen A is predominantly Cr₂N. The blue curve also shows that specimen A exhibits a strong Cr₂N (300) orientation. This is consistent with the observation of Polcar [30].

When a small amount of carbon incorporated into the coating of specimen B, some of the Cr₂N peaks are no longer visible and a number of the CrN peaks are more intense (as shown in the red curve in Figure 4.7). Specifically, the peaks of Cr₂N (002), Cr₂N (112), Cr₂N (300), Cr₂N (113) and Cr₂N (302) are no longer visible and peaks from CrN (111) and CrN (311) are clearly apparent. Also, the dominant preferred orientation peak changes from Cr₂N (300) to CrN (200) with the incorporation of carbon. This indicates that the volume fraction of Cr₂N is reduced and the presence of C promotes the formation of CrN. In specimens B, C and D (red, green and pink curves, respectively), there is little difference over the 2θ range from 50-80°. However, at a $2\theta=42.6$, it can be clearly seen that the intensity of the Cr₂N (111) peak is decreased with increasing graphite target currents from 0 A to 4.5 A; conversely, the intensity of peaks CrN (200) at $2\theta=43.6$ is increased. This, again, implies the dominant phase changes from Cr₂N to CrN.

Generally, the observed diffraction peaks for Cr₂N are shifted towards lower angles compared to the standard data. This is presumably due to the presence of compressive stresses in the film [59]. Conversely, the diffraction peaks of CrN are shifted to higher angles compared to standard data due to tensile stresses caused by ion bombardment during deposition [35, 59, 97]. Values representing the residual tensile stresses and

compressive stresses in the fcc-CrN and hcp-Cr₂N phases indicated by $\Delta d = (d - d_0) / d_0$ (%) in Table 4.4, where d is the measured interplanar spacing (measured d-spacing) and d₀ is standard interplanar spacing (standard d-spacing). The nitrogen atoms are replaced by larger carbon atoms which reduce the lattice constant [41, 98].

The residual tensile stress and compressive stress are represented by negative and positive value of Δd , respectively. Other researchers reported that the intensity of diffraction peaks for CrN become lower and broadened through carbon doping to CrN, which was suggested to be associated with the presence of an amorphous structure, but this behaviour was not found in this study [99]. These workers suggested that the lowering of peak intensities and broadening peak is because that the carbon atoms cannot replace the nitrogen atoms, but rather the C atoms disturb the normal crystal structure of chromium nitride [8, 99]. However, it is suggested that in this study, C substitutes on to the N sites on the CrN lattice or the Cr₂N lattice.

Table 4.4 Inter-planar spacing (d-spacing) calculated using XRD results

		A		B		C		D	
plane	d ₀ (Å)	d (Å)	Δd (%)						
Cr₂N									
110	2.4057	2.4445	1.62	2.4100	0.18	2.4059	0.01	2.4161	0.43
002	1.2419	2.2574	0.69						
111	2.12	2.1271	0.33	2.1258	0.27	2.1262	0.29	2.1254	0.25
200	2.0832	2.0933	0.48	2.0987	0.75	2.0972	0.67	2.1050	1.05
112	1.6405	1.6538	0.81						
211	1.4862			1.4977	0.78	1.5167	2.05	1.4883	0.14
300	1.3892	1.3923	0.22						
113	1.2696	1.2770	0.58						
302	1.1808	1.1902	0.80						
221	1.1619	1.1738	1.2	1.1743	1.06	1.1731	0.97	1.1731	0.97
CrN									
111	2.3925			2.3489	-1.82	2.3508	-1.74	2.3712	-0.89
200	2.072	2.0530	-0.91	2.0529	-0.92	2.0532	-0.91	2.0530	-0.92
220	1.4651	1.4411	-1.63	1.4460	-1.30	1.4606	-0.30	1.4550	-0.69
311	1.2495			1.2315	-1.44	1.2464	-0.25	1.2288	-1.66

4.2.4 Transmission Electron Microscopy (TEM)

As can be seen in the Figure 4.8 (a)-(d), cross-sectional TEM bright-field images show several layers in each sample. A uniform columnar grain structure of the chromium wetting layer (around 50 nm in thickness) deposited on the M2 steel substrate for each sample, is clearly visible. This is consistent with the observations in the cross-sectional FIB images. A well-defined, closely packed columnar structure of CrN layer can be observed in specimen A (Figure 4.8 (a)). However, the columnar structure of Cr(C)N layer become finer and denser with increasing the graphite target current from 0 to 4.5A (Figure 4.8 (a) to (d)). This is possibly because the carbon atoms promote nucleation by acting as nucleation sites. It was suggested that these nucleation sites interrupt the normal crystal growth of CrN and limit grain growth leading to a finer structure [8]. Therefore, an increase in the nucleation rate relative to the growth rate results in a denser structure and grain refinement as the C content is increased.

From Figure 4.8 (a)-(d), all four samples show that the columnar grains of the Cr wetting layer extend into the Cr(C)N grains adjacent to this interface. Moreover, the columnar Cr(C)N grains adjacent to this interface appear relatively finer than the Cr(C)N grains closer to the coating outer surface. The appearance of single grains that span the Cr/Cr(C)N interface suggests that although there is a chemical change at this interface the Cr(C)N phase nucleates directly on to the Cr columnar grains . Ehiasarian [100] suggested that the coarser grain size closed to the coating outer surface is because higher growth rate grains dominate at this location.

From Figure 4.8 (e), irregular shaped voids can be clearly shown in specimen A (indicated by yellow arrows). With increasing the carbon target current in specimens C and D (Figure 4.8 (g) and (h)), those irregular shaped voids grow along with the columnar grain boundaries and form elongated and narrow inter-columnar voids (indicated by white arrows). This might suggest that the additional carbon atoms in the Cr(C)N coatings increase the columnar grain growth rate and elongated voids form at these boundaries.

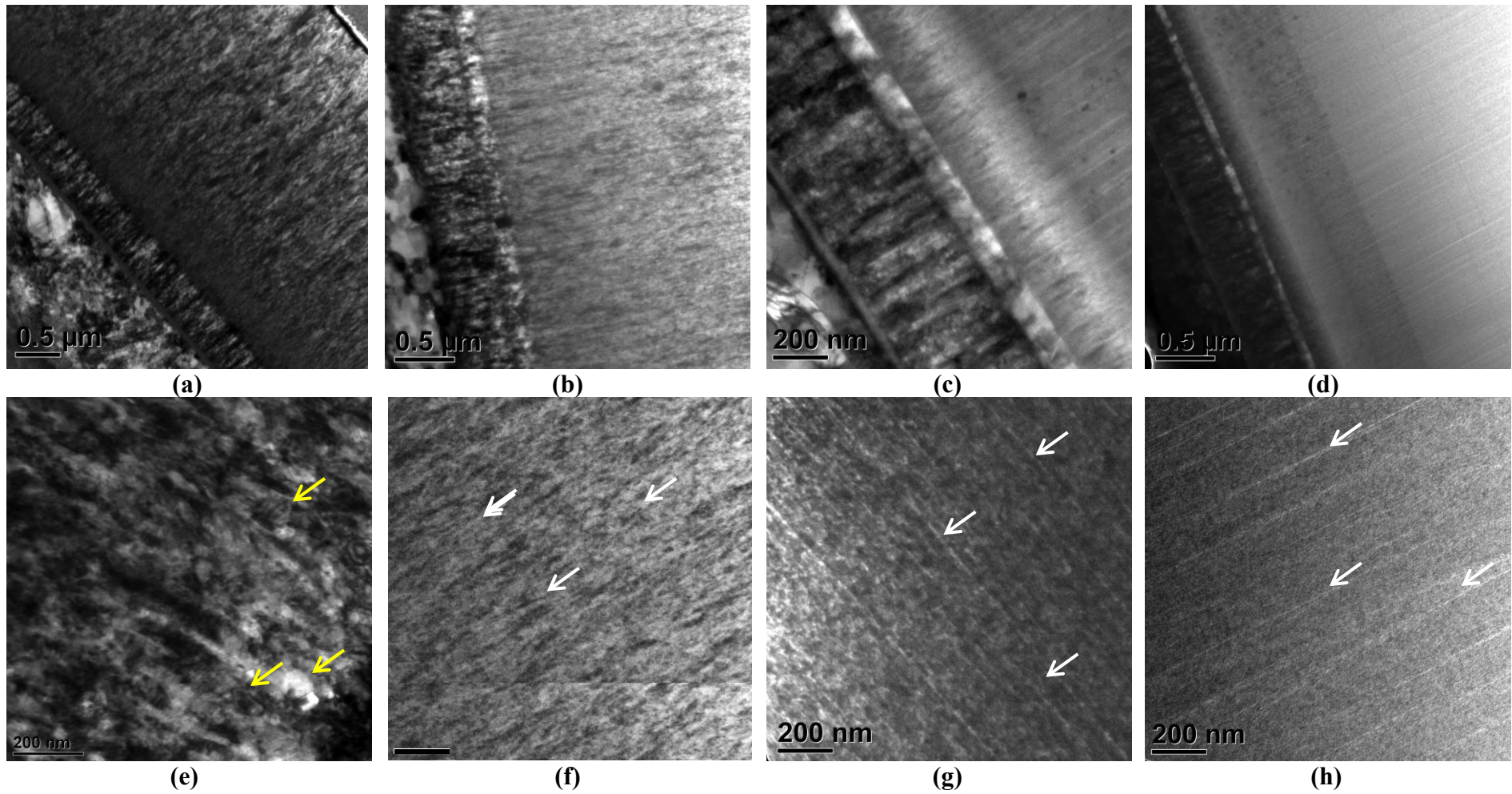


Figure 4.8: Bright-field TEM images of the Cr wetting layer (a)-(d) and Cr(C)N layer (e)-(f) for specimens A, B, C and D respectively

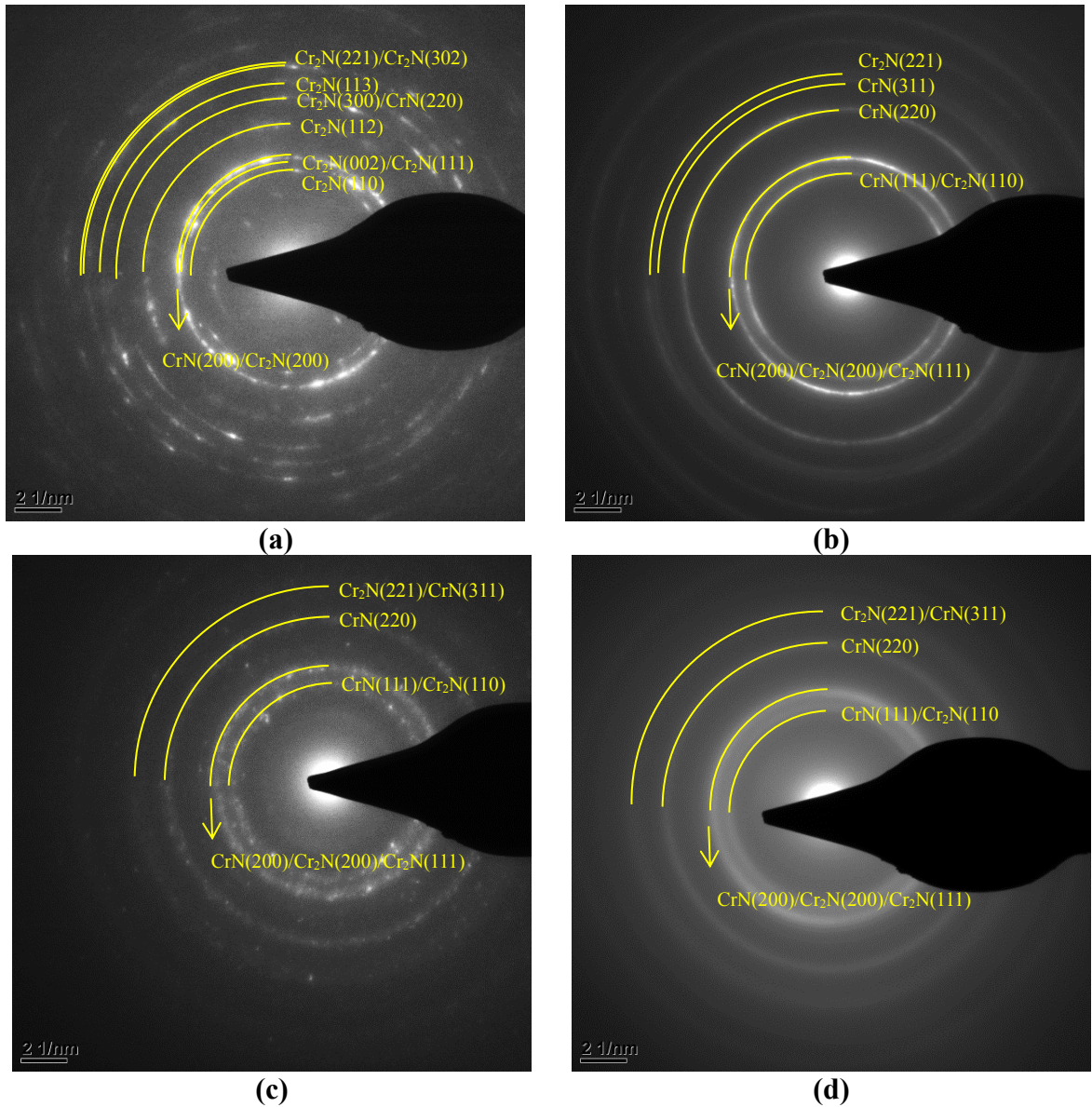


Figure 4.9: Selected area electron diffraction patterns from the Cr(C)N layers of (a) A (b) B (c) C (d) D

In Figure 4.9, the selected area electron diffraction (SAED) patterns for the four Cr(C)N coating are presented. For each analysis the diffraction aperture was located in the middle of the Cr(C)N layer. As shown in Figure 4.9 (a), the pattern for specimen A exhibits more rings which are more fragmented in nature compared to the other Cr(C)N coatings (Figure 4.9 (b)-(d).) When a small amount of carbon is present in the coating, for example specimen B, (Figure 4.9 (b)), the CrN (111) ring is clearly present, but some of Cr₂N rings are no longer clearly visible. This indicates that the dominant phase in this coating has transformed from Cr₂N to CrN. This is consistent with the XRD data described in Section 4.2.3. Compared to specimen A, the SAED pattern for specimen B exhibits less fragmented, but broader rings. Further, with more carbon present in

specimens C and D (Figure 4.9 (c) and (d)), the diffraction rings become wider and more diffuse. Some rings overlap and are not clearly resolved which results in broader, wider rings that inhibit analysis. These broader, more complete rings indicate the presence of a finer grain size in the more heavily carbon doped coatings suggesting a nanocrystalline structure. The planar indices for each ring were determined by calculating the inter-planar spacings (d) from the SAED patterns and then comparing the calculated, experimental values with the standard data (as described in section 4.2.3). The SAED patterns indicated that two crystalline phases, eg. FCC-CrN and HCP-Cr₂N, were present in all four coatings. The d-spacings calculated from the predominant rings and the corresponding planes for the reflections in the SAED patterns are summarized in the Table 4.5- Table 4.8.

Table 4.5: Inter-planar spacing (d-spacing) calculated using SAED for specimen A

	Ring radius (1/nm)	Measured d (Å)	Theoretical d ₀ (Å)	Phase
1	4.07-4.16	2.4022-2.4571	2.4057	Cr ₂ N(110)
2	4.24-4.42	2.2632-2.3562	2.2419	Cr ₂ N(002)
			2.1200	Cr ₂ N(111)
3	4.68-4.88	2.0476-2.15	2.0832	Cr ₂ N(200)
			2.0720	CrN(200)
4	5.87-6.1	1.6381-1.7030	1.6405	Cr ₂ N(112)
5	6.81-7.21	1.3871-1.4676	1.4651	CrN(220)
			1.3892	Cr ₂ N(300)
6	7.79-7.91	1.2647-1.2836	1.2696	Cr ₂ N(113)
7	8.43-8.49	1.1780-1.1862	1.1808	Cr ₂ N(302)
8	8.60-8.66	1.1543-1.1622	1.1619	Cr ₂ N(221)

Table 4.6: Inter-planar spacing (d-spacing) calculated using SAED for specimen B

	Ring radius (1/nm)	Measured d (Å)	Theoretical d ₀ (Å)	Phase
1	4.14-4.29	2.3333-2.4138	2.4057	Cr ₂ N (110)
			2.3925	CrN (111)
2	4.71-5	2-2.1212	2.1200	Cr ₂ N (111)
			2.0832	Cr ₂ N (200)
			2.0720	CrN (200)
3	6.79-7	1.4286-1.4737	1.4651	CrN (220)
4	7.86-8.29	1.2069-1.2727	1.2495	CrN (311)
5	8.29-8.64	1.1570-1.2069	1.1619	Cr ₂ N (221)

Table 4.7: Inter-planar spacing (d-spacing) calculated using SAED for specimen C

	Ring radius (1/nm)	Measured d (Å)	Theoretical d ₀ (Å)	Phase
1	4-4.22	2.3674-2.5	2.4057	Cr ₂ N(110)
			2.3925	CrN(111)
2	4.71-5	2-2.1226	2.1200	Cr ₂ N(111)
			2.0832	Cr ₂ N(200)
			2.0720	CrN(200)
3	6.78-7	1.4285-1.4754	1.4651	CrN(220)
4	8-8.61	1.1619-1.25	1.2495	CrN(311)
			1.1619	Cr ₂ N(221)

Table 4.8: Inter-planar spacing (d-spacing) calculated using SAED for specimen D

	Ring radius (1/nm)	Measured d (Å)	Theoretical d ₀ (Å)	Phase
1	4.11-4.44	2.25-2.4342	2.4057	Cr ₂ N(110)
			2.3925	CrN(111)
2	4.72-5.09	1.9627-2.1206	2.1200	Cr ₂ N(111)
			2.0832	Cr ₂ N(200)
			2.0720	CrN(200)
3	6.78-7.05	1.4192-1.476	1.4651	CrN(220)
4	8-8.61	1.1616-1.25	1.2495	CrN(311)
			1.1619	Cr ₂ N(221)

The phases determined to be present from the SAED patterns are generally consistent with the analysis from the XRD spectra (Figure 4.7). However, the peak from Cr₂N (211) was not observed in the SAED pattern. This might be because the intensity of this ring was too low and not readily visible in the SAED pattern. As can be seen from the Table 4.5- Table 4.8, the measured d-spacings have a small range of values for each ring due to their finite ring width. This might also suggest that some planes overlap resulting in an overall wider ring. The presence of brighter rings in the diffraction patterns implies higher volume fraction for that phase (if structure factor effects are ignored) which is consistent with the XRD data.

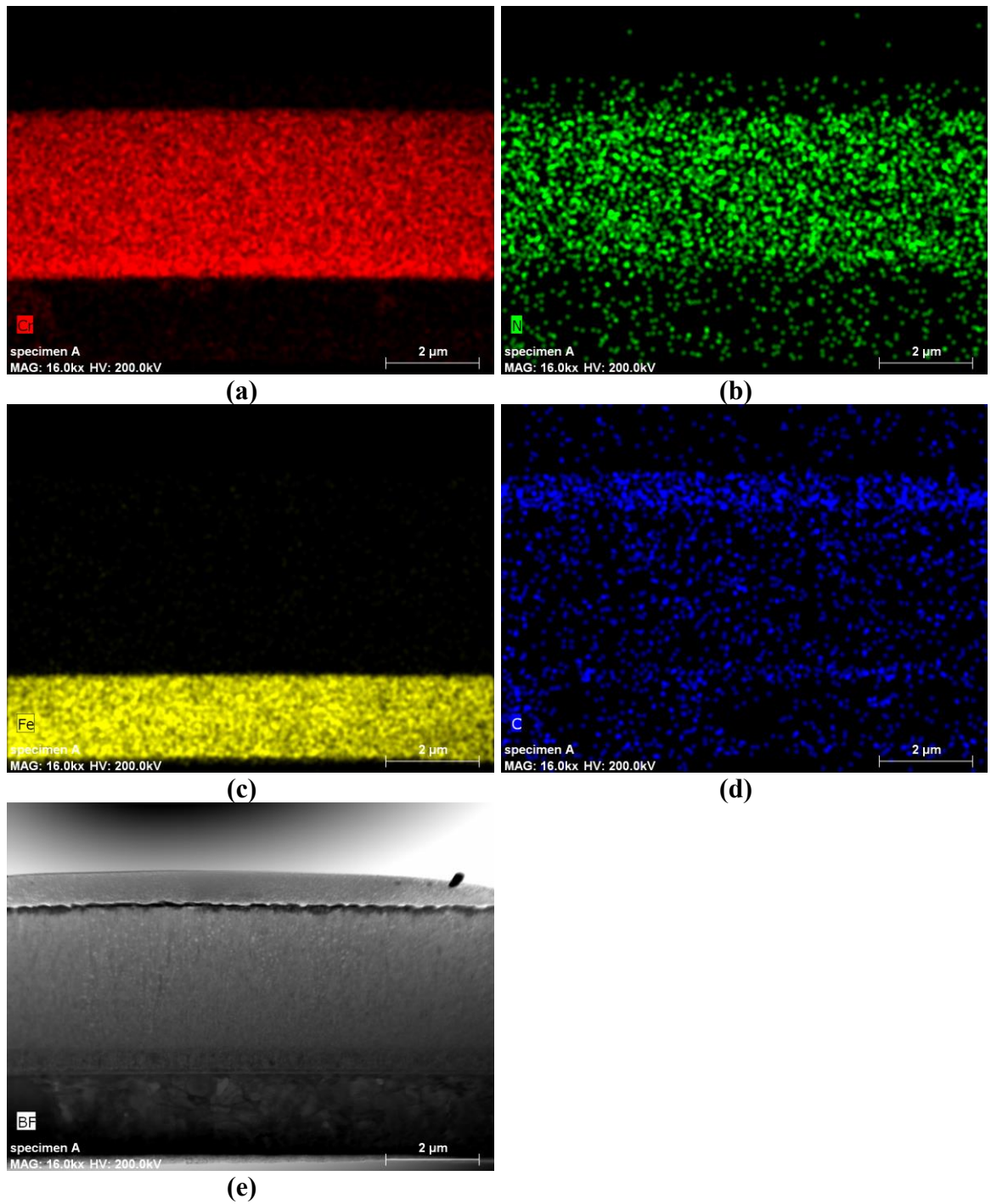


Figure 4.10: EDS elemental maps for Specimen A (a) Cr (b) N (c) Fe (d) C (e) bright field STEM image

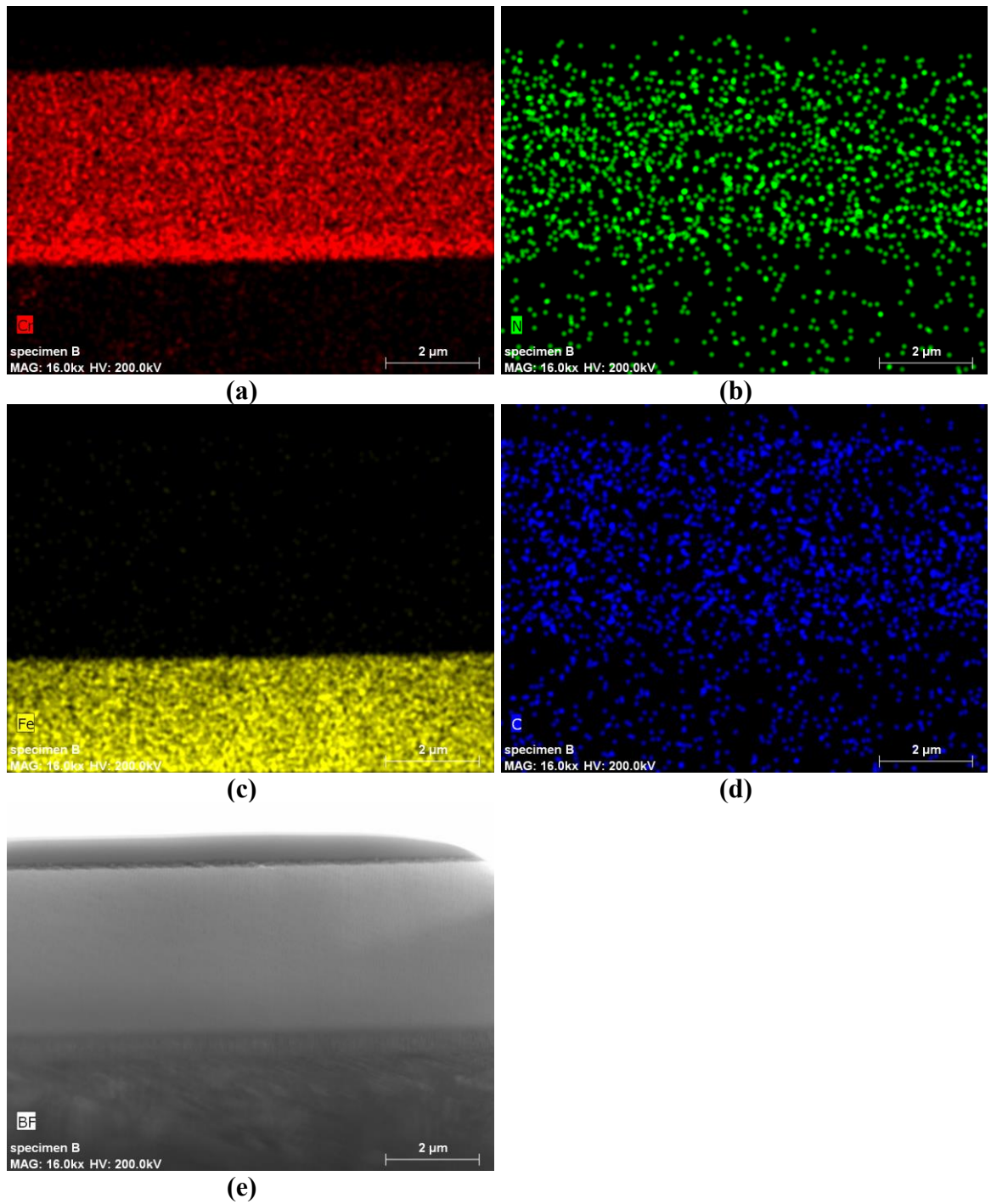


Figure 4.11: EDS elemental maps for Specimen B (a) Cr (b) N (c) Fe (d) C (e) bright field STEM image

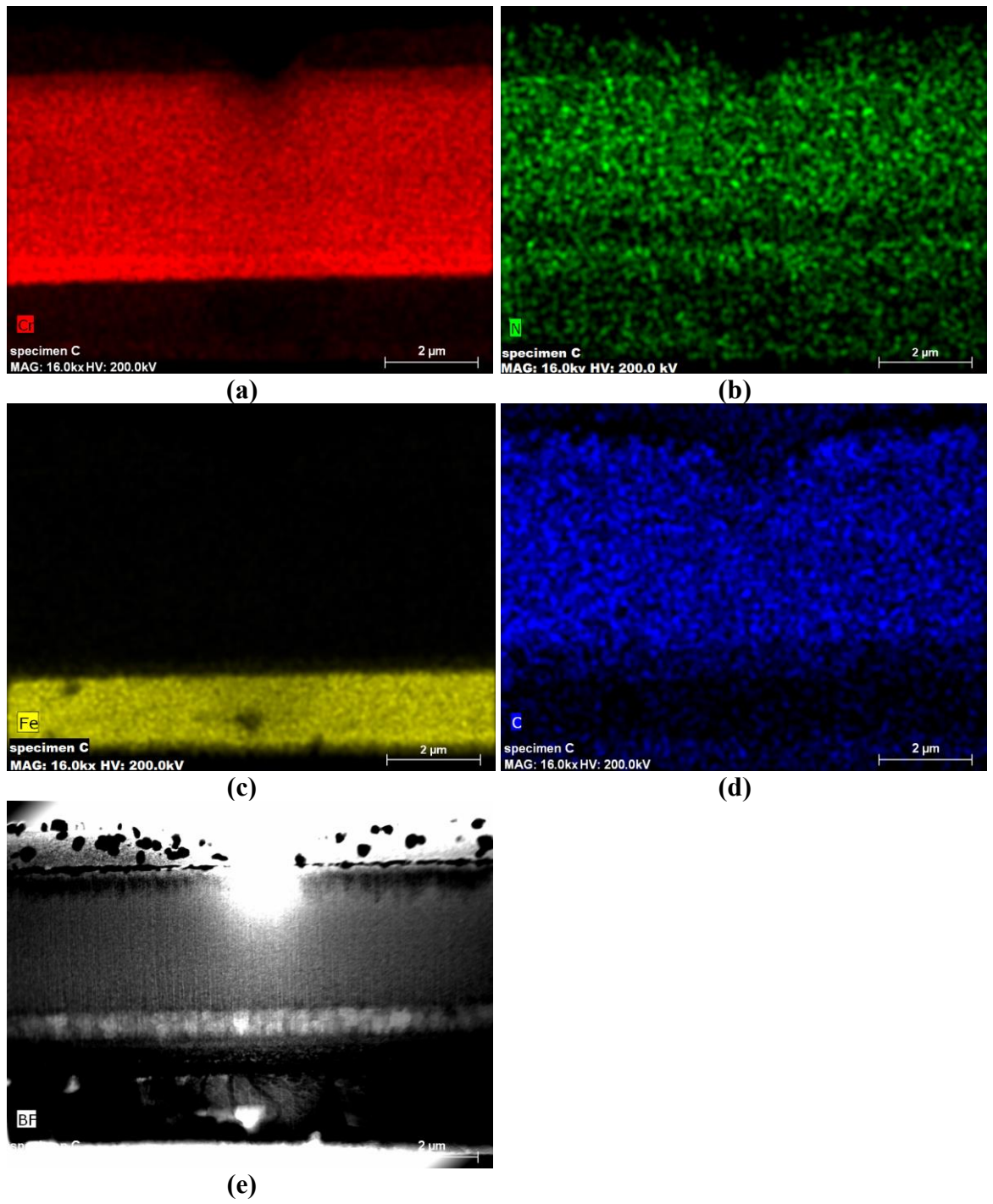


Figure 4.12: EDS elemental maps for Specimen C (a) Cr (b) N (c) Fe (d) C (e) bright field STEM image

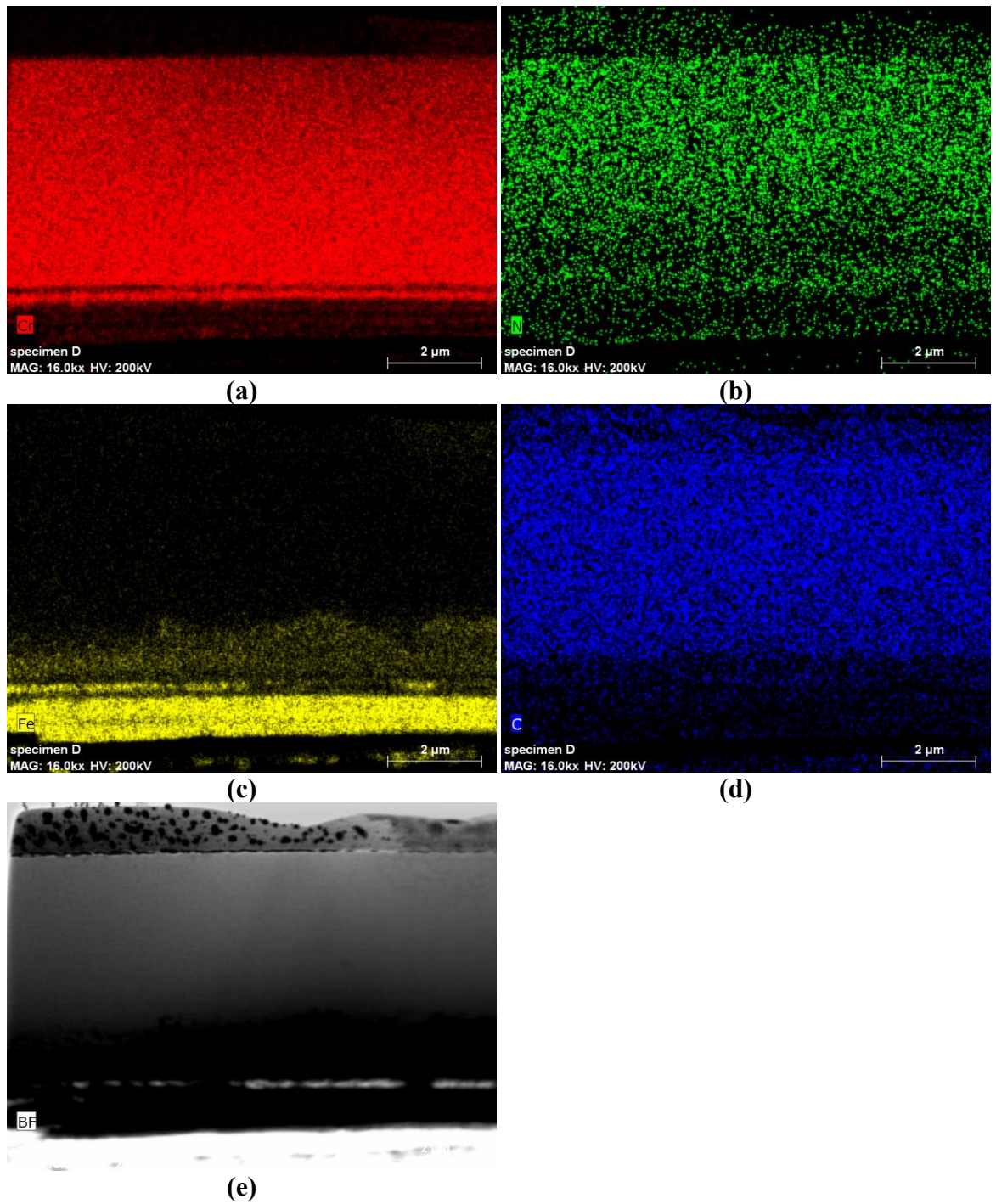


Figure 4.13: EDS elemental maps for Specimen D (a) Cr (b) N (c) Fe (d) C (e) bright field STEM image

Compositional data obtained from energy dispersive X-ray spectroscopy (EDS) elemental mapping of the regions containing the Cr(C)N coatings, Cr wetting layer and M2 steel substrate are shown in Figures 4.10-4.13. The different elements are represented by different colours. The mapping images show the elemental distribution for chromium (red), nitrogen (green), iron (yellow) and carbon (blue). From these images, the overall chemical composition of the samples can be readily identified. However, more subtle differences in the concentration of each sample are less clear. The effects of higher carbon concentrations in the Cr(C)N coatings are apparent through the more intense blue colouring of the C maps, but due to the relatively low efficiency of collection and production of C K X-rays in EDS more quantitative assessment of C concentrations in these films cannot be assessed.

4.2.5 Atomic Force Microscopy (AFM)

AFM scanasyst mode images of the Cr(C)N coatings show that the surface grains are cobblestone-like in Figure 4.14 (a)-(d). As shown in Figure 4.15, the TEM cross-sectional image, in this case of specimen B, shows that the interface between protective platinum layer and Cr(C)N layer is not smooth, but varies slightly in topography. This manifests the appearance of the surface of the cross-sectional columnar structure as a cobblestone-like surface. The finer columnar grains, such as those in specimens C and D, lead to a smaller roughness and smaller feature size than specimens A and B.

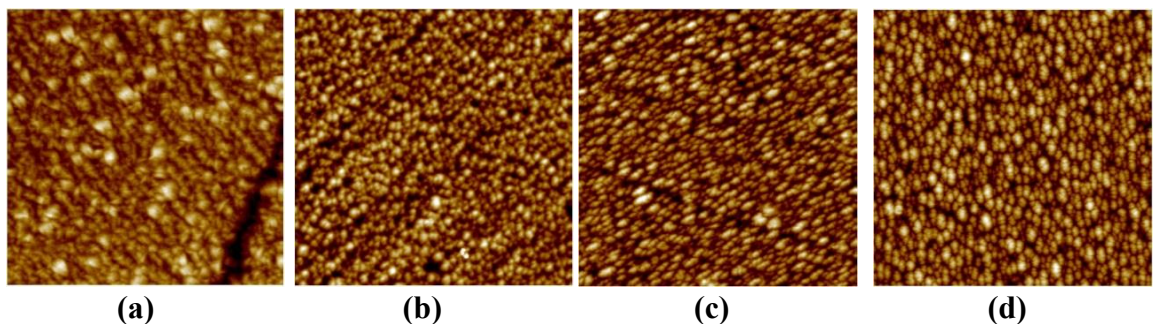


Figure 4.14: AFM images with scanasyst mode in $5\mu\text{m} \times 5\mu\text{m}$ area for the Cr(C)N coatings
(a) A (b) B (c) C (d) D

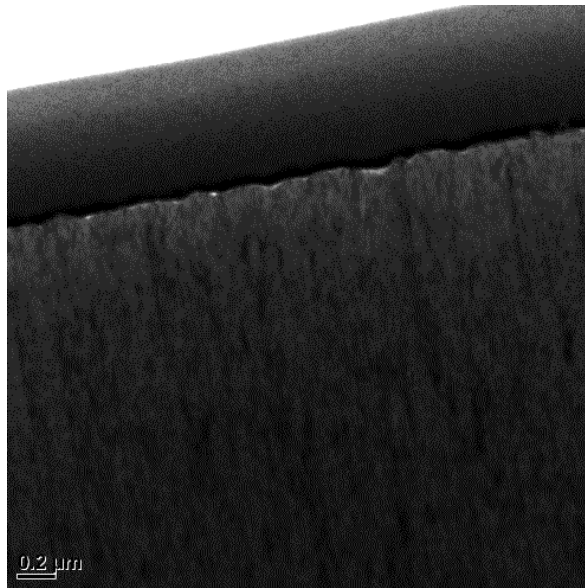


Figure 4.15: TEM bright field image of specimen B

The particle size was analysed from the cross-sectional surface using the section function of the AFM software (More information about this function is described in the literature and section 3.3.3.) In general, the surface roughness and the particle size decreases with the increasing carbon content in the coatings (See Table 4.9). The higher roughness corresponds to the growth of the coarser columnar structure. The carbon atoms promote nucleation leading to a finer grain size [8]. A similar effect was observed by others authors [8, 41]. Thus, with increasing graphite target current, the surface roughness became smaller.

Table 4.9: Roughness (Ra)* and feature size* for the four Cr(C)N coatings

	A	B	C	D
Roughness, Ra (nm)	10.7	9.51	7.58	8.19
Feature size (μm)	0.34	0.24	0.22	0.21

* Ra= Arithmetic average roughness

*Feature size= The average diameter of the particle size

4.3 Mechanical and tribological properties characterization

4.3.1 Mechanical properties

The hardness, H , and elastic modulus, E , values for the Cr(C)N coatings were measured using Hysitron triboindentation. The H and E values were then used to calculate the elastic strain resistance (or elastic index, H/E) and plastic deformation resistance (or plastic index, H^3/E^2) [63]. A material with a higher value of E allows the given load to be distributed over a smaller volume in the material [101]. A higher value of H/E indicates that a material has higher resistant against elastic strain to failure. A higher value of H^3/E^2 indicates that the material is highly resistant to plastic deformation [102, 103].

According to Johnson's analysis [104], the yield pressure P_y in a rigid-ball on elastic/plastic plate contact can be determined by the equation:

$$P_y = 0.78r^2 (H^3/E^2)$$

where r is the contacting sphere radius. Thus, the value of H^3/E^2 is proportional to the load at which the material starts to deform plastically. In addition, the value of H/E and H^3/E^2 are two important parameters to assist in the understanding of tribological behaviour and wear resistance which are discussed in detail in section 4.3.2.

Both hardness and modulus show a similar tendency with respect to increasing carbon content as shown in both Table 4.10 and Figure 4.16. In general, both hardness and modulus decrease with increasing carbon target current. Both parameters exhibit the highest values for both H and E for 0 A applied to the graphite target (specimen A) (19.4 GPa and 295 GPa) and the lowest values for the 4.5 A graphite target current (specimen D) (14.9 GPa and 218.6 GPa). For 1.5 A and 3.5 A graphite target current, (specimens B and C) both parameters exhibit the third highest (16 GPa and 235.4 GPa) and second highest value (17.3 GPa and 146.9 GPa) for both H and E , respectively. This suggests that although it is clear that E and H decrease with carbon content, the variation is more complex than based simply on increasing C concentration in the coating.

Table 4.10: Summary of values of H, E, H/E and H^3/E^2 for the four Cr(C)N coatings.

		Modulus, E (GPa)	Hardness, H (GPa)	H/E	H^3/E^2 (GPa)
A398	Mean	295.0	19.4	0.0657	0.0838
	Std Dev	18.3	1.5		
B387	Mean	235.4	16.0	0.0681	0.0744
	Std Dev	16.7	1.2		
C393	Mean	246.9	17.3	0.0699	0.0843
	Std Dev	8.1	1.1		
D396	Mean	218.6	14.9	0.0680	0.0688
	Std Dev	8.1	0.8		

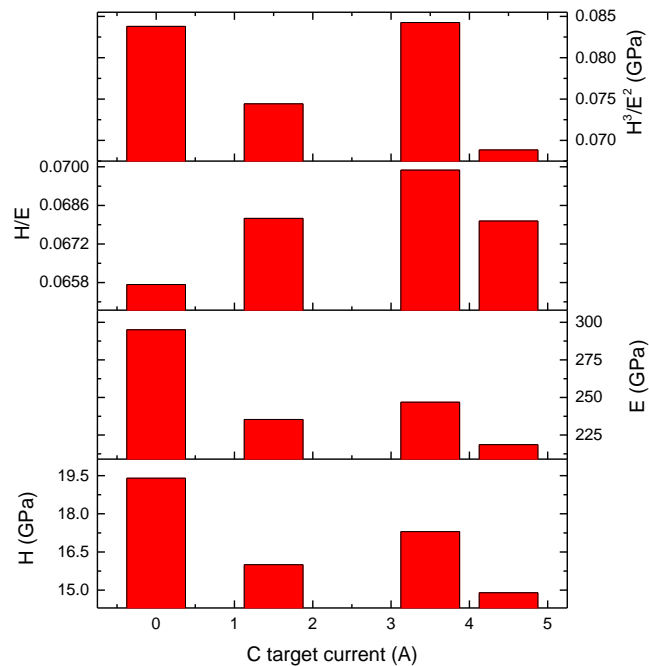


Figure 4.16: Histograms showing the values of H, E, H/E and H^3/E^2 for different C target currents

The total indentation depth for an applied load of 8mN is less than 3% of the coating thickness (Table 4.11). Thus, this suggests that the substrate did not contribute to the deformation during testing due to the 10 percent rule [85, 105]. The 10 percent rule is not based on modelling constraints, but rather derived from empirical evidence.

Table 4.11: Ratio of indentation depth to total thickness of Cr(C)N coatings using a 8mN of load

	Thickness (μm)	Indentation depth (nm)	Ratio (%)
A	4.10	125.0	3.04
B	5.75	140.2	2.44
C	6.08	135.1	2.22
D	6.95	146.0	2.10

Furthermore, an increase in hardness with increased carbon content reported by other authors [8, 99] was not observed in this study. These workers suggested that the hardness increases with increasing carbon content due to solid solution hardening and increased sp^3 bonding. However, an increase in sp^3 bonding was not observed in the XPS data derived from this current study (Table 4.3). However, a similar effect, that is decreasing hardness with increasing C carbon content, was also observed by some other authors [30, 35, 36, 41, 63]. These authors attributed this decrease in hardness to two causes: firstly, the higher amorphous carbon content in the carbon-rich coatings, and secondly, a lower percentage of sp^3 bonding in the coatings. As shown in Table 4.3, much of the carbon in the coatings studied here formed as sp^2 bonding, exhibited in the XPS spectra by the peak at a binding energy of 284.5 eV. Moreover, the sp^2 content increased with carbon target current. Therefore, the hardness of the coating decreased, broadly, with increasing graphite target current.

As shown in Table 4.3, it is worth noting that the analysis by XPS shows that the carbon content in specimen C is higher than specimen B, but the hardness in specimen B is lower than specimen C. XPS analysis indicates that in both specimens B and C there is around 18% of Cr-C bonding (signified by the peak at a binding energy of ~ 283 eV (C1sA)).

However, there is a much higher percentage of C associated with sp^2 -C-C/C-N bonds for specimen C compared to specimen B. Moreover, there is higher concentration of these bonds in specimen D, which exhibits the lowest overall hardness. This would suggest that these sp^2 -C-C/C-N bonds reduce hardness. As referred to in section 4.2.4, the cross-sectional TEM images of Cr(C)N showed that the course columnar structure of the coatings became denser and finer with increasing carbon content since the space

between the columnar grains is decreased. Further, as referred to section 4.2.5, the feature size of the Cr(C)N phase examined using AFM, changed from 0.34, 0.24, 0.22 to 0.21 μm with increasing C content. The feature size measured in this study is lateral columnar size which is correlated to the grain size. Therefore, it is clear that C additions reduce the CrN grain size, which may then lead to greater Hall-Petch type strengthening effects in the specimens with a finer grain size [106, 107]. Although at these very fine grain size, the large fraction of atoms located in grain boundaries may also lead to Hall-Petch softening effects [107-109].

These phenomena might also be explained by the present of Cr-C bonds. The presence of Cr-C bonding was detected by XPS. (Although the presence of chromium carbide based phases that exhibit this type of bonding was not detected by either TEM electron diffraction or XRD analysis). This may relate to the presence of an amorphous chromium carbide phase which may lead to a decrease in hardness for these coatings [61]. An increase in hardness for specimen C may be due to the solid solution hardening by carbon (35.2 at. % in this study). The carbon atoms replace the nitrogen sites and then these migrating nitrogen atoms may form an amorphous carbon nitride (a-CN_x) phase at the boundary [110]. In fact, it is known that nitride films of transition metals can admit only a limited number of atoms into interstitial positions [111]. The carbon atoms incorporated into the lattice interstitially strengthen the structure of the CrN unit cell. Once the carbon is over this solubility limit, some carbon atoms might segregate to the grain boundaries and thus decrease the hardness. Therefore, the further decreasing hardness in specimen D is suggested to be due to an increase in the volume fraction of amorphous carbon (41.2 at. % in this study) [41, 63, 112]. It is also known that Cr₂N is harder than CrN, therefore as the C additions promote the formation of CrN, relative to Cr₂N, some softening would also be expected. It is clear that there are several competing effects which determine the overall hardness of a given coating. In these coatings the individual effects of each factor cannot be readily separated to determine clearly their unambiguous influence on hardness. This would be the subject of further work.

As shown in Table 10, the H/E and H^3/E^2 values obtained here are lower than those obtained in previous studies: 0.08-0.10 for H/E and 0.08-0.19 for H^3/E^2 [30, 41, 113]. This is presumably due to the relatively low hardness observed in this study (In previous studies, the hardness of the Cr(C)N coatings ranged from 19 to 29 GPa). Generally, a material with highly resistance to plastic deformation (H^3/E^2) has higher elastic strain resistance (H/E) [114]. In other studies, a material with a high hardness and low elastic modulus allows the applied load to be dissipated over a larger area [101, 114]. It is worth noting that specimen A shows a higher H^3/E^2 , but a lower H/E ; whilst specimen D shows a lower H^3/E^2 , but higher H/E compared to the other samples. This can be explained by Figure 4.17. In this figure, specimen A shows the highest resistance to plastic deformation (lowest total depth) due to the high H^3/E^2 (0.0838) and specimen D shows the lowest resistance to plastic deformation (highest total depth) due to the low H^3/E^2 value (0.0688). From the unloading curve, specimen A show the lowest elastic recovery due to its low H/E and specimen D show the highest elastic recovery due to its high H/E value. Specimen A had the lowest H/E value around 0.065 indicating poorer elastic strain resistance; while specimen C exhibited the maximum H/E value of 0.07 indicating good elastic strain resistance. Specimen A and C have the highest H^3/E^2 around 0.084 indicating good plastic deformation resistance.

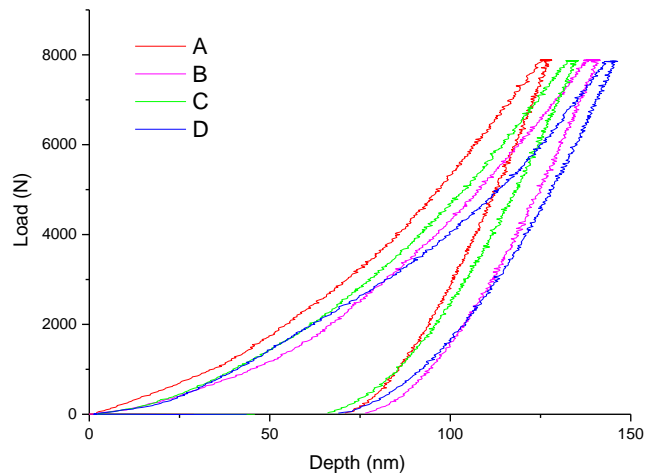


Figure 4.17: Depth vs. Load under 8mN using Hysitron indentation

4.3.2 Tribological properties

The coefficients of friction of the Cr(C)N coatings were measured using a pin-on-disk wear testing. The coefficients of friction, as function of sliding distance, of the four Cr(C)N coatings sliding against ruby balls are illustrated in Figure 4.18. As can be seen, higher carbon concentrations in the CrN coatings do not lead to a significant decrease in coefficient of friction. For all four coatings the measured values of coefficient of friction fell in a range from 0.4 to 0.46 which is similar to values for coefficient of friction measured by other researchers [35]. That is, Warcholinski measured that coefficient of friction for CrN was 0.54 and that carbon additions to CrN led to values in the range from 0.4 to 0.5. It was suggested that decreasing coefficient of friction might be related to the Cr-C system which has a coefficient of friction of 0.33 [35]. The average coefficients of friction were measured after the initial run-in period because that the initial roughness of the coating surfaces might affect the run-in period for obtaining accurate values. The larger initial roughness need longer time for smoothing the surface asperities. The measured coefficient of friction values after different run-in periods is shown in Figure 4.19. The error bars shown in Figure 4.19 are the standard deviations from all fluctuations after the various run-in periods for each sample.

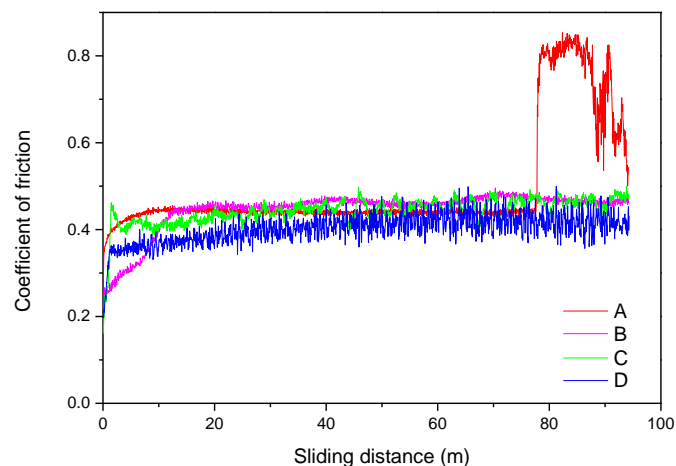


Figure 4.18: Friction behaviour of Cr(C)N coatings sliding against ruby balls

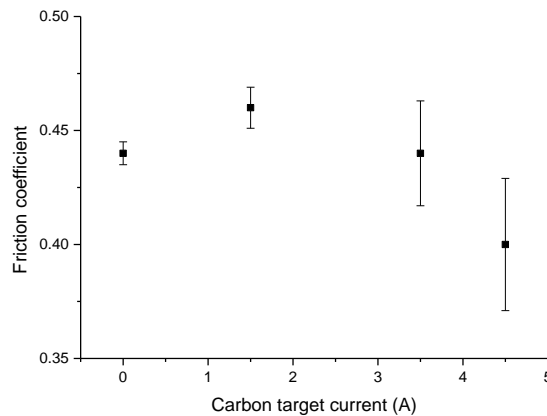


Figure 4.19: Coefficient of friction as a function of carbon target current

The overall shape of the curves is similar although the run-in periods and the friction values are slightly different. For specimen A ($I_C=0$), the coefficient of friction increased following the run-in period from initial value of just less than 0.4 to a steady value of 0.44 (± 0.005) at a sliding distance of 10 m and then sharply rose to a value to 0.8 at around 80 m. This might be because the wear track reached the M2 steel substrate. This are confirmed later through observation of cross-sectional images shown in section 4.4.2. The coefficient of friction for binary CrN was relatively lower than the values recorded in previous studies ($\sim 0.5-0.7$), but for the ternary Cr(C)N coatings, the values were similar to those reported elsewhere [8, 35]. This difference may be due to the different phase compositions of the coatings studied here compared to these other materials [97]. Qianzhi [63] suggested that the differences in the coefficient of friction were associated with the presence of Cr_2O_3 particles in the coatings they examined. Other workers [115, 116] also reported that the presence of chromium oxides build additional protective film on the worn surface and decrease the coefficient of frictions. As referred to in the XPS data (Table 4.3), the relatively low coefficient of friction of CrN in this study could possibly be explained by presence of chromium oxide (6.3 at.% for O1s) in these coatings.

For specimen B ($I_C=1.5$ A), the coefficient of friction increased gradually to a steady value of 0.46 (± 0.009) at a sliding distance of 15 m and then maintained the same value with only a slight variation. For sample C ($I_C=3.5$ A), the coefficient of friction increased sharply from initial value following the run-in period. The average coefficient of friction of specimen C measured after the run-in period at 3m is 0.44 (± 0.023). For specimen D ($I_C=4.5$ A), the shape of curve is very similar to specimen C. The coefficient of friction of specimen D increased continuously from a sliding distance of 1.5 m to the end of the test.

During sliding, the ruby ball plowed into the Cr(C)N coatings and created wear particles which may influence frictional behaviour. As can be seen in the curves for specimens C and D, increasing the sliding distance resulted in increasing the value for the coefficient of friction. Moreover, the degree of noise increases with sliding distance as well. The average coefficient of friction of sample D measured after the run-in period at 1.5 m was 0.40 (± 0.029).

Generally, an increase in carbon content in the coatings leads to a slightly lower coefficient of friction. This can be explained by the presence of sp^2 carbon bonding and also, possibly, chromium carbide in these coatings (Table 4.3). The high hardness and relatively low ductility of specimen A lead to significant cracking of this coating during wear testing and its almost complete removal from the wear track. It is evident that although carbon additions did not greatly reduce the coefficient of friction they did increase coating toughness to prevent cracking and coating spallation.

4.4 Deformation and fracture behaviour

4.4.1 Ultra Micro-Indentation System (UMIS)

The indentation responses of all Cr(C)N coatings, examined in a range of loads from 100 mN to 500 mN using a 5 μ m radius spherical indenter, are shown in Table 4.12 to Table 4.15 and in Figure 4.20. In general, as expected, the total depth, the residual depth as well as the degree of recovery increased with increasing indentation load for each specimen. However, the percentage of recovery decreased with increasing load.

Table 4.12: UMIS data for Specimen A

Indentation Load (mN)	100	200	300	400	500
Total Depth, ht (μm)	0.37	0.62	0.90	1.22	1.50
Residual Depth, hr (μm)	0.11	0.24	0.44	0.68	0.93
Recovery, he (μm)	0.26	0.37	0.45	0.54	0.57
Recovery %	0.69	0.60	0.51	0.44	0.38

Table 4.13: UMIS data for Specimen B

Indentation Load (mN)	100	200	300	400	500
Total Depth, ht (μm)	0.41	0.71	1.02	1.40	1.79
Residual Depth, hr (μm)	0.13	0.26	0.40	0.59	0.88
Recovery, he (μm)	0.28	0.45	0.63	0.80	0.91
Recovery %	0.69	0.63	0.61	0.57	0.51

Table 4.14: UMIS data for Specimen C

Indentation Load (mN)	100	200	300	400	500
Total Depth, ht (μm)	0.37	0.63	0.86	1.13	1.43
Residual Depth, hr (μm)	0.09	0.21	0.34	0.53	0.79
Recovery, he (μm)	0.28	0.41	0.52	0.60	0.63
Recovery %	0.76	0.66	0.61	0.53	0.44

Table 4.15: UMIS data for Specimen D

Indentation Load (mN)	100	200	300	400	500
Total Depth, ht (μm)	0.40	0.67	0.91	1.21	1.48
Residual Depth, hr (μm)	0.12	0.25	0.38	0.58	0.83
Recovery, he (μm)	0.28	0.42	0.53	0.63	0.66
Recovery %	0.71	0.63	0.58	0.52	0.44

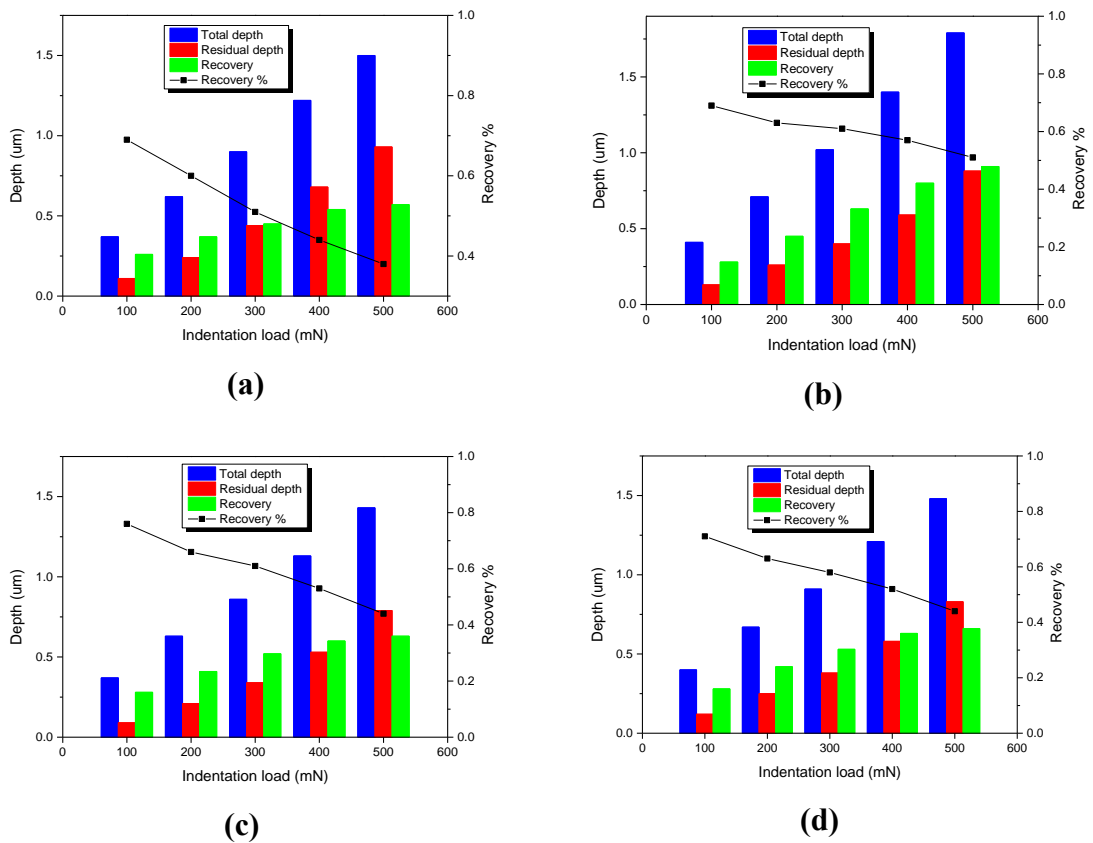


Figure 4.20: Deformation behaviour at loads 100-500mN for specimens (a) A (b) B (c) C (d) D

As can be seen from Table 4.16, the total indentation depths for specimen B were the highest across all loads amongst the four samples. This might suggest that specimen B has the lowest hardness. However, as described in section 4.3.1, Hysitron measurements showed that specimen D has the lowest hardness rather than specimen B. This difference might arise from several factors. Because of the effect of the soft substrate, the thinner specimen B coating results in larger indentation depth, compared with the thicker specimen D, at loads over 100mN (Table 4.17). Also, the lowest stiffness and lowest H^3/E^2 (plastic deformation resistance) of specimen B might also be the reasons of the highest indentation depth. More detailed information about stiffness are discussed with respect to the load-displacement curves described later.

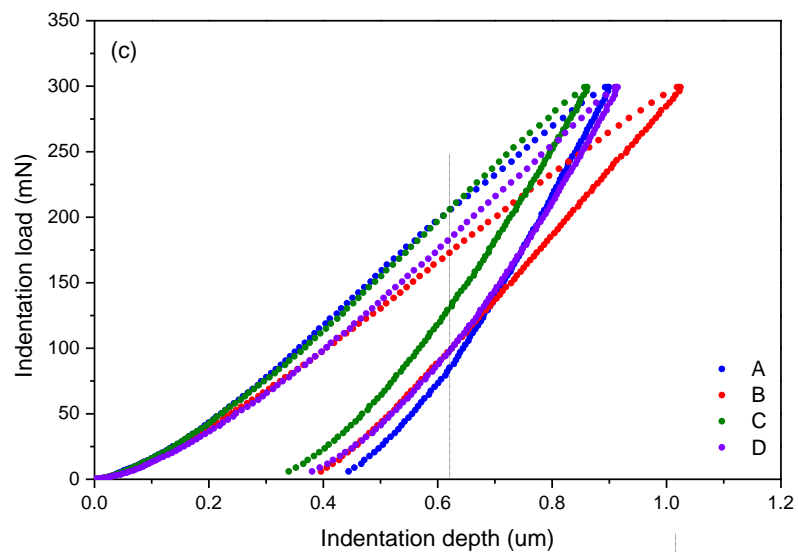
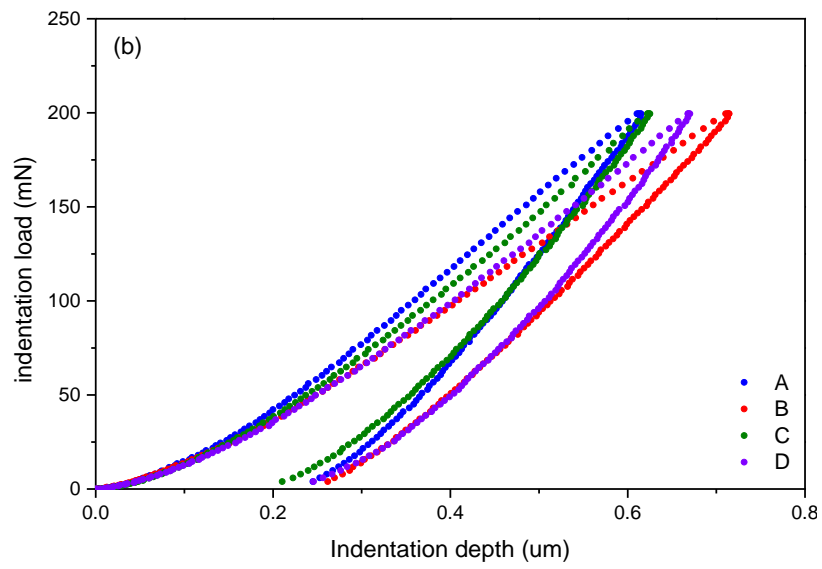
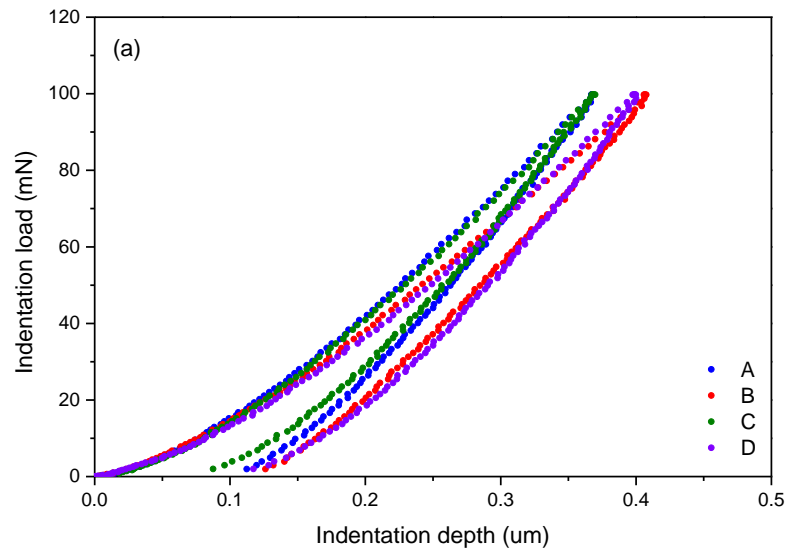
Specimen A exhibited the lowest total depth at loads of 100mN and 200mN, but at higher loads of 300mN to 500mN, specimen C had the lowest total depth (Table 4.16). This may also be attributed to the effect of the substrate (Table 4.17). It is well known that the result from coatings at relatively high loads is strongly influenced by substrate properties. Therefore, the lowest total depth changed from specimen A to specimen C with increasing loads from 200 mN to 300 mN due to the effects of the soft M2 steel substrate at the higher load. Specimen A was the more significantly influenced by the soft substrate as the coating thickness of specimen A is ~35 % less than specimen C.

Table 4.16: Total depth of each load for each sample

	100 mN	200 mN	300 mN	400 mN	500 mN
A (μm)	0.37	0.62	0.90	1.22	1.50
B (μm)	0.41	0.71	1.02	1.40	1.79
C (μm)	0.37	0.63	0.86	1.13	1.43
D (μm)	0.40	0.67	0.91	1.21	1.48

Table 4.17: Ratio of indentation depth to thickness at loads of 100 mN to 300 mN

	Thickness (μm)	Ratio (%) at 100 mN	Ratio (%) at 200 mN	Ratio (%) at 300 mN
A	4.2	8.81	14.76	21.43
B	5.31	7.72	13.37	19.21
C	5.65	6.55	11.15	15.22
D	5.99	6.68	11.19	15.19



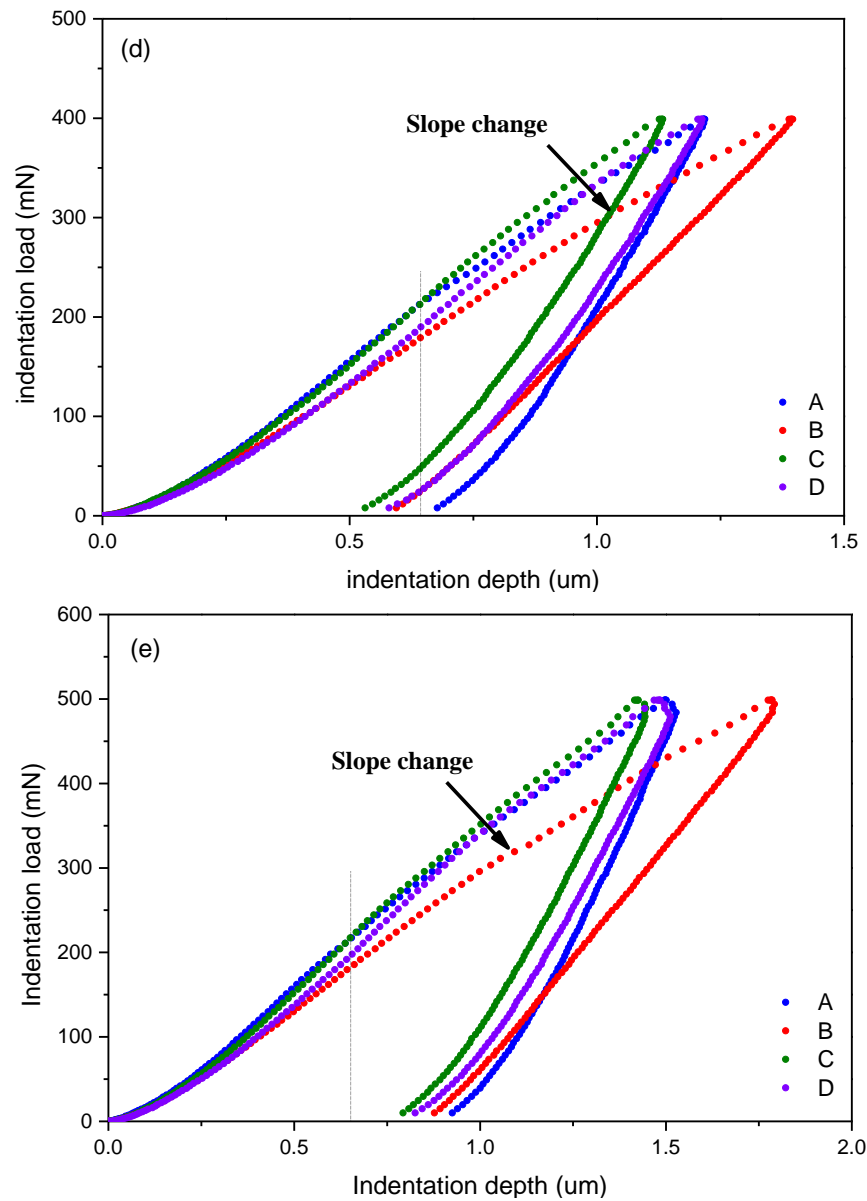


Fig. 4.21: Load-displacement curve to loads of (a) 100mN (b) 200mN (c) 300mN (d) 400mN (e) 500mN for specimen A.

From Figure 4.21 (a), the overall shapes of the indentation curves for all four specimens are similar exhibiting elastic behaviour relatively low loads. As shown in the green curve, specimen C shows the lowest indentation depth of $0.37\mu\text{m}$ and the highest % recovery value of 0.76 which is correlated to the lowest H^3/E^2 value and highest H/E value. As shown in Table 4.10 where H/E and H^3/E^2 values are presented, the material with higher H/E value is believed to have higher elastic recovery [117] which is similar to the nanoindentation data presented in this section. A similar phenomenon is observed

in Figure 4.21 (b) for indentation to a maximum load at 200mN. Specimen A has the higher value of H^3/E^2 indicating higher resistance to plastic deformation which can be confirmed in Figure 4.21 (a)-(e).

From Figure 4.21 (c), the slope of each loading curve reveals the differences in the stiffness of these four samples. Specimen B shows the lowest stiffness due to exhibiting the lowest slope in the loading curve, whilst specimen A shows the highest stiffness. Specimen C exhibits the highest stiffness at an indentation depth of $\sim 0.62\mu\text{m}$ (marked as a dotted line) and same phenomenon is observed under loads of 300mN and 400mN (Figure 4.21 (d) and Figure 4.21 (e)). This may be due to the effect of the differing coating thickness values. Specimen C is $\sim 35\%$ thicker than specimen A so that at higher loads the relatively soft substrate contributes significantly to the deformation behaviour of coating A.

It can be clearly seen that the slope of loading curve on specimen B changed at an indentation depth of $1.1\mu\text{m}$ and a 300mN load, as indicated by the arrows in Figure 4.21 (d) and Figure 4.21 (e). This discontinuity can be correlated to microstructural effects such as coating delamination from the substrate or crack generation [118, 119].

All four samples show a sudden drop (a nose) at the initial unloading curve after holding maximum load at 500mN. This creep effect at the maximum load may influence the unloading behaviour, especially when the unloading rate is slow [120]. This displacement increased slightly at the commencement of the unloading showing a negative slope in the initial part of the unloading curve. This is due to creep rate of the coating being higher than the initial unloading rate [121]. To eliminate this nose, it is suggested that holding time should be longer to allow the material to approach equilibrium prior to unloading. Clearly, a holding time of 8 seconds for 500 mN is apparently not enough. However, in the previous studies, holding times for nanoindentation of CrN-based coating ranges from 5s to 10s without such creep effects being evident [122, 123].

4.4.2 Deformation behaviour characterization

FIB plan view images and cross-sectional images from the 500mN spherical indentations on the four Cr(C)N coatings are shown in Figure 4.22 (a)-(d) and Figure 4.22 (e)-(f), respectively. The diameters of indented areas for specimen A to specimen D, were measured to be 6.84, 6.32, 5.79 and 6.05 μm , respectively. These diameters are consistent, relatively, with the indentation depths described earlier (Table 4.12 to Table 4.15). This suggests that larger indentation depth results in larger diameter of indented area.

As shown in Figure 4.22 (e) and (f), concentric ring cracks can be observed at the edges of the indents in specimens A and B which may be correlated to a higher degree of damage in these coatings. No similar cracks were seen in specimens C and D at this magnification, but some limited plastic deformation of substrate still can be seen in Figure 4.22 (g) and (h). The interfaces between the Cr(C)N layers, Cr wetting layer and M2 substrate are clearly deformed and no longer parallel. This correlates with the low plastic deformation resistance, H^3/E^2 (≤ 0.085). However, the thickness of the Cr(C)N layers is seen to be uniform across the indented area relative to the undeformed coatings shown in Figure 4.22 (e)-(h), indicating no plastic flow of the coating during indentation. The magnification of FIB is not enough to observe further details about the presence and nature of any cracking. The deformed Cr(C)N coatings were then characterized using TEM at higher magnification.

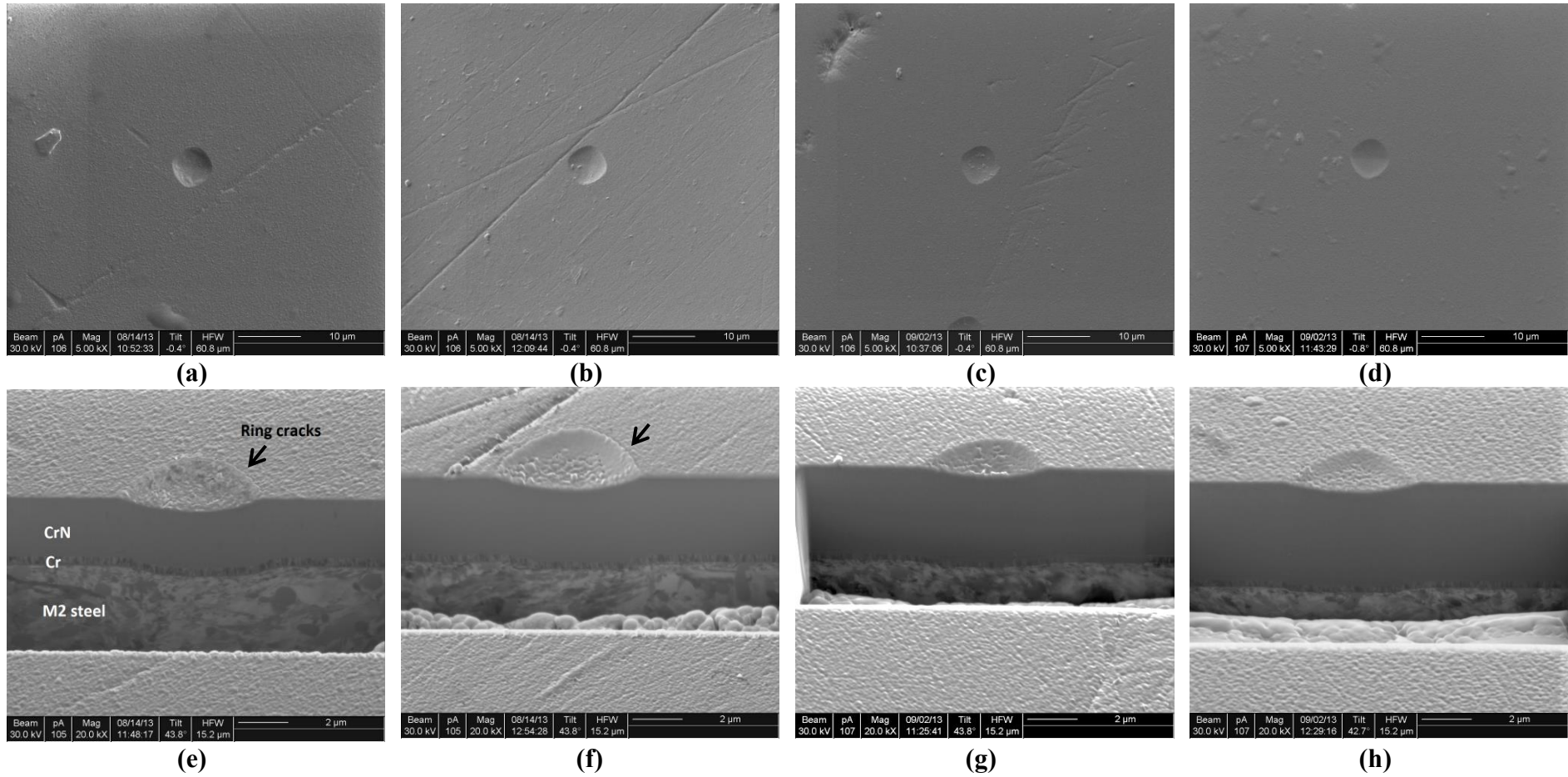
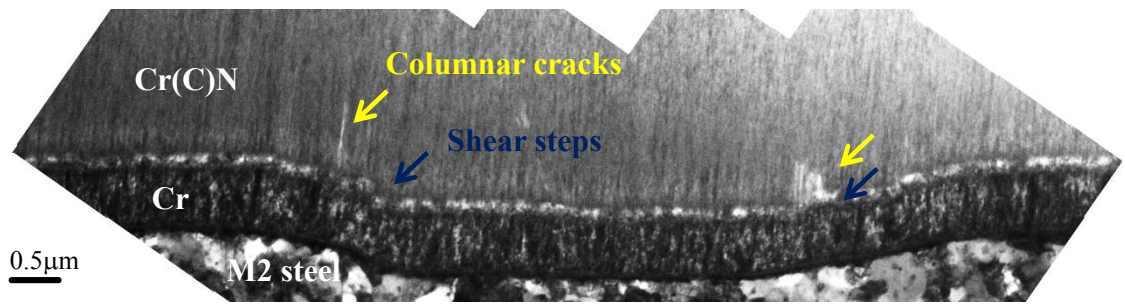
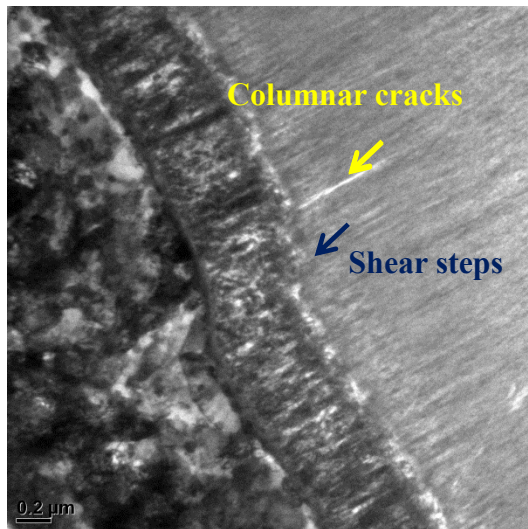


Figure 4.22: FIB images showing deformation behaviour after spherical nanoindentation with 500mN of (a) A (b) B (c) C (d) D for showing;
 (e) A (f) B (g) C (h) D showing cross-sectional view

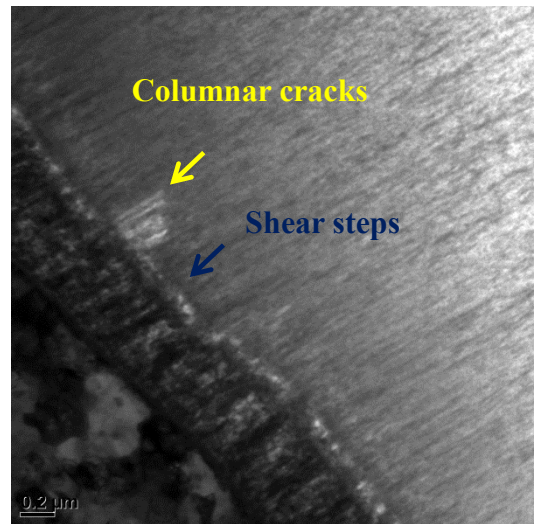
Figure 4.23 (a)-(d) shows cross-sectional bright field TEM images taken from the indented area, which were subject to nanoindentation at a load of 500 mN using a spherical indenter with a radius of 5 μm . Figure 4.23 (a) is recorded from the centre of the indented area and shows the overall deformation behaviour of the coating and the deformation in the wetting layer and the substrate. There are three types of cracks visible here, columnar cracks, shear steps and transverse cracks, each of these crack types is labeled in Figure 4.23 (a)-(c). Figure 4.23 (b) and (c) are taken from the left hand side and right hand side of indented area, respectively. These images show a small number of columnar cracks near the edges of the spherical indents, marked by yellow arrows. These fine columnar cracks are observed in the Cr(C)N layer closed to the Cr wetting layer and some of them extend into the Cr wetting layer. This suggests that the Cr wetting layer prevents crack propagation into the substrate. Columnar grain boundary sliding or shearing at grain boundaries (shear cracks), result in shear steps near the interface between the coating and the substrate at the edges of the indented area. Also, it is clear that the interfacial bonding between the Cr(C)N, Cr and the substrate are well maintained under loading even though the crack transversed the interfaces that separate them. Figure 4.23 (d) was taken close to the surface of the right-hand side of indented area. Very fine transverse cracks parallel to the coating surface can be seen in Figure 4.23 (d), marked by red arrows. [124].



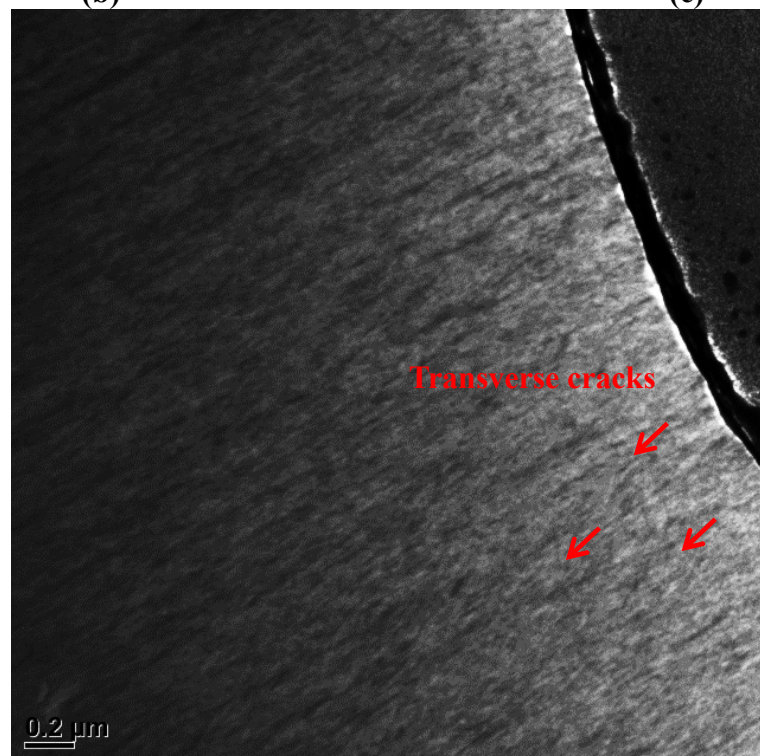
(a)



(b)



(c)



(d)

Figure 4.23: A bright field TEM image of (a) centre (b) left (c) right (d) top of indented area using spherical indenter under a 500mN of specimen B

4.4.3 Wear track characterization

Figures 4.24 (a)-(d) shows the wear track morphology of the Cr(C)N coatings after using a pin-on-disk triboindenter with a ruby sphere at 5N and 5000 cycles. As can be seen in Figure 4.24 (a), specimen A suffered the severest wear compared to the others. There are many grooves and evidence of spallation etc. along the sliding direction resulting from abrasion in the wear track. This indicates the removal of chips from the coating. Compared to specimen A, specimens B, C and D exhibited smoother wear tracks with relatively shallow grooves.

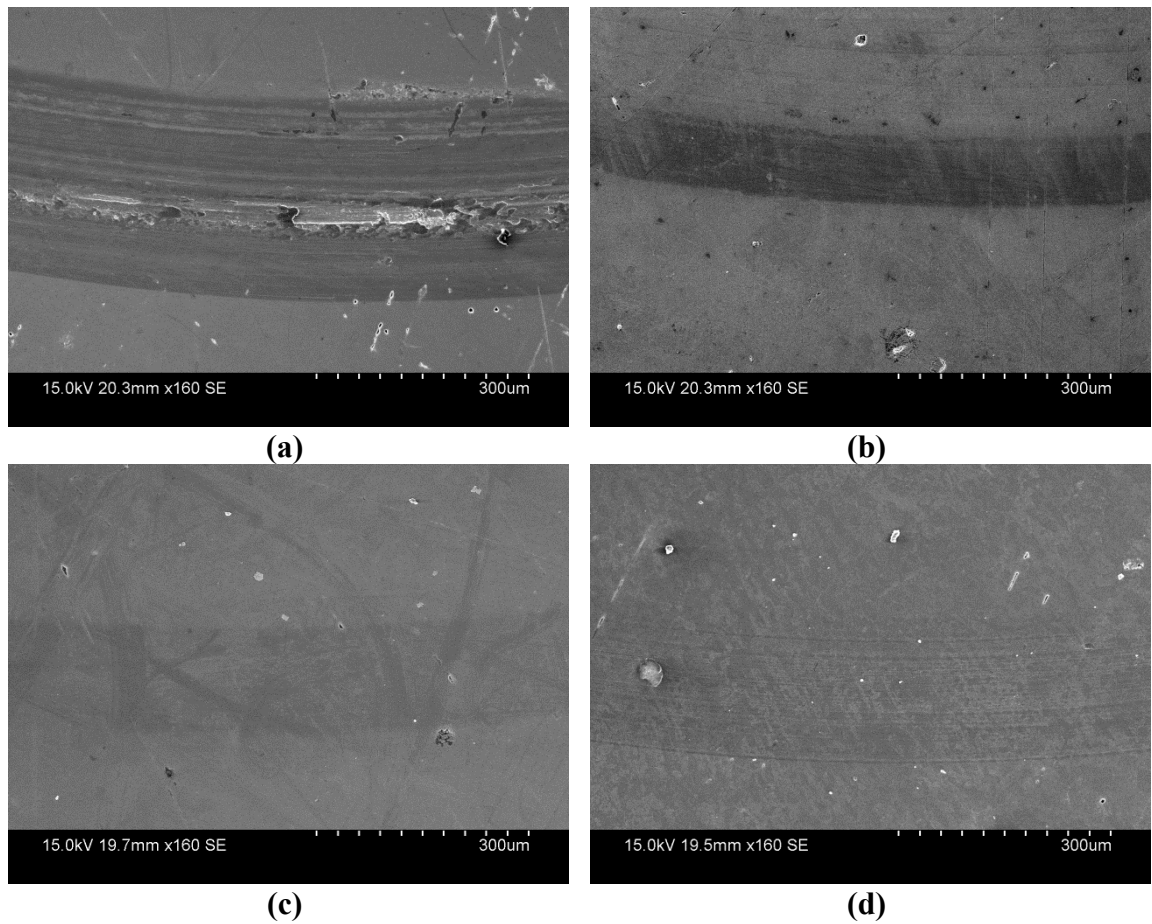
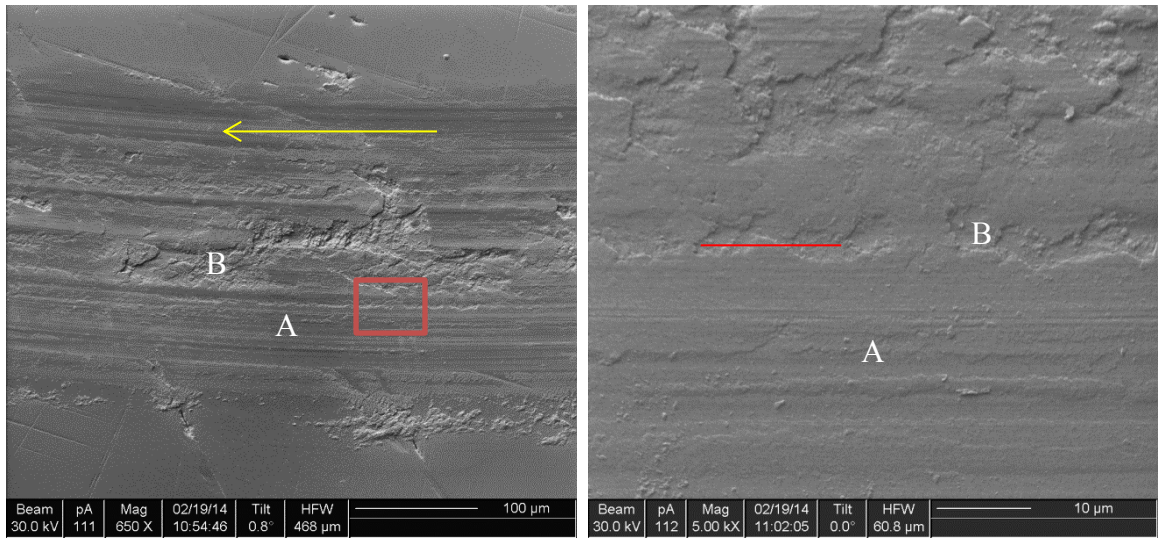


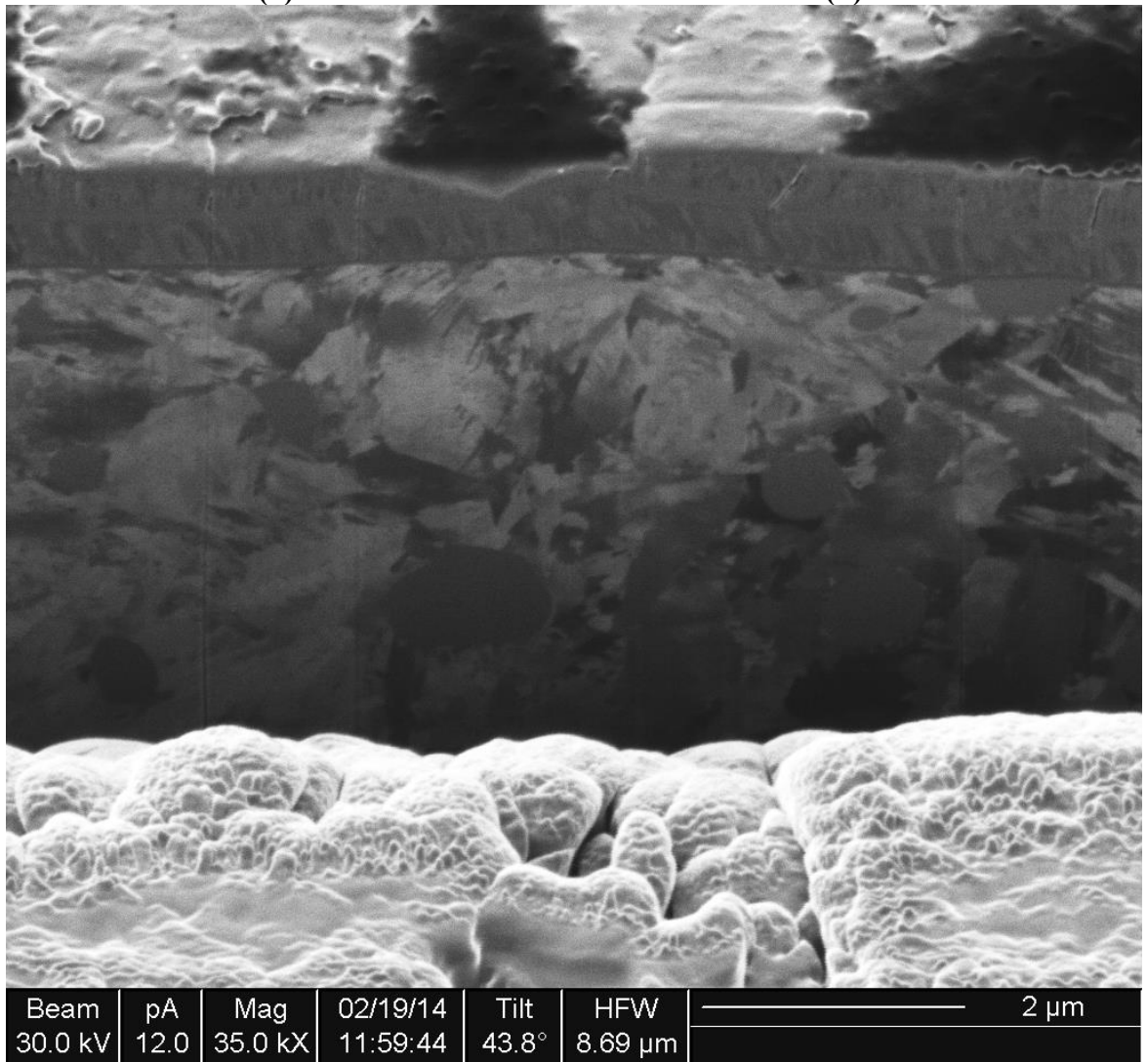
Figure 4.24: SEM images showing wear tracks after pin-on-disk wear testing for specimens (a) A (b) B (c) C (d) D

The morphologies of the wear track on the surface of specimen A shows features of abrasive wear, e.g. long parallel grooved induced by plowing and wear pits from material pullout, indicated by regions A and B, respectively (Figure 4.25 (a) and (b)). The morphological features, such as plowing, cracking and wear pits, confirm that abrasive wear is the dominant wear mechanism in specimen A. Nevertheless, plastic deformation was also observed in the wear track, which indicates that adhesive wear also occurred [125]. This phenomena can be correlated to the mechanical behaviour of specimen A: highest hardness, lowest H/E value and highest H^3/E^2 value showing its brittle characteristic [126]. A cross-sectional image of the wear track in specimen A was illustrated in Figure 4.25 (c). Specimen A exhibited a deep and rough wear track with many obvious cracks and chips showing that the wear debris are loose and easily removed the surface. Cracks running perpendicular to the sliding direction were also observed, which is consistent with the brittle nature of this specimen. Almost all of the coating in this specimen has been removed during wear. In most areas a section only a few hundred nanometres in thickness remains. In some areas all of the coating has been spalled away. In contrast, the relatively ductile Cr coating remains attached to the steel substrate and appears undamaged by the wear process.



(a)

(b)



(c)

Figure 4.25: FIB images showing wear track after pin-on-disk wear testing of (a)(b) plan view; (c) cross-sectional view for specimen A

The cross-sectional FIB images (Figure 4.26) show that all the Cr(C)N coatings exhibited good adhesion to the M2 substrate. Compared to specimen A, plan view images show that specimen B, C and D exhibited smoother wear tracks with shallow grooves. A cross-sectional image of specimen B shows that some cracks nucleated underneath the wear track, but the material has not spalled off the coating surface. It is known that the fracture could occur from coating defects such as droplets, cracks and chips. These coating defects could pull out from the coating leading to brittle fracture of the coating itself [127]. This indicates that the presence of carbon in the Cr(C)N coatings improves ductility and wear resistance. The main reason is that the Cr(C)N coatings with graphite phase can form transferred films on the surface of friction pairs, ruby balls. These transferred films can reduce volume wear ratio and hence improve the wear resistance. [8].

The depth of the wear tracks measured from the FIB cross-sectional images is summarized in Table 4.18. However, these values are not reliable because some of the FIB cross-sectional images are not located exactly in the middle of wear track. As shown in Table 4.18, the depth of the wear track (Δ Thickness) on specimen A ($\sim 3.04 \mu\text{m}$) is close to the thickness of CrN coating ($3.61 \mu\text{m}$) whilst the wear tracks on specimen B suggest only shallow grooves ($0.58 \mu\text{m}$) form on the surface. The higher depth of wear track can be related to the higher wear rate. The highest wear rate for specimen A might be due to the presence of Cr_2O_3 particles as abrasive particles [128]. The depth of the wear tracks for specimens C and D have similar values, which are 1.35 and $1.38 \mu\text{m}$. Such wear behaviour during wear testing can be explained by the H/E value and H^3/E^2 value. Many workers suggested that the coatings with higher H/E value exhibit better wear resistance [126, 129], such as lower wear rate [130] and fracture toughness [131]. As referred to the H/E value in section 4.3.1, the lowest H/E value (0.0657) in specimen A showed the most brittle characteristics. In this study no clear difference in the wear microstructure for specimens C and D could be discerned. Another important parameter of wear behaviour, H^3/E^2 , also reported by many workers. Feng suggested that the H^3/E^2 is inversely proportional to wear rate [132]. In this study, the higher H^3/E^2 value for specimens A (0.0838) and C (0.0843) and the lower H^3/E^2 value for specimens B (0.0744) and D (0.0688) is consistent with this observation.

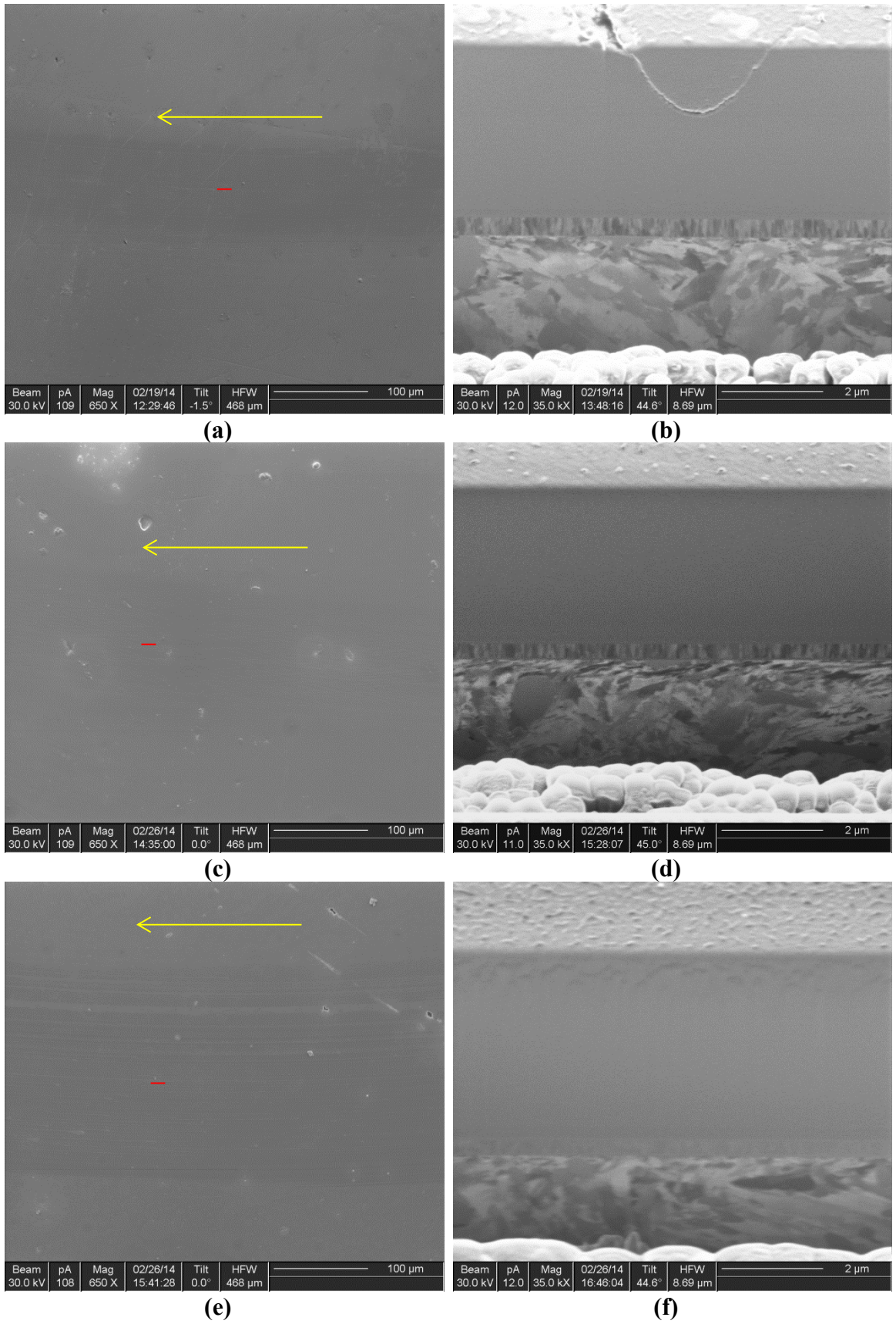


Figure 4.26: FIB images showing wear track after pin-on-disk wear testing for specimens (a) B (c) C (e) D in plan views; (b) B (d) C (e) D in cross-sectional views

Table 4.18: The thickness of four Cr(C)N coatings after wear testing

	A	B	C	D
Cr(C)N (μm)	0.55	4.69	4.33	5.10
Cr (μm)	0.52	0.48	0.45	0.48
Total (μm)	1.06	5.17	4.78	5.56
Original total thickness (μm)	4.10	5.75	6.08	6.95
Δ Thickness (μm)	3.04	0.58	1.35	1.38

* Δ Thickness=depth of wear track=original total thickness-total thickness after wear testing

4.5 Summary

It was shown that the carbon content in the Cr(C)N coatings increased with increasing graphite target current. The carbon additions in the coatings led to a change in phase equilibria from a Cr₂N-rich phase in C-free specimen A to a CrN-dominant phase in specimen B, C, and D. The carbon additions also led to denser and finer coatings. As the carbon content increased in the coatings, the hardness, modulus, and coefficient of friction decreased. Furthermore, in the deformation mechanism studies, it was found that the toughness of Cr(C)N coatings improved and the wear resistance increased due to the presence of carbon additions.

Chapter 5 General discussion

5.1 Introduction

This chapter discusses the general effects of carbon additions to Cr(C)N coatings in terms of their microstructure and mechanical properties. As described in Chapter 4, although the hardness and Young's modulus are generally decreased by increasing the carbon content, the relationship between these parameters is not a simple or linear one. That is, specimen C, that contained around 35 at.% C was measured to be harder than both specimens B and D, that contained either lower or higher concentrations of C, respectively. Furthermore, the coefficient of friction was generally decreased with increasing carbon, but the coefficient of friction that was measured for specimen A was lower than values reported elsewhere in the literature [7, 8, 35]. This is because the mechanical properties and tribological properties of these Cr(C)N coatings are dependent on a range of factors, such as phase equilibria, bonding type, surface roughness, grain size and coating thickness, which themselves do not vary independently with coating composition or deposition parameters.

5.2 Microstructure and composition versus mechanical properties

As expected, the carbon content in the Cr(C)N coatings increased with increasing graphite target current. It is evident that the increasing C content on the coatings had several different effects on the coating microstructure.

First, the phase equilibria changed such that that CrN volume fraction increased relative to the fraction of Cr₂N with increasing carbon content as was determined by TEM electron diffraction patterns and XRD analysis. As described in the literature review, it is known that Cr₂N (H = 15-27GPa) is harder than CrN (H = 11-15GPa). This is because the degree of covalent bonding in Cr₂N is higher than in CrN. Therefore, softening with increasing volume fraction of CrN might be expected. However, the volume fractions of the two phases in each coating were not experimentally determined. Further analysis using methods such XRD Rietveld analysis [133] could be applied to these materials to determine such volume fractions and lattice parameters [134].

Second, it is evident that at the highest C concentrations there was excess carbon (or nitrogen) relative to that required to form stoichiometric CrN. It is probable, then, that the excess carbon formed sp^2 carbon bonds, C-N bonds or Cr-C bonds in these coatings, which was determined by XPS. These Cr-C bonds might relate to amorphous phases or a very fine-grained structured chromium carbide, although such phases were not observed in the XRD spectra or TEM electron diffraction patterns. It is also suggested that the possible presence of chromium carbide-based phases resulted in lower hardness values. Higher resolution TEM analysis could be used to investigate the possible presence of these phases in more detail.

Third, the C additions led to a refinement in grain size. This may lead to Hall-Petch effects, both hardening and softening (that is the reverse Hall-Petch effect). In fine grained coatings (such as specimen C), the high fraction of grain boundaries may have impeded dislocation motion, and hence, the coating was strengthened. However, at very high carbon contents (such as specimen D), a large amount of carbon atoms in the coating may have resulted in very fine grain sizes promoting grain boundary sliding. Higher resolution TEM studies may be useful in generating precise measurements of grain size in each coating as these were difficult to discern on the basis of the micrographs obtained in this study. Further, modeling studies which allow analysis of Hall-Petch type effects on hardness may also be useful.

In the wear tests performed, specimen A, which is predominantly Cr_2N , has a lower value of coefficient of friction than previous studies reported in the literature. This low value for specimen A may be due to the presence of chromium oxide in the coatings and which leads to a decrease in the coefficient of friction [135]. The coefficients of friction for specimens B, C and D were measured within the range of previous studies. With the increasing carbon doping in the coatings, the coefficient of frictions decreased. This might due to the presence of sp^2 carbon bonds and also possibly Cr-C bonds. Further wear testing studies would include tests against with other materials e.g. Si_3N_4 and Al_2O_3 [136] and for longer periods. The wear behaviour would be further characterized using scratch tests. The scratch test is often used to evaluate the adhesion between the coating and substrate. It provides a dynamic examination of wear and deformation behaviour

with an increasing scratch depth varying with the applied load [135]. The applied load at which failure occurs is called the critical load and plays an important role in determining coating spallation behaviour [137].

As suggested above, phases with low values of coefficient of friction, such as chromium carbides and chromium oxides, may be present in the deposited coatings. However, these phases were not directly observed in this study. To determine whether these phases were present, further studies using high resolution TEM may be valuable.

5.3 Deformation mechanism v.s. Indentation curves

Through a combination of cross-sectional imaging and load-displacement curve, an understanding of deformation behaviour of these coatings could be achieved. With increasing carbon additions in the coatings, the coatings became less brittle. The carbon additions also enhanced toughness to reduce the degree of cracking. The higher toughness might relate to a higher H/E value. This suggests that sp^2 carbon bonds improved toughness, but at the expense of hardness. Cr(C)N coatings with no or small amounts of carbon additions with lower H/E values exhibited lower toughness (e.g. specimen A). The enhanced toughness with carbon additions may also be due to the presence of a denser columnar structure. During wear testing, specimen C and D did not show any evidence of cracking in the wear track showing that the toughness was improved.

Ideally, coatings should exhibit both high hardness and good toughness. It is evident in this study that carbon additions increase toughness, but at the expense of hardness. Previous studies have shown that to improve toughness without loss of hardness through carbon additions, complex coating architectures are required, for example multilayer coatings, such as CrCN/CrN [97, 138]. Recently, there have been a number of studies on Cr-X-N (CrN-based) ternary coatings with various elemental additions. It has been reported that other additions such as W [139], Al [140], V [140], added to CrN coatings improved toughness without loss of hardness.

Chapter 6 Conclusions and summary

This work has studied the interrelations between microstructure, mechanical and tribological properties of Cr(C)N coatings with various carbon contents. A range of Cr(C)N coatings, with varying C contents, was prepared using a closed-field unbalanced magnetron sputtering ion plating system on to M2 steel substrates.

1. With increasing the graphite target current from 0, 1.5, 3.5 and 4.5 A, the total thickness, including Cr(C)N and the Cr wetting layer, were increased from 4.1, 5.75, 6.08 and 6.95 μm , respectively, which indicates that the deposition rate increased with increasing graphite target currents.
2. The carbon-free CrN coating exhibited a coarse columnar crystalline structure with some irregularly shaped intergranular voids. When carbon was added into the coatings, the Cr(C)N coatings exhibit a finer and denser columnar structure with narrow inter-crystalline voids. The roughness and the grain size decreased with increasing carbon content because the carbon atoms act to promote nucleation.
3. The carbon additions in the Cr(C)N coatings replace nitrogen in either Cr_2N or CrN and lead to a change in phase equilibria promoting CrN at the expense of Cr_2N , which was determined by XPS, XRD and TEM. With large amounts of carbon in the coatings, it is suggested that the excess carbon might exist as an amorphous carbon phase or, carbon nitride, chromium carbide in the coatings, however, this is not observed directly in this study. To determine the presence of these phases, further investigation using high resolution TEM would be required.

4. The XPS results show that the carbon mainly exists as Cr-C bonds and sp^2 C-C/C-N bonds in all four specimens. The presence of sp^2 carbon and, possibly, Cr-C bonds in the coatings can reduce the coefficients of friction. As the sp^2 carbon content increased with graphite target current in the coatings, the coefficients of friction decreased. However, the carbon-free CrN coating exhibited a lower value than expected. It is suggested that this low value is due to the presence of chromium oxide (determined by XPS) and Cr_2N in this coatings.

5. With increasing carbon content in the coatings, the hardness and modulus generally decreased. This would suggest that the sp^2 bonds in the coating might not only reduce the friction of coefficient, but also reduce the hardness and modulus. It is noticed that hardness and modulus increased with further carbon additions and then decreased further with even higher amount of carbon additions. These both strengthening and softening phenomena may be explained by Hall-Petch effect and solid solution effect of C dissolved in the CrN unit cells.

6. The analysis of the deformation and wear mechanism shows that the cracks occurred in the Cr(C)N coatings with low carbon content. With increasing doping in the Cr(C)N coatings, the toughness and brittleness were improved and even hardness is decreased. However, the deformation of Cr(C)N coatings is still not clear since cracking only occurred at a maximum load of 500 mN. Further investigation of deformation mechanism in Cr(C)N would be required with more specimens with different carbon content at higher loads and the wear behaviour would be determined using wear rate calculated from the volume of material removed.

References

- [1] A. Conde, C. Navas, A. B. Cristóbal, J. Housden, and J. de Damborenea, "Characterisation of corrosion and wear behaviour of nanoscaled e-beam PVD CrN coatings", *Surface and Coatings Technology*, **201** [6] pp. 2690-2695 (2006).
- [2] G. Wei, A. Rar, and J. A. Barnard, "Composition, structure, and nanomechanical properties of DC-sputtered CrNx ($0 \leq x \leq 1$) thin films", *Thin Solid Films*, **398–399** [0] pp. 460-464 (2001).
- [3] P. J. Kelly, and R. D. Arnell, "Magnetron sputtering: a review of recent developments and applications", *Vacuum*, **56** [3] pp. 159-172 (2000).
- [4] H. Scheerer, E. M. Slomski, T. Troßmann, and C. Berger, "Characterization of CrN coatings concerning the potential to cover surface imperfections", *Surface and Coatings Technology*, **205, Supplement 1** [0] pp. S47-S50 (2010).
- [5] C. Gautier, and J. Machet, "Study of the growth mechanisms of chromium nitride films deposited by vacuum ARC evaporation", *Thin Solid Films*, **295** [1–2] pp. 43-52 (1997).
- [6] P. Wiecinski, J. Smolik, H. Garbacz, and K. J. Kurzydowski, "Microstructure and mechanical properties of nanostructure multilayer CrN/Cr coatings on titanium alloy", *Thin Solid Films*, **519** [12] pp. 4069-4073 (2011).
- [7] E. Y. Choi, M. C. Kang, D. H. Kwon, D. W. Shin, and K. H. Kim, "Comparative studies on microstructure and mechanical properties of CrN, Cr–C–N and Cr–Mo–N coatings", *Journal of Materials Processing Technology*, **187–188** [0] pp. 566-570 (2007).
- [8] H. Pengfei, and J. Bailing, "Study on tribological property of CrCN coating based on magnetron sputtering plating technique", *Vacuum*, **85** [11] pp. 994-998 (2011).
- [9] H. Schatten, "Scanning Electron Microscopy for the Life Sciences," Cambridge University Press, 2012.
- [10] J. M. Cairney, P. R. Munroe, and J. H. Schneibel, "Examination of fracture surfaces using focused ion beam milling", *Scripta Materialia*, **42** [5] pp. 473-478 (2000).
- [11] J. Li, T. Malis, and S. Dionne, "Recent advances in FIB–TEM specimen preparation techniques", *Materials Characterization*, **57** [1] pp. 64-70 (2006).
- [12] P. R. Munroe, and D. McGrouther, "Principles and Applications of Focused Ion Beam Milling", *FIB Workshop Notes, Electron Microscope Unit, University of New South Wales*, (2005).
- [13] C. Ducati. "Natural Sciences Tripos Part III MATERIALS SCIENCE T2: Electron Microscopy," <http://www.msm.cam.ac.uk/teaching/partIII/courseT2/T2H.pdf>.
- [14] S. Chatterjee, S. Gadad, and T. Kundu, "Atomic force microscopy", *Resonance*, **15** [7] pp. 622-642 (2010).
- [15] "Atomic Force Microscopy Of Soft Or Fragile Materials Using TappingMode Imaging Technology From Veeco," March 23, 2014; <http://www.azom.com/article.aspx?ArticleID=3279>.
- [16] E. Martínez, J. Romero, A. Lousa, and J. Esteve, "Nanoindentation stress–strain curves as a method for thin-film complete mechanical characterization: application to nanometric CrN/Cr multilayer coatings", *Applied Physics A*, **77** [3-4] pp. 419-427 (2003).
- [17] L. Ma, L. Levine, R. Dixson, D. Smith, and D. Bahr, "Effect of the Spherical Indenter Tip Assumption on the Initial Plastic Yield Stress," *Nanoindentation in Materials Science*, D. J. Nemecek, ed., 2012.
- [18] W. C. Oliver, and G. M. Pharr, "Measurement of hardness and elastic modulus by instrumented indentation: Advances in understanding and refinements to methodology", *Journal of Materials Research*, **19** [1] pp. 3-20 (2004).
- [19] J. S. Field, and M. V. Swain, "Determining the mechanical properties of small volumes of material from submicrometer spherical indentations", *Journal of Material Research*,

- (1995).
- [20] E. Weppelmann, and M. V. Swain, "Investigation of the stresses and stress intensity factors responsible for fracture of thin protective films during ultra-micro indentation tests with spherical indenters", *Thin Solid Films*, **286** [1–2] pp. 111-121 (1996).
- [21] M. V. Swain, and J. T. Hagan, "Indentation plasticity and the ensuing fracture of glass", *J. Phys. D: Appl. Phys.*, **9** (1976).
- [22] E. S. Gadelmawla, M. M. Koura, T. M. A. Maksoud, I. M. Elewa, and H. H. Soliman, "Roughness parameters", *Journal of Materials Processing Technology*, **123** [1] pp. 133-145 (2002).
- [23] M. Pakala, and R. Y. Lin, "Reactive sputter deposition of chromium nitride coatings", *Surface and Coatings Technology*, **81** [2–3] pp. 233-239 (1996).
- [24] J. W. Lee, S. K. Tien, and Y. C. Kuo, "The effects of pulse frequency and substrate bias to the mechanical properties of CrN coatings deposited by pulsed DC magnetron sputtering", *Thin Solid Films*, **494** [1–2] pp. 161-167 (2006).
- [25] M. Odén, C. Ericsson, G. Håkansson, and H. Ljungcrantz, "Microstructure and mechanical behavior of arc-evaporated Cr–N coatings", *Surface and Coatings Technology*, **114** [1] pp. 39-51 (1999).
- [26] J. W. Lee, Y. C. Kuo, C. J. Wang, L. C. Chang, and K. T. Liu, "Effects of substrate bias frequencies on the characteristics of chromium nitride coatings deposited by pulsed DC reactive magnetron sputtering", *Surface and Coatings Technology*, **203** [5–7] pp. 721-725 (2008).
- [27] S. K. Pal, "Synthesis, Characterization and Tribological Behavior of Nitrogen-Doped Chromium-Diamond-Like Carbon Nanocomposite Thin Films", (2004).
- [28] P. Engel, G. Schwarz, and G. K. Wolf, "Corrosion and mechanical studies of chromium nitride films prepared by ion-beam-assisted deposition", *Surface and Coatings Technology*, **98** [1–3] pp. 1002-1007 (1998).
- [29] R. Saha, R. B. Inturi, and J. A. Barnard, "Structural and mechanical characterization of Cr-Ta-N hard coatings prepared by reactive magnetron sputtering", *Surface and Coatings Technology*, **82** [1–2] pp. 42-47 (1996).
- [30] T. Polcar, T. Vitu, L. Cvrcek, J. Vyskocil, and A. Cavaleiro, "Effects of carbon content on the high temperature friction and wear of chromium carbonitride coatings", *Tribology International*, **43** [7] pp. 1228-1233 (2010).
- [31] M. H. Sohi, A. A. Kashi, and S. M. M. Hadavi, "Comparative tribological study of hard and crack-free electrodeposited chromium coatings", *Journal of Materials Processing Technology*, **138** [1–3] pp. 219-222 (2003).
- [32] H. Ichimura, and I. Ando, "Mechanical properties of arc-evaporated CrN coatings: Part I — nanoindentation hardness and elastic modulus", *Surface and Coatings Technology*, **145** [1–3] pp. 88-93 (2001).
- [33] M. Odén, J. Almer, G. Håkansson, and M. Olsson, "Microstructure–property relationships in arc-evaporated Cr–N coatings", *Thin Solid Films*, **377–378** [0] pp. 407-412 (2000).
- [34] F. D. Lai, and J. K. Wu, "High temperature and corrosion properties of cathodic-arc-plasma-deposited CrN coatings", *Surface and Coatings Technology*, **64** [1] pp. 53-57 (1994).
- [35] B. Warcholiński, A. Gilewicz, Z. Kukliński, and P. Myśliński, "Arc-evaporated CrN, CrN and CrCN coatings", *Vacuum*, **83** [4] pp. 715-718 (2008).
- [36] J. Almer, M. Odén, and G. Håkansson, "Microstructure and thermal stability of arc-evaporated Cr–C–N coatings", *Philosophical Magazine*, **84** [7] pp. 611-630 (2004).
- [37] M. Čekada, P. Panjan, M. Maček, and P. Šmíd, "Comparison of structural and chemical properties of Cr-based hard coatings", *Surface and Coatings Technology*, **151–152** [0] pp. 31-35 (2002).
- [38] T. Polcar, L. Cvrček, P. Široký, and R. Novák, "Tribological characteristics of CrCN

- coatings at elevated temperature”, *Vacuum*, **80** [1–3] pp. 113-116 (2005).
- [39] C. K. Park, S. M. Chang, H. S. Uhm, S. H. Seo, and J. S. Park, “XPS and XRR studies on microstructures and interfaces of DLC films deposited by FCVA method”, *Thin Solid Films*, **420–421** [0] pp. 235-240 (2002).
- [40] X. M. He, N. Baker, B. A. Kehler, K. C. Walter, M. Nastasi, and Y. Nakamura, “Structure, hardness, and tribological properties of reactive magnetron sputtered chromium nitride films”, *Journal of Vacuum Science & Technology A: Vacuum, Surfaces, and Films*, **18** [1] pp. 30-36 (2000).
- [41] C. Y. Tong, J. W. Lee, C. C. Kuo, S. H. Huang, Y. C. Chan, H. W. Chen, and J. G. Duh, “Effects of carbon content on the microstructure and mechanical property of cathodic arc evaporation deposited CrCN thin films” , *Surface and Coatings Technology*, **231** [0] pp. 482-486.
- [42] T. Hurkmans, D. B. Lewis, J. S. Brooks, and W. D. Münz, “Chromium nitride coatings grown by unbalanced magnetron (UBM) and combined arc/unbalanced magnetron (ABS™) deposition techniques”, *Surface and Coatings Technology*, **86–87, Part 1** [0] pp. 192-199 (1996).
- [43] S. K. Pradhan, C. Nouveau, A. Vasin, and M. A. Djouadi, “Deposition of CrN coatings by PVD methods for mechanical application”, *Surface and Coatings Technology*, **200** [1–4] pp. 141-145 (2005).
- [44] R. D. Arnell, P. J. Kelly, and J. W. Bradley, “Recent developments in pulsed magnetron sputtering”, *Surface and Coatings Technology*, **188–189** [0] pp. 158-163 (2004).
- [45] A. A. Solov'ev, N. S. Sochugov, K. V. Oskomov, and S. V. Rabotkin, “Investigation of plasma characteristics in an unbalanced magnetron sputtering system”, *Journal Name: Plasma Physics Reports; Journal Volume: 35; Journal Issue: 5; Other Information: DOI: 10.1134/S1063780X09050055; Copyright (c) 2009 Pleiades Publishing, Ltd., pp. Medium: X; Size: page(s) 399-408* (2009).
- [46] K. Laing, J. Hampshire, D. Teer, and G. Chester, “The effect of ion current density on the adhesion and structure of coatings deposited by magnetron sputter ion plating”, *Surface and Coatings Technology*, **112** [1–3] pp. 177-180 (1999).
- [47] S. Yang, D. Camino, A. H. S. Jones, and D. G. Teer, “Deposition and tribological behaviour of sputtered carbon hard coatings”, *Surface and Coatings Technology*, **124** [2–3] pp. 110-116 (2000).
- [48] J. Vyskocil, and J. Musil, “Cathodic arc evaporation in thin film technology”, *Journal of Vacuum Science & Technology A: Vacuum, Surfaces, and Films*, **10** [4] pp. 1740-1748 (1992).
- [49] B. Warcholinski, and A. Gilewicz, “Multilayer coatings on tools for woodworking”, *Wear*, **271** [11–12] pp. 2812-2820 (2011).
- [50] Y. Nakanishi, A. Miyake, H. Kominami, T. Aoki, Y. Hatanaka, and G. Shimaoka, “Preparation of ZnO thin films for high-resolution field emission display by electron beam evaporation”, *Applied Surface Science*, **142** [1–4] pp. 233-236 (1999).
- [51] K. K. Wasa, Makoto; Adachi, Hideaki, *Thin Film Materials Technology - Sputtering of Compound Materials*, William Andrew Publishing/Noyes.
- [52] A. J. Haq, “Deformation Behaviour of Diamond-like Carbon Coatings on Silicon Substrates,” University of New South Wales, 2008.
- [53] Q. Kong, L. Ji, H. Li, X. Liu, Y. Wang, J. Chen, and H. Zhou, “Influence of substrate bias voltage on the microstructure and residual stress of CrN films deposited by medium frequency magnetron sputtering”, *Materials Science and Engineering: B*, **176** [11] pp. 850-854 (2011).
- [54] Z. Liu, G. d. Wang, and W. Gao, “Properties of 310S stainless steel coatings produced by unbalanced magnetron sputter deposition”, *Materials Characterization*, **54** [4–5] pp. 466-472 (2005).
- [55] S. Grasser, R. Daniel, and C. Mitterer, “Microstructure modifications of CrN coatings by

- pulsed bias sputtering”, *Surface and Coatings Technology*, **206** [22] pp. 4666-4671 (2012).
- [56] H. Era, Y. Ide, A. Nino, and K. Kishitake, “TEM study on chromium nitride coatings deposited by reactive sputter method”, *Surface and Coatings Technology*, **194** [2–3] pp. 265-270 (2005).
- [57] C. L. Chang, J. Y. Jao, W. Y. Ho, and D. Y. Wang, “Influence of bi-layer period thickness on the residual stress, mechanical and tribological properties of nanolayered TiAlN/CrN multi-layer coatings”, *Vacuum*, **81** [5] pp. 604-609 (2007).
- [58] J. Lin, J. J. Moore, W. D. Sproul, B. Mishra, Z. Wu, and J. Wang, “The structure and properties of chromium nitride coatings deposited using dc, pulsed dc and modulated pulse power magnetron sputtering”, *Surface and Coatings Technology*, **204** [14] pp. 2230-2239 (2010).
- [59] B. Warcholinski, A. Gilewicz, J. Ratajski, Z. Kuklinski, and J. Rochowicz, “An analysis of macroparticle-related defects on CrCN and CrN coatings in dependence of the substrate bias voltage”, *Vacuum*, **86** [9] pp. 1235-1239 (2012).
- [60] P. Briois, D. Merics, V. Demange, O. Banakh, F. Sanchette, and A. Billard, “Characterizations of CrN/a-CN_x nanolayered coatings deposited by DC reactive magnetron sputtering of Cr and graphite targets”, *Vacuum*, **86** [2] pp. 206-209 (2011).
- [61] J. Esteve, J. Romero, M. Gómez, and A. Lousa, “Cathodic chromium carbide coatings for molding die applications”, *Surface and Coatings Technology*, **188–189** [0] pp. 506-510 (2004).
- [62] G. G. Fuentes, M. J. Díaz de Cerio, J. A. García, R. Martínez, R. Bueno, R. J. Rodríguez, M. Rico, F. Montalá, and Y. Qin, “Gradient CrCN cathodic arc PVD coatings”, *Thin Solid Films*, **517** [20] pp. 5894-5899 (2009).
- [63] Q. Wang, F. Zhou, X. Ding, Z. Zhou, C. Wang, W. Zhang, L. K. Y. Li, and S. T. Lee, “Microstructure and water-lubricated friction and wear properties of CrN(C) coatings with different carbon contents”, *Applied Surface Science*, **268** [0] pp. 579-587 (2013).
- [64] T. Ishitani, H. Tsuboi, T. Yaguchi, and H. Koike, “Transmission electron microscope sample preparation using a focused ion beam”, *Journal of Electron Microscopy*, **43** [5] pp. 322-326 (1994).
- [65] L. A. Giannuzzi, and F. A. Stevie, “A review of focused ion beam milling techniques for TEM specimen preparation”, *Micron*, **30** [3] pp. 197-204 (1999).
- [66] P. K. Chu, S. Qin, C. Chan, N. W. Cheung, and L. A. Larson, “Plasma immersion ion implantation—a fledgling technique for semiconductor processing”, *Materials Science and Engineering: R: Reports*, **17** [6–7] pp. 207-280 (1996).
- [67] M. R. Lee, P. A. Bland, and G. Graham, “Preparation of TEM samples by focused ion beam (FIB) techniques: Applications to the study of clays and phyllosilicates in meteorites”, *Mineralogical Magazine*, **67** [3] pp. 581-592 (2003).
- [68] M. W. Phaneuf, “Applications of focused ion beam microscopy to materials science specimens”, *Micron*, **30** [3] pp. 277-288 (1999).
- [69] P. R. Munroe, “The application of focused ion beam microscopy in the material sciences”, *Materials Characterization*, **60** [1] pp. 2-13 (2009).
- [70] L. Reimer, and H. Kohl, *Transmission Electron Microscopy: Physics of Image Formation*, Fifth ed., Springer series in optical sciences, 2008.
- [71] M. H. Loretto, *Electron Beam Analysis of Materials*, Second ed., Chapman & Hall 1994.
- [72] B. D. Cullity, *Elements of x-ray diffraction*, Second ed., Addison-Wesley Pub. Co. , 1978.
- [73] S. R. K. Sundaram, “Atomic Resolution Analytical Electron Microscopy Study of Multiferroic-Ferromagnetic Interfaces,” Ph.D thesis, School of Materials Science and Engineering, The University of New South Wales, 2012.
- [74] V. S. Ramachandran, and J. J. Beaudoin, "Handbook of Analytical Techniques in Concrete Science and Technology," William Andrew Publishing/Noyes, 2001.
- [75] J. W. Seok, N. M. Jadeed, and R. Y. Lin, “Sputter-deposited nanocrystalline Cr and CrN

- coatings on steels”, *Surface and Coatings Technology*, **138** [1] pp. 14-22 (2001).
- [76] G. W. Nelson, “Covalently bonded protein surfaces on poly(methyl methacrylate): Characterization by X-ray photoelectron spectroscopy and atomic force microscopy,” Master Thesis, Queen's University, 2008.
- [77] C. Malitesta, I. Losito, F. Scordari, and E. Schingaro, “XPS investigation of titanium in melanites from Monte Vulture (Italy)”, *European Journal of Mineralogy*, **7** [4] pp. 847-858 (1995).
- [78] "A practical guide to SPM," 29 March, 2014; http://www.veeco.com/pdfs/library/SPM_Guide_0829_05_166.pdf.
- [79] P. Eaton, and P. West, *Atomic Force Microscopy*, Oxford University Press, Oxford, 2010.
- [80] G. Stachowiak, and A. W. Batchelor, "Experimental Methods in Tribology," Elsevier Science, 2004.
- [81] K. Holmberg, A. Matthews, and H. Ronkainen, “Coatings tribology—contact mechanisms and surface design”, *Tribology International*, **31** [1–3] pp. 107-120 (1998).
- [82] A. C. Fischer-Cripps, “A review of analysis methods for sub-micron indentation testing”, *Vacuum*, **58** [4] pp. 569-585 (2000).
- [83] T. J. Bell, A. Bendeli, J. S. Field, M. V. Swain, and E. G. Thwaite, “The Determination of Surface Plastic and Elastic Properties by Ultra Micro-indentation”, *Metrologia*, **28** [6] pp. 463 (1991).
- [84] J. Malzbender, “Comment on hardness definitions”, *Journal of the European Ceramic Society*, **23** [9] pp. 1355-1359 (2003).
- [85] A. C. Fischer-Cripps, *Nanoindentation*, Springer, New York, N.Y. ; London, 2002.
- [86] A. B. T J Bell, J S Field, M V Swain and E G Thwaite, “The Determination of Surface Plastic and Elastic Properties by Ultra Micro-indentation”.
- [87] J. Menčík, and M. V. Swain, “Errors associated with depth-sensing microindentation tests”, *Journal of Materials Research* **10** [06] pp. 1491-1501 (1995).
- [88] Y. T. Cheng, and C. M. Cheng, “Effects of 'sinking in' and 'piling up' on estimating the contact area under load in indentation”, *Philosophical Magazine Letters*, **78** [2] pp. 115-120 (1998).
- [89] R. F. Cook, and G. M. Pharr, “Direct Observation and Analysis of Indentation Cracking in Glasses and Ceramics”, *Journal of the American Ceramic Society*, **73** [4] pp. 787-817 (1990).
- [90] S. Han, J. H. Lin, G. H. Wang, and H. C. Shih, “The effect of preferred orientation on the mechanical properties of chromium nitride coatings deposited on SKD11 by unbalanced magnetron sputtering”, *Materials Letters*, **57** [5–6] pp. 1202-1209 (2003).
- [91] G. P. López, D. G. Castner, and B. D. Ratner, “XPS O 1s binding energies for polymers containing hydroxyl, ether, ketone and ester groups”, *Surface and Interface Analysis*, **17** [5] pp. 267-272 (1991).
- [92] Y. Shi, S. Long, S. Yang, and F. Pan, “Deposition of nano-scaled CrTiAlN multilayer coatings with different negative bias voltage on Mg alloy by unbalanced magnetron sputtering”, *Vacuum*, **84** [7] pp. 962-968 (2010).
- [93] “ISO/CD 14577-1. Metallic materials — Instrumented indentation test for hardness and other materials parameters — Part 1: Test Method, ISO, 1999.”.
- [94] S. Shukla, S. Seal, Z. Rahaman, and K. Scammon, “Electroless copper coating of cenospheres using silver nitrate activator”, *Materials Letters*, **57** [1] pp. 151-156 (2002).
- [95] *XPS Handbook of the Elements and Native Oxides*, XPS International Inc., 1999
- [96] M. Detroye, F. Reniers, C. Buess-Herman, and J. Vereecken, “AES–XPS study of chromium carbides and chromium iron carbides”, *Applied Surface Science*, **144–145** [0] pp. 78-82 (1999).
- [97] B. Warcholinski, A. Gilewicz, Z. Kuklinski, and P. Myslinski, “Hard CrCN/CrN multilayer coatings for tribological applications”, *Surface and Coatings Technology*, **204** [14] pp. 2289-2293 (2010).

- [98] J. Almer, M. Odén, and G. Håkansson, "Microstructure, stress and mechanical properties of arc-evaporated Cr–C–N coatings", *Thin Solid Films*, **385** [1–2] pp. 190-197 (2001).
- [99] P. F. Hu, G. J. Yin, and S. K. Zhou, "Influence of Carbon Doping on Microstructure and Tribological Properties of CrN Coating", *Advanced Materials Research*, **325** pp. 263-268 (2012).
- [100] A. P. Ehasarian, W. D. Münz, L. Hultman, U. Helmersson, and I. Petrov, "High power pulsed magnetron sputtered CrN_x films", *Surface and Coatings Technology*, **163–164** [0] pp. 267-272 (2003).
- [101] G. S. Kim, S. Y. Lee, J. H. Hahn, and S. Y. Lee, "Synthesis of CrN/AlN superlattice coatings using closed-field unbalanced magnetron sputtering process", *Surface and Coatings Technology*, **171** [1–3] pp. 91-95 (2002).
- [102] e. T.Y. Tsui, "Nanoindentation and nanoscratching of hard carbon coatings for magnetic disks", *MRS Proceedings*, **383** (1995).
- [103] D. V. Shtanskii, S. A. Kulinich, E. A. Levashov, and J. J. Moore, "Structure and physical-mechanical properties of nanostructured thin films", *Physics of the Solid State*, **45** [6] pp. 1177-1184 (2003).
- [104] K. L. Johnson, *Contact Mechanics*, Cambridge University Press, London, UK,, 1985.
- [105] L. D. Wang, M. Li, and T. H. Zhang, "Hardness Measurement and Evaluation of Thin Film on Material Surface", *Chinese Journal of Aeronautics* **16** pp. 52-58 (2003).
- [106] P. H. Mayrhofer, G. Tischler, and C. Mitterer, "Microstructure and mechanical/thermal properties of Cr–N coatings deposited by reactive unbalanced magnetron sputtering", *Surface and Coatings Technology*, **142–144** [0] pp. 78-84 (2001).
- [107] J. Shirahata, T. Otori, H. Asami, T. Suzuki, T. Nakayama, H. Suematsu, Y. Nakajima, and K. Niihara, "Preparation of Cr(N,O) thin films by RF reactive unbalanced magnetron sputtering", *Thin Solid Films*, **519** [11] pp. 3497-3500 (2011).
- [108] A. Leyland, and A. Matthews, "On the significance of the H/E ratio in wear control: a nanocomposite coating approach to optimised tribological behaviour", *Wear*, **246** [1–2] pp. 1-11 (2000).
- [109] Z. B. Qi, P. Sun, F. P. Zhu, Z. C. Wang, D. L. Peng, and C. H. Wu, "The inverse Hall–Petch effect in nanocrystalline ZrN coatings", *Surface and Coatings Technology*, **205** [12] pp. 3692-3697 (2011).
- [110] D. Mercks, N. Bonasso, S. Naamane, J.-M. Bordes, and C. Coddet, "Mechanical and tribological properties of Cr–N and Cr–Si–N coatings reactively sputter deposited", *Surface and Coatings Technology*, **200** [1–4] pp. 403-407 (2005).
- [111] E. Martinez, R. Sanjinés, O. Banakh, and F. Lévy, "Electrical, optical and mechanical properties of sputtered CrNy and Cr1–xSixN1.02 thin films", *Thin Solid Films*, **447–448** [0] pp. 332-336 (2004).
- [112] I.-W. Park, D. S. Kang, J. J. Moore, S. C. Kwon, J. J. Rha, and K. H. Kim, "Microstructures, mechanical properties, and tribological behaviors of Cr–Al–N, Cr–Si–N, and Cr–Al–Si–N coatings by a hybrid coating system", *Surface and Coatings Technology*, **201** [9–11] pp. 5223-5227 (2007).
- [113] Z. L. Wu, J. Lin, J. J. Moore, and M. K. Lei, "Microstructure, mechanical and tribological properties of Cr–C–N coatings deposited by pulsed closed field unbalanced magnetron sputtering", *Surface and Coatings Technology*, **204** [6–7] pp. 931-935 (2009).
- [114] Bruno B. Lopes, Rita C. C. Rangel, Cesar A. Antonio, Steven F. Durrant, Nilson C. Cruz, and E. C. Rangel, "Mechanical and Tribological Properties of Plasma Deposited a-C:H:Si:O Films," *Nanoindentation in Materials Science* D. J. Nemecek, ed., 2012.
- [115] Y. M. Zhou, R. Asaki, K. Higashi, W. H. Soe, and R. Yamamoto, "Sliding wear behavior of polycrystalline TiN/CrN multilayers against an alumina ball", *Surface and Coatings Technology*, **130** [1] pp. 9-14 (2000).
- [116] T. Polcar, T. Kubart, R. Novák, L. Kopecký, and P. Šíroký, "Comparison of tribological

- behaviour of TiN, TiCN and CrN at elevated temperatures”, *Surface and Coatings Technology*, **193** [1–3] pp. 192-199 (2005).
- [117] J. Guo, H. Wang, F. Meng, X. Liu, and F. Huang, “Tuning the H/E* ratio and E* of AlN coatings by copper addition”, *Surface and Coatings Technology*, **228** [0] pp. 68-75 (2013).
- [118] P. C. Wo, P. R. Munroe, Z. F. Zhou, K. Y. Li, and Z. H. Xie, “Effects of TiN sublayers on the response of TiSiN nanocomposite coatings to nanoindentation and scratching contacts”, *Materials Science and Engineering: A*, **527** [16–17] pp. 4447-4457 (2010).
- [119] M. V. Swain, and J. Menčík, “Mechanical property characterization of thin films using spherical tipped indenters”, *Thin Solid Films*, **253** [1–2] pp. 204-211 (1994).
- [120] M. Vandamme, and F.-J. Ulm, “Viscoelastic solutions for conical indentation”, *International Journal of Solids and Structures*, **43** [10] pp. 3142-3165 (2006).
- [121] D. M. Ebenstein, and L. A. Pruitt, “Nanoindentation of biological materials”, *Nano Today*, **1** [3] pp. 26-33 (2006).
- [122] H. N. Shah, R. Jayaganthan, and A. C. Pandey, “Nanoindentation study of magnetron-sputtered CrN and CrSiN coatings”, *Materials & Design*, **32** [5] pp. 2628-2634 (2011).
- [123] Z. G. Zhang, O. Rapaud, N. Allain, D. Mercs, M. Baraket, C. Dong, and C. Coddet, “Microstructures and tribological properties of CrN/ZrN nanoscale multilayer coatings”, *Applied Surface Science*, **255** [7] pp. 4020-4026 (2009).
- [124] L. W. Ma, J. M. Cairney, M. Hoffman, and P. R. Munroe, “Deformation mechanisms operating during nanoindentation of TiN coatings on steel substrates”, *Surface and Coatings Technology*, **192** [1] pp. 11-18 (2005).
- [125] X. Wu, I. Baker, H. Wu, and P. R. Munroe, “Dry sliding wear of nanostructured Fe₃₀Ni₂₀Mn₂₀Al₃₀”, *Intermetallics*, **23** [0] pp. 116-127 (2012).
- [126] J. Lin, W. D. Sproul, J. J. Moore, S. Lee, and S. Myers, “High rate deposition of thick CrN and Cr₂N coatings using modulated pulse power (MPP) magnetron sputtering”, *Surface and Coatings Technology*, **205** [10] pp. 3226-3234 (2011).
- [127] L. Aihua, D. Jianxin, C. Haibing, C. Yangyang, and Z. Jun, “Friction and wear properties of TiN, TiAlN, AlTiN and CrAlN PVD nitride coatings”, *International Journal of Refractory Metals and Hard Materials*, **31** [0] pp. 82-88 (2012).
- [128] B. D. Beake, V. M. Vishnyakov, and J. S. Colligon, “Nano-impact testing of TiFeN and TiFeMoN films for dynamic toughness evaluation”, *J. Phys. D: Appl. Phys.*, **44** (2011).
- [129] Y. S. Yang, T. P. Cho, and Y. C. Lin, “Effect of coating architectures on the wear and hydrophobic properties of Al–N/Cr–N multilayer coatings”, *Surface and Coatings Technology*, [0].
- [130] M. Pettersson, S. Tkachenko, S. Schmidt, T. Berlind, S. Jacobson, L. Hultman, H. Engqvist, and C. Persson, “Mechanical and tribological behavior of silicon nitride and silicon carbon nitride coatings for total joint replacements”, *Journal of the Mechanical Behavior of Biomedical Materials*, **25** [0] pp. 41-47 (2013).
- [131] B. Warcholinski, and A. Gilewicz, “Effect of substrate bias voltage on the properties of CrCN and CrN coatings deposited by cathodic arc evaporation”, *Vacuum*, **90** [0] pp. 145-150 (2013).
- [132] F. Cai, Q. Yang, D. Nagy, and X. Huang, “Tribological Behaviors of Titanium Nitride- and Chromium-Nitride-Based Physical Vapor Deposition Coating Systems”, *Journal of Engineering for Gas Turbines and Power*, **134** [11] pp. 112504-112504 (2012).
- [133] R. J. Hill, and C. J. Howard, “Quantitative phase analysis from neutron powder diffraction data using the Rietveld method”, *Journal of Applied Crystallography*, **20** [6] pp. 467-474 (1987).
- [134] P. H. Mayrhofer, F. Rovere, M. Moser, C. Strondl, and R. Tietema, “Thermally induced transitions of CrN thin films”, *Scripta Materialia*, **57** [3] pp. 249-252 (2007).
- [135] Martí, amp, x, E. nez, J. Romero, A. Lousa, and J. Esteve, “Wear behavior of nanometric CrN/Cr multilayers”, *Surface and Coatings Technology*, **163–164** [0] pp. 571-577 (2003).

- [136] T. Polcar, N. M. G. Parreira, and R. Novák, "Friction and wear behaviour of CrN coating at temperatures up to 500 °C", *Surface and Coatings Technology*, **201** [9–11] pp. 5228-5235 (2007).
- [137] P. van Essen, R. Hoy, J. D. Kamminga, A. P. Ehasarian, and G. C. A. M. Janssen, "Scratch resistance and wear of CrNx coatings", *Surface and Coatings Technology*, **200** [11] pp. 3496-3502 (2006).
- [138] B. Warcholinski, and A. Gilewicz, "The Properties of Multilayer CrCN/CrN Coatings Dependent on Their Architecture", *Plasma Processes and Polymers*, **8** [4] pp. 333-339 (2011).
- [139] P. Hones, R. Consiglio, N. Randall, and F. Leacutevy, "Mechanical properties of hard chromium tungsten nitride coatings", *Surface and Coatings Technology*, **125** [1–3] pp. 179-184 (2000).
- [140] M. Uchida, N. Nihira, A. Mitsuo, K. Toyoda, K. Kubota, and T. Aizawa, "Friction and wear properties of CrAlN and CrVN films deposited by cathodic arc ion plating method", *Surface and Coatings Technology*, **177–178** [0] pp. 627-630 (2004).